**Title**
Scanning Tunneling Microscopy of Charge Density Wave Structure in 1T-TaS2



**Author**
Thomson, R.E.

**Publication Date**
1991-11-01

LBL-31673
UC-404

Lawrence Berkeley Laboratory
UNIVERSITY OF CALIFORNIA

Materials Sciences Division

# Scanning Tunneling Microscopy of Charge Density Wave Structure in 1T-$TaS_2$

R.E. Thomson
(Ph.D. Thesis)

November 1991



Prepared for the U.S. Department of Energy under Contract Number DE-AC03-76SF00098

## DISCLAIMER

LBL-31673

# Scanning Tunneling Microscopy of Charge Density Wave Structure in 1T-$TaS_2$

Ruth Ellen Thomson

Department of Physics,
University of California
Berkeley, CA 94720

and

Materials Sciences Division
Lawrence Berkeley Laboratory
University of California
Berkeley, CA 94720

November 1991

This work was supported by the Director, Office of Energy Research, Office of Basic Energy Sciences, Materials Sciences Division of the U.S. Department of Energy under contract number DE-AC03-76SF00098.

Scanning Tunneling Microscopy of Charge Density Wave Structure in 1T-$TaS_2$

by

Ruth Ellen Thomson

## Abstract

I have used a scanning tunneling microscope (STM) to image simultaneously the atomic lattice and the charge density wave (CDW) superstructure in tantalum disulfide (1T-$TaS_2$) over the temperature range of 370-77K. In the lowest temperature (commensurate) phase, present below 180K, the CDW is at an angle of 13.9° relative to the lattice and is uniformly commensurate. In the incommensurate phase, present above 353K, the CDW is aligned with the lattice.

1T-$TaS_2$ exhibits two other phases; the triclinic (**T**) phase which is present between 223K and 283K upon warming the sample, and the nearly-commensurate (**NC**) phase which is present between 353K and 180K upon cooling the sample and between 283K and 353K upon warming the sample. In both of these phases, discommensurate models where the CDW is arranged in small commensurate domains have been proposed. In the **NC** phase the CDW is rotated between 10° and 12.5° relative to the atomic lattice. Such a rotated CDW would create an interference pattern with the underlying atomic lattice regardless of the existence of a true domain superstructure. Previous work on 1T-$TaS_2$ has not adequately accounted for the possibility of this moiré pattern. However, around each fundamental CDW peak in the Fourier transform of the real space STM images,

several satellite spots are visible, which conclusively prove the existence of domains in the **NC** phase.

In the **T** phase, STM images clearly show discommensurations and domains of the CDW which are verified by the satellite spots in the Fourier transform. However, the shape and size of these domains do not agree with those of the stretched honeycomb model proposed by Nakanishi and Shiba, but do agree with the striped model developed by my co-worker B. Burk from his new x-ray diffraction results.

In addition, I report on our STM studies of two other CDW materials, blue bronze and o-$TaS_3$. With blue bronze we obtain STM images of the atomic structure but do not observe the CDW. With o-$TaS_3$ we observe 1-D CDW fluctuations above the critical temperature.

This thesis is dedicated to

F. Bear and M. Muscoon.

Thesis Outline

Acknowledgements

I have enjoyed my graduate school experience very much and this is largely due to the wonderful group of people I have worked with. First of all I would like to thank my advisor, John Clarke, for paying me all these years, as well as for his enthusiasm, guidance, patient editing, and many ideas for the project. David Abraham, Eric Ganz and especially John Mamin, the original members of the STM lab, invested a lot of their time and energy in my training the first several years I worked on this project, and I would like to gratefully thank them for their patience and good humor. I would like to thank the post-docs who worked with me, Ulrich Walter and Philippe Renauld, for all their help and advice, hard work and friendliness. I would also like to thank Prof. Knute Fisher and Prof. Alex Zettl and his students for their long and very fruitful collaborations with the STM lab. In particular, Brian Burk made very large contributions to the work on 1T-$TaS_2$, Ulrich Walter collaborated on the work on blue bronze described in chapter 8, and Jing-bao Liu did much of the work on o-$TaS_3$ described in chapter 9. Al Daft, the supervisor of the student shop for many years, deserves a special thank you for his great patience and many good ideas on how to machine tricky parts. The other members of the Clarke group, especially Mark Shattuck, Nancy Missert, Mats Gustafsson and Sue Whitfield have always been willing to discuss the experiment (or anything else) and offer helpful advice. Also, I would like to thank Prof. Owen Chamberlain for tutoring me to help me prepare for my prelim exams. My housemates over the years, Bob Phelps, Margo Damasser, Carl Mears, Mats Gustafsson, Andre Clapp and Mari Strain have always provided a

supportive and congenial home environment. I would like to offer a special thank you to my good friend Roger Carr for years of support, optimism, encouragement, and very good advice. And lastly, I would like to thank my parents and brothers for helping to make me who I am, which is what ultimately got me through graduate school.

This work was supported by the Director, Office of Energy Research, Office of Basic Energy Science, Materials Science Division of the U.S. Department of Energy, under contract number DE-AC03-76SF00098.

# Chapter I

## Introduction

Since it was first described in detail in 1974,[1] 1T-$TaS_2$ has been a popular material for study with a wide variety of techniques. This is because it was discovered that the material not only supported a charge density wave (CDW), but that it underwent a complicated series of phase transitions as a function of temperature. A great deal of work was done to assess the nature of the transitions and the CDW in each phase using such techniques as x-ray and electron diffraction,[2] Rutherford backscattering,[3] differential scattering calorimetry,[4] x-ray photoemission,[5] and high resolution electron microscopy,[6] to name only a few. Because of the subtlety of the nature of the the CDW in several phases, until the advent of the scanning tunneling microscope (STM), there was not a general agreement on the details of the CDW in these phases.

The STM was invented in 1981 by Binnig, Rohrer and Gerber[7] and has enjoyed more than a decade of exploding popularity. The technique is really quite simple, being based on measuring the tunneling current between a sharp metal tip and a conducting sample. A small bias voltage is applied between the tip and the sample, and this voltage is held constant. If the tip is within a few Angstroms of the sample, the tunneling current which is induced by this voltage is measured by a pre-amplifier and then fed to a feedback circuit which uses this signal to maintain the tip at the correct height above the surface. The tip is then scanned across the sample in a raster pattern using a piezoelectric scanner and either

the tunneling current or the height of the tip above the surface is recorded to produce an image of the surface.

Since the induced tunneling current is exponentially dependent on the distance between the tip and the sample, the STM can have a very high resolution, especially in the vertical dimension. This is important in the present study because it allows us to obtain, routinely, images with atomic resolution on 1T-$TaS_2$. The tunneling current is also proportional to the electronic density of states near the Fermi level, making the STM capable of imaging a charge density wave, which is essentially a spatial rearrangement of the electrons near the Fermi level. Therefore, the STM is an ideal instrument to use to resolve the remaining questions about the nature of the various CDW phases in 1T-$TaS_2$.

---

[1]J.A.Wilson, F.J.DiSalvo and S.Mahajan, Phys. Rev. Lett. **32**, 882 (1974); and J.A.Wilson, F.J.DiSalvo and S.Mahajan, Adv. Phys. **24**, 117 (1975).

[2]S.Tanda, T.Sambongi, T.Tani and S.Tanaka, J. Phys. Soc. Jpn. **53**, 476 (1984); C.P.Scruby, P.M.Williams and G.S.Parry, Phil. Mag. **31**, 255 (1975); L.D.Chapman and R.Colella, Phys. Rev. B **32**, 2233 (1985); R.L.Withers and J.W.Steeds, J. Phys. C **20**, 4019 (1987); J.A.Wilson, F.J.DiSalvo and S.Mahajan, Adv. Phys. **24**, 117 (1975).

[3]T.Haga and Y.Abe, Phys. Rev. Lett. **51**, 678 (1983).

[4]S.C.Bayliss, A.M.Ghorayeb and D.R.P.Guy, J.Phys. C **17**, L533 (1984).

[5]H.P.Hughes and R.A.Pollak, Comm. Phys. **1**, 61 (1976).

[6]M.Kuwabara, M.Tomito, H.Hashimoto and H.Endoh phys. stat. sol. (a) **96**, 39 (1986).

[7]G.Binnig, H.Rohrer, Ch.Gerber and E.Weibel, Phys. Rev. Lett. **49**, 57 (1982).

# Chapter II
# EQUIPMENT

In this chapter I describe the STM equipment used in the experiments discussed in the later chapters of this thesis, including the microscope itself, the electronics which controlled it and the computer hardware and software which performed the data acquisition and analysis.

## (a) The Microscope

The tunneling microscope I used for my thesis experiments was a modification of designs by Kaiser and Jacklevic,[1] and by Drake *et al.* [2] It consists of a metal base plate, supported by three height adjustment screws, clamped onto the main microscope body by two springs (Fig. 2-1). In order to minimize thermal drift, in the latest versions of the microscope we have machined the microscope body and base plate out of invar. The three height adjustment screws together form a kinematic mount. All three screws terminate in 4.76 mm stainless steel ball bearings. One screw is positioned above three more ball bearings glued to the base plate so that the screw and microscope body are constrained to rotate about this pivot point. The second screw is positioned above a narrow groove machined into the base plate so that it can move along one dimension relative to the first screw. The final screw is free to move in two dimensions as its ball bearing rests on the flat surface of the base plate. This arrangement results in stable microscope operation even when the microscope is subjected to temperature changes.

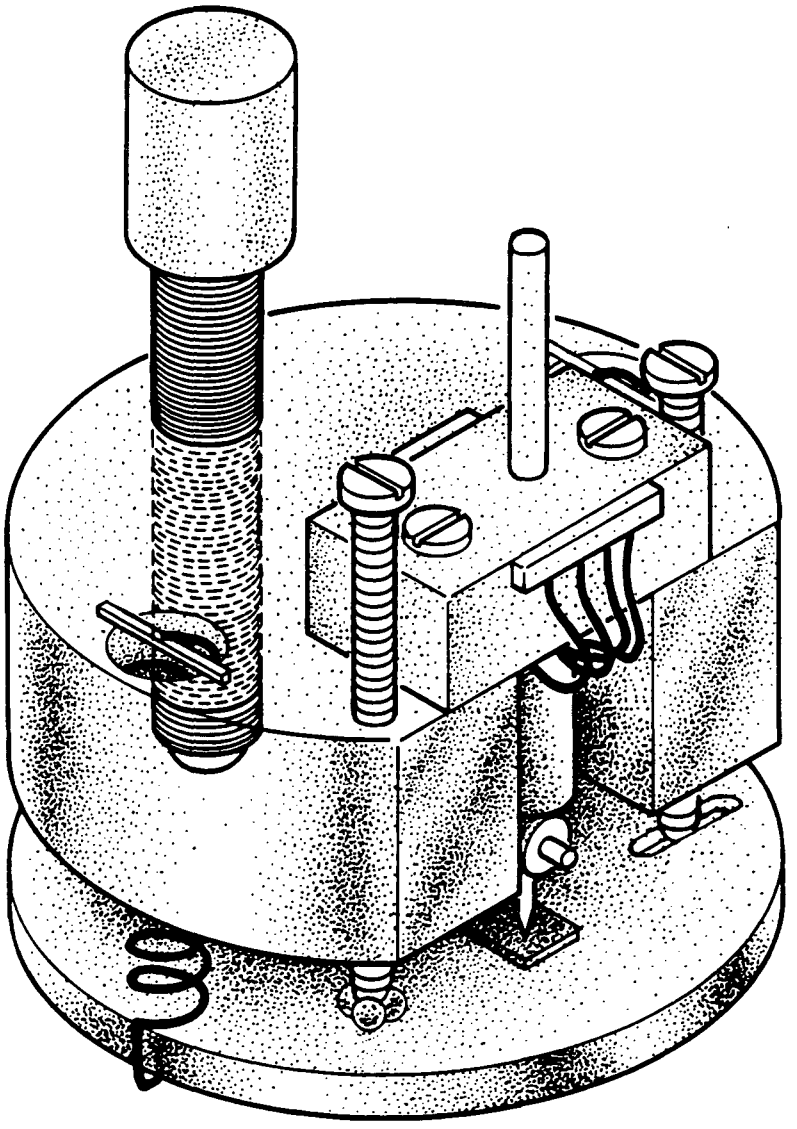

XBL-884 7338

Figure 2-1. Schematic drawing of the STM. The thin plate acts as a lever arm to facilitate adjustment of the sample to within tunneling range. The fine-adjust screw is controlled by a motor and the entire microscope can be immersed in a cryogenic liquid.

The tunneling tip is moved across the sample surface with a piezoelectric tube scanner based on the design by Binnig and Smith.[3] We use piezoelectric tubes 12.7 mm long and 6.35 mm in diameter with a 0.75 mm wall thickness. The piezoelectric tube is coated with nickel and is "poled" radially so that an electric potential applied between the electrodes on the inside and the outside of the tube cause it to change its length. The outer electrode is scored vertically into four electrically isolated longitudinal quadrants. The x and y motion is caused by applying voltages of the same size but opposite polarity to opposing quadrants of the tube (Fig. 2-2), while z motion is controlled by the voltage applied to the inner electrode. Using graphite as a calibration sample, we find that the piezoelectric tube has a response of about 120 Å/V in x and y. The calibration in z was determined to be about 30 Å/V using a KAMAN magnetic measuring system. The piezoelectric tube is fairly stiff and with the tip holder glued to one end it exhibits a fundamental mechanical resonance around 8 kHz.

The tip holder consists of a small collar of macor (a machinable ceramic), to insulate it from the electrodes on the scanner, and a tiny stainless steel socket with two set screws to secure it to the tip. The tip holder holds the tip along the central axis of the scanner tube. We have tried to make the tip holder as small as possible in order to keep the mechanical resonance frequency of the scanner tube as high as possible.

The tip itself is made of 1 mm diameter Pt-20%Rh wire. We fashion the tip by simply cutting the wire with blunt wire cutters.

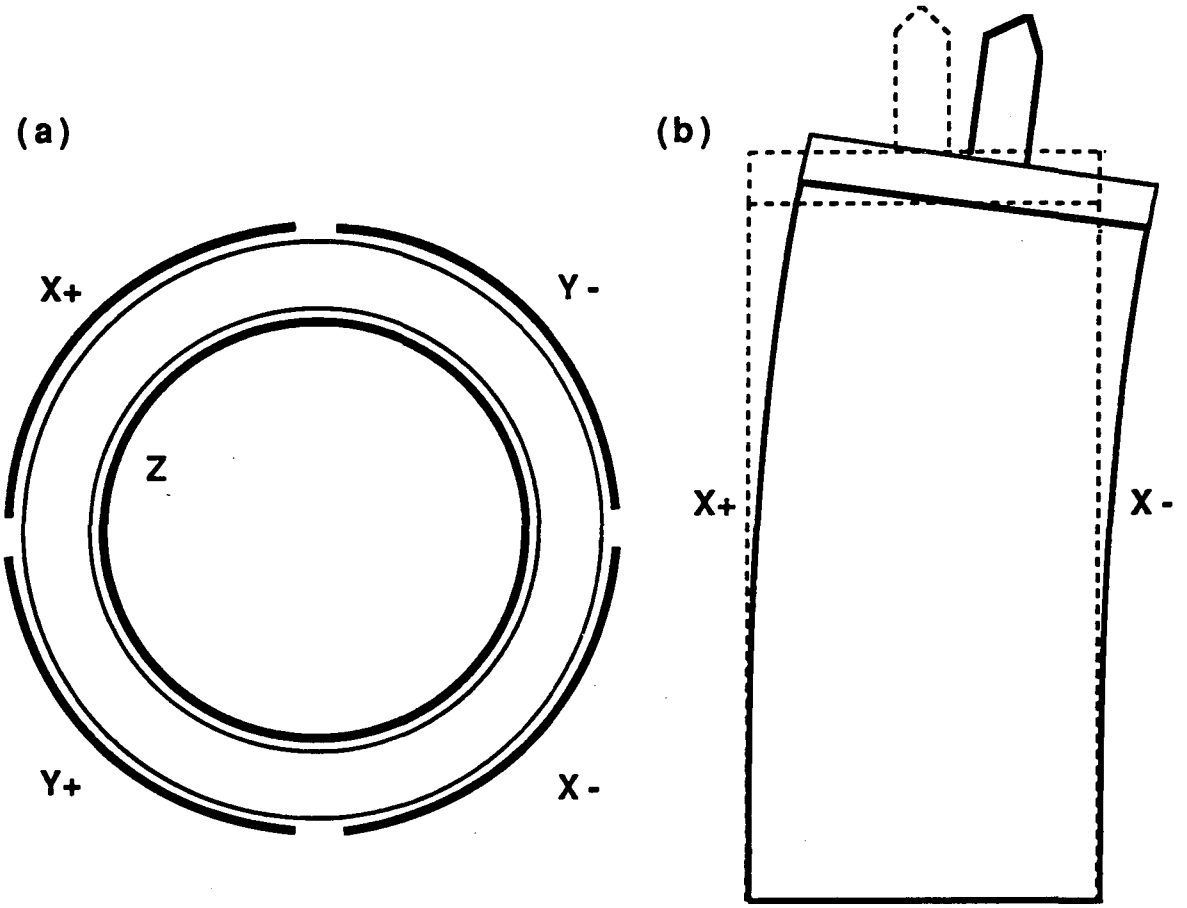


Figure 2-2. Schematic of the piezoelectric tube which controls the x, y, and z motion of the tunneling tip. (a) top view showing the scoring of the electrodes to create four equivalent quadrants. (b) side view illustrating lateral motion of the tip.

The platinum wire is so soft and the wire cutters are dull enough that the wire is squashed more than cut and the wire has to be pulled away from the wire cutters in order to cause the two pieces to part completely. This causes the formation of an axe-head shaped termination of the wire, the very end of which is work-hardened. We hold the wire cutters at a slight angle to the tip so that the end of the central ridge across the wire that forms the tip is at one edge of the wire. This makes the process of doing the coarse approach of the tip to the sample easier because the part of the wire that is going to form the actual tunneling tip is easy to distinguish. About 75% of the tips we form in this way achieve atomic resolution on graphite in air and continue to do so until an accident, such as crashing the tip into the sample, occurs.

The piezoelectric scanning tube is held in a macor mount on one edge of the microscope body. Directly beneath the scanning tube the sample is clamped to the base plate by two nylon screws. The two large height adjustment screws at this end of the microscope control the coarse adjustment of the tip-sample distance. Because the line joining the pivot positions of these screws is offset from the position of the tip by 1.5 mm, adjustment of the third screw, 30 mm from the tip, causes a motion of the sample relative to the tip of only 20 μm per turn. (The height adjustment screws all have 3.15 threads per mm.) We adjust the coarse position of the sample under a low-magnification optical microscope, moving the tip to within about 50μm of the surface. We use a geared-down DC motor to turn the fine-adjust screw at a rate of about 0.3 rotations per minute, bringing the tip towards the

sample surface with the z-drive feedback circuit in operation. As soon as a tunneling current is detected, the z drive retracts and the motor is switched off automatically. In this way, we can bring the tip within working range of the sample without touching the two together.

In order to achieve high resolution with an STM it is essential to minimize vibrations. The fact that our microscope is fairly small and rigid makes it much less sensitive to low frequency vibrations, but higher frequency vibrations can still excite resonances of the STM which cause the tip to move relative to the sample. This shows up as noise on the tunneling current and therefore degrades the resolution of the microscope. A very important factor in the minimization of the vibrational noise on the STM is the fact that our laboratory is in the second basement, which is the lowest floor of our building. In addition, the experiment is run on a miniature vibration isolation table of the sort used for optics experiments. Since acoustic noise present in the laboratory can excite vibrations in the STM, we protect the microscope from acoustic noise by operating it inside a glass bell-jar. With these precautions we are able routinely to resolve atomic features on such samples as graphite and 1T-$TaS_2$.

Another important factor in achieving high resolution is having a clean sample surface. Since our microscope operates at ambient pressure, there exist only a few materials which are sufficiently non-reactive that they stay clean enough in air that we can still achieve atomic resolution. We have improved the quality of the sample surface somewhat by extending the technique of Drake *et al.*[4]

who imaged samples immersed in mineral oil. All of the samples we used are layered materials and are cleavable using household transparent tape. We apply the tape to the sample and then immerse the sample in hexadecane before removing the tape. The tape peels off a thin layer of the material exposing a fresh surface. This surface is immediately coated with the hexadecane and so is never exposed to air during the cleaving process. Hexadecane is a light hydrocarbon with an extremely low vapor pressure, so the sample surface is protected by the hexadecane for many days. The hexadecane does not seem to interfere with the tunneling current in any way.

In order to study the temperature dependent properties of 1T-$TaS_2$ we required a temperature variable STM. The first phase transition of this material occurs at 360K and the last at 180K, so this was the temperature range in which we were interested. The temperature range above room temperature was achieved by heating mechanical pump oil as a thermal bath. The STM is mounted inside a copper can that hangs inside a glass dewar full of pump oil. The temperature of the oil is controlled using a heating tape immersed in the oil.

For temperatures below room temperature the bath of pump oil is replaced with a bath of *n*-pentane. In this case the copper can containing the microscope is also filled with pentane in order to dissolve the hexadecane off the sample surface. (The freezing point of hexadecane is only 291K, while that of *n*-pentane is 143K.) During the experiment, the temperature of the the pentane bath is lowered below the desired temperature by passing liquid nitrogen

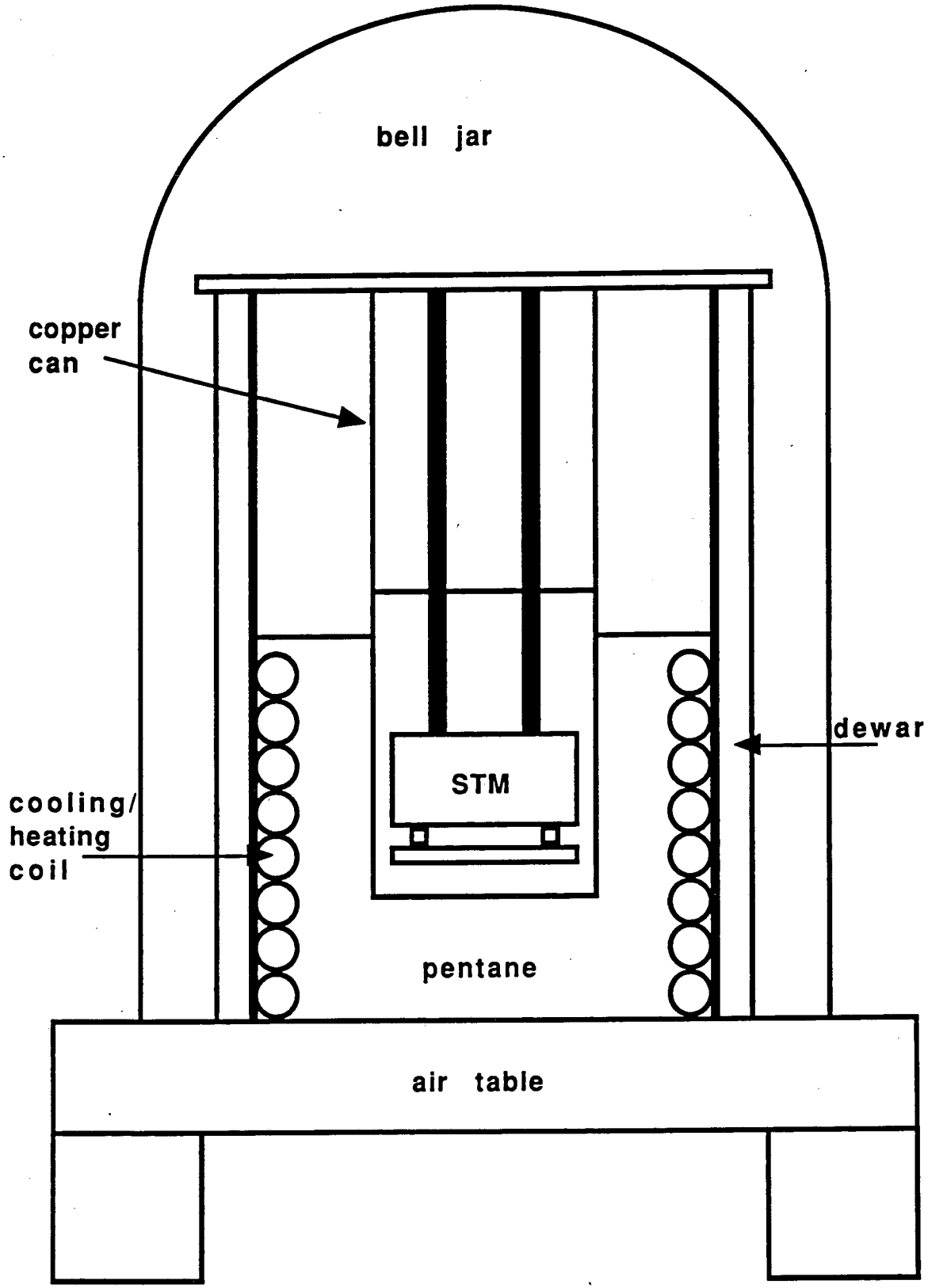


Figure 2-3 Overview of the experimental set-up.

through a copper coil immersed in the pentane bath. The bath temperature is then allowed to warm slowly back to room temperature. This technique allows the temperature of the experiment to warm slowly (≈3°C/h) while the data are taken, since in most cases this does not significantly degrade the images. Some of the later images were acquired using a slush bath of n-octane (215K) or of water (273K) which provided more thermally stable STM operation. For experiments both above and below room temperature, the temperature of the sample is determined with a silicon switching diode (1N-4448) mounted on the STM body and monitored with a handheld battery powered 3-1/2 digit voltmeter. The schematic diagram of the experimental set-up is shown in Fig. 2-3.

(b) Electronics

An overview of the electronics that control the STM is shown in Fig.2-4. This system consists of seven separate parts. The voltage bias box applies a DC bias voltage between the tip and the sample to induce the tunneling current. This current is sensed by the pre-amplifier whose output is fed into the feedback loop and then amplified by the high-voltage amplifier. The voltages used to scan the tip across the sample are produced in the x-y ramp generator. Finally, the signal amplifier is used to prepare the signal for the computer's A to D converter. The motor controller performs automatic coarse approach of the tip to the sample. Each of these items will be discussed separately.

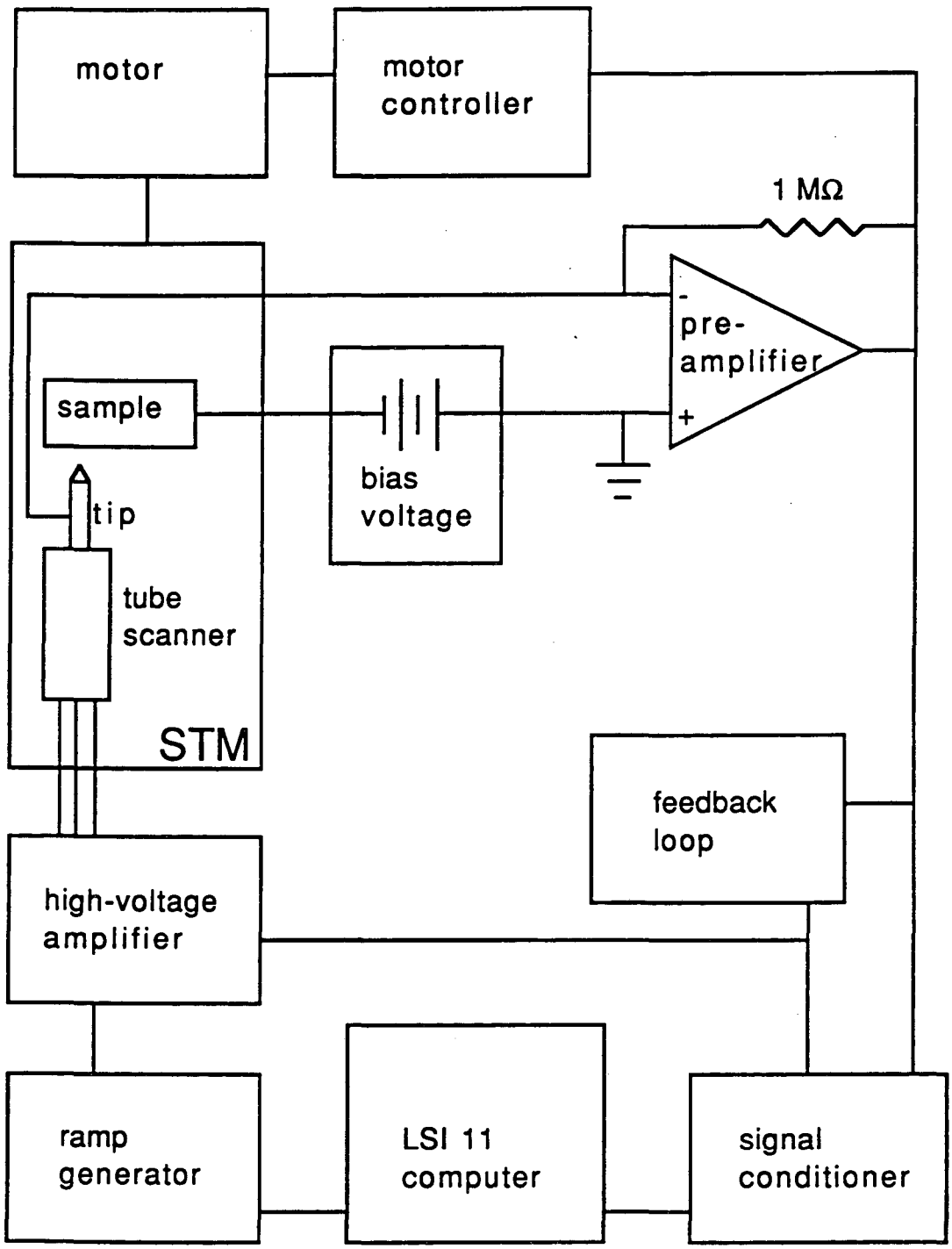


Figure 2-4 Schematic overview of the STM electronics.

The DC bias across the tunneling gap is generated by a long-life mercury 9-volt battery because it produces no 60 Hz noise. We use a simple resistive divider to provide bias voltages from 1 mV to 1 V. It is quite important to keep the lead from the battery to the sample well shielded to minimize the noise on the bias voltage. We use the pre-amp grounding plane as our grounding point for the STM electronics, so the bias battery is connected between this ground point and the sample. We find this leads to a lower noise level on the pre-amp signal than if the bias is applied to the tip.

The tunneling current which is induced by the bias voltage when the tip and the sample are very close (< 10 Å) is sensed by the pre-amplifier. The pre-amplifier consists of a current to voltage converter followed by an instrumentation op-amp with a gain of 20. Because it became desirable to acquire STM data at lower values of the tunneling current, we replaced the first pre-amplifier [shown in Fig. 2-5(a)] with one which had a larger gain [shown in Fig. 2-5(b)]. Because of capacitive pick-up on the lead between the tip and the pre-amplifier, it is important to keep this lead as short as possible. However, the geometry of our STM requires that this lead be about 30 cm long. This creates a noise level on the pre-amplifier output when there is no tunneling current of about 10 mV which is equivalent to 0.1 nA of tunneling current. The circuit diagrams for the pre-amplifiers used in the experiments in this thesis are shown in Fig. 2-5.

The output of the pre-amplifier is rectified and then fed into the feedback loop. The feedback circuit amplifies the signal,

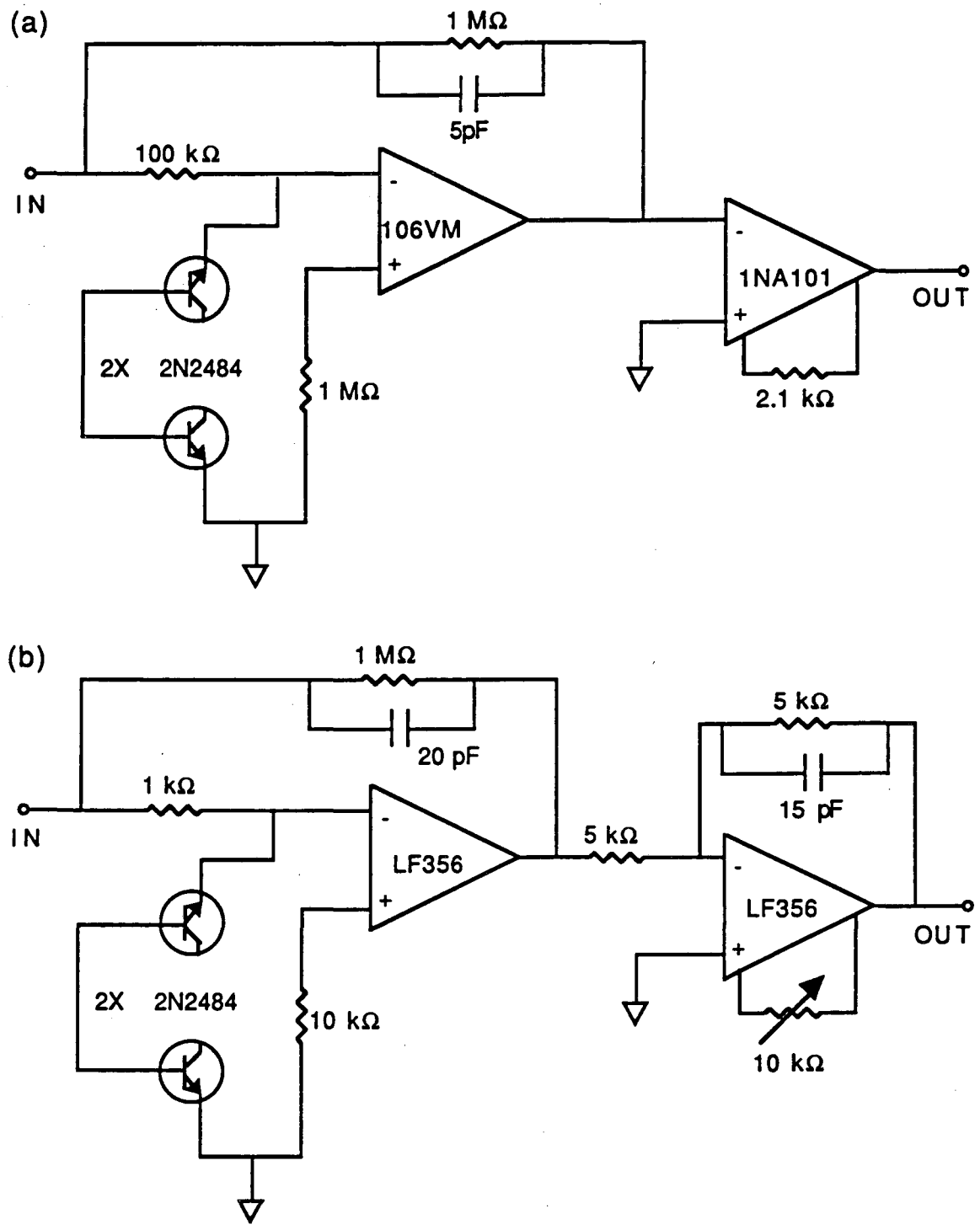


Figure 2-5 Schematics of the two pre-amplifiers used for this work. (a) Original pre-amplifier. (b) Improved pre-amplifier with higher gain.

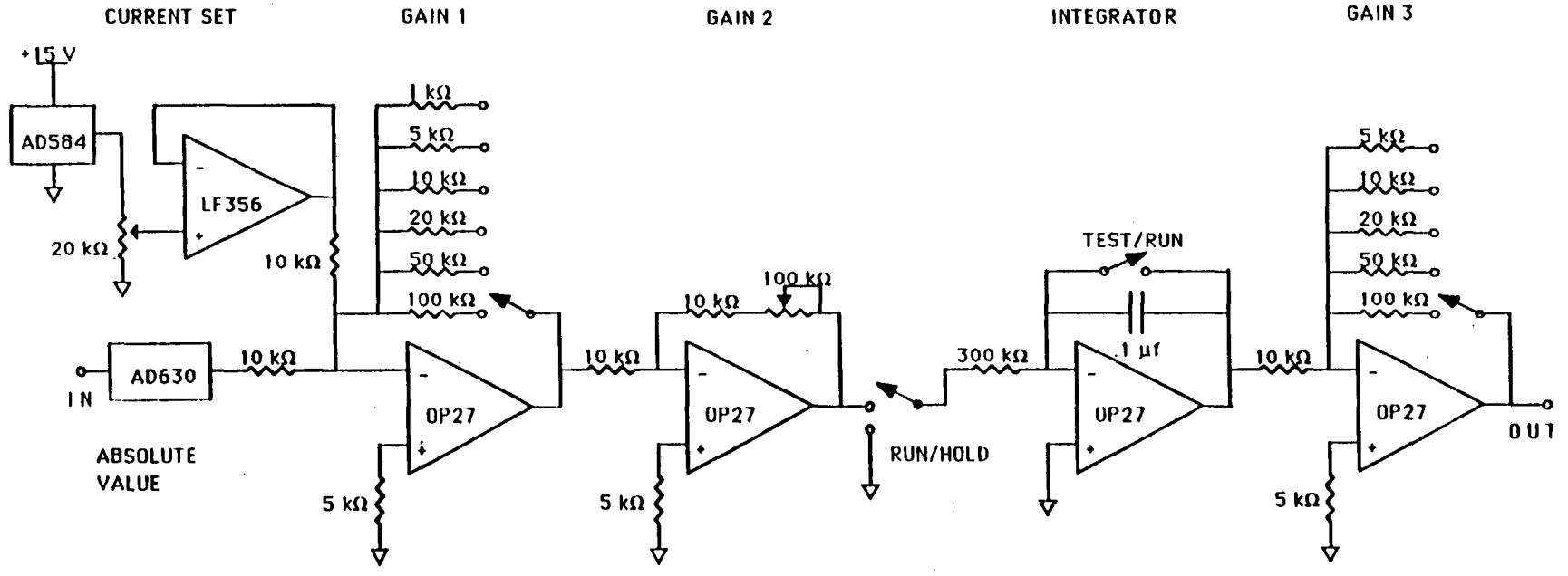


Figure 2-6 Schematic of the feedback circuit.

compares it to an adjustable current set and amplifies and filters the difference. The feedback circuit used during the experiments described in this thesis is identical to the one described in E.D.Ganz's Ph.D. thesis.[5] A schematic of this feedback circuit is shown in Fig. 2-6.

The output of the feedback circuit is amplified by a high-voltage amplifier. We use a Burr Brown 3582 300 V operational amplifier in a configuration shown in Fig. 2-7. For the feedback loop we use an amplifier gain of 24 and a 3 db rolloff at 60 Hz, with 1-2 mV of noise rms at the output. The output of the high-voltage amplifier is then applied to the z drive of the piezoelectric, thus completing the feedback loop.

To scan the x and y drives, we use analog ramps. The logic circuit used to control the ramps and interface them with the computer is shown in Fig. 2-8. The electronics that generate the variable amplitude, variable frequency ramps are shown in Fig. 2-9.

These ramps are then fed into high-voltage amplifiers identical to the one used for the z-drive and shown in Fig. 2-7. In this case we use two variable voltage dividers to generate DC signals that add offsets to the ramps. One voltage divider output is amplified by a factor of 25 by the high-voltage amplifier/adder to create a coarse offset and the other is used with no amplification to create a fine offset. The analog ramp can be fed in with either a gain of 1 or 25 depending on the size of the ramp desired. Two of the high-voltage amplifiers are operated between -15 V and + 250 V

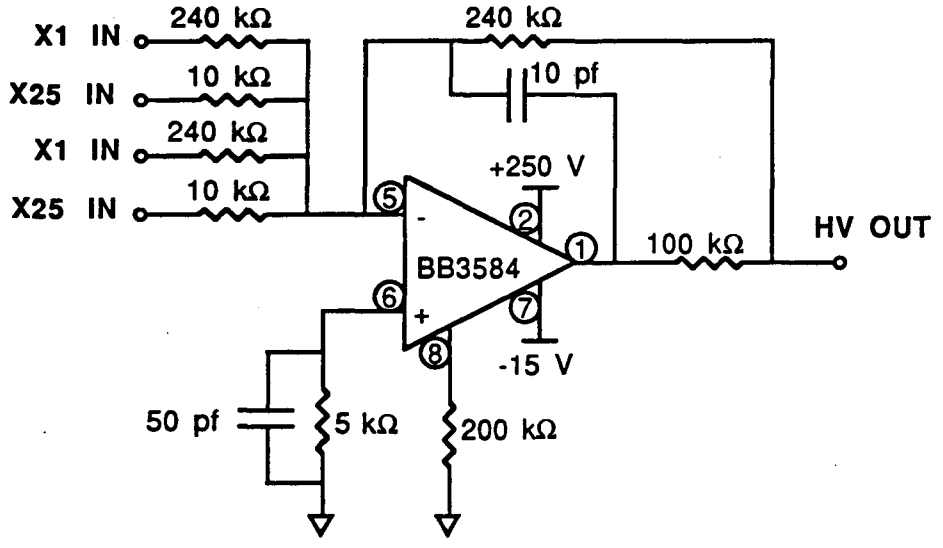


Figure 2-7 Schematic of the high voltage amplifier.

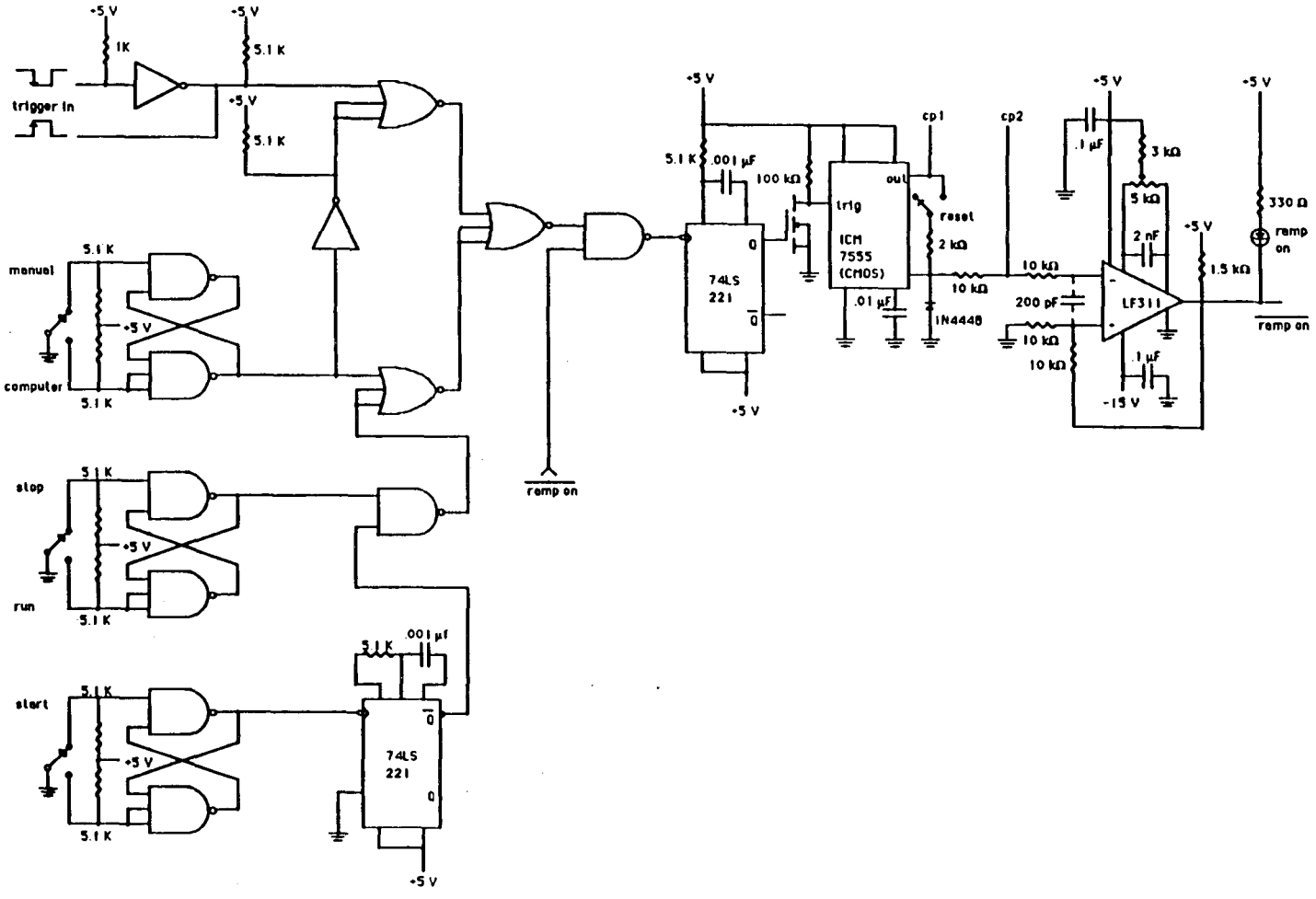


Figure 2-8 Schematic of the logic circuit used to control the analog ramps.

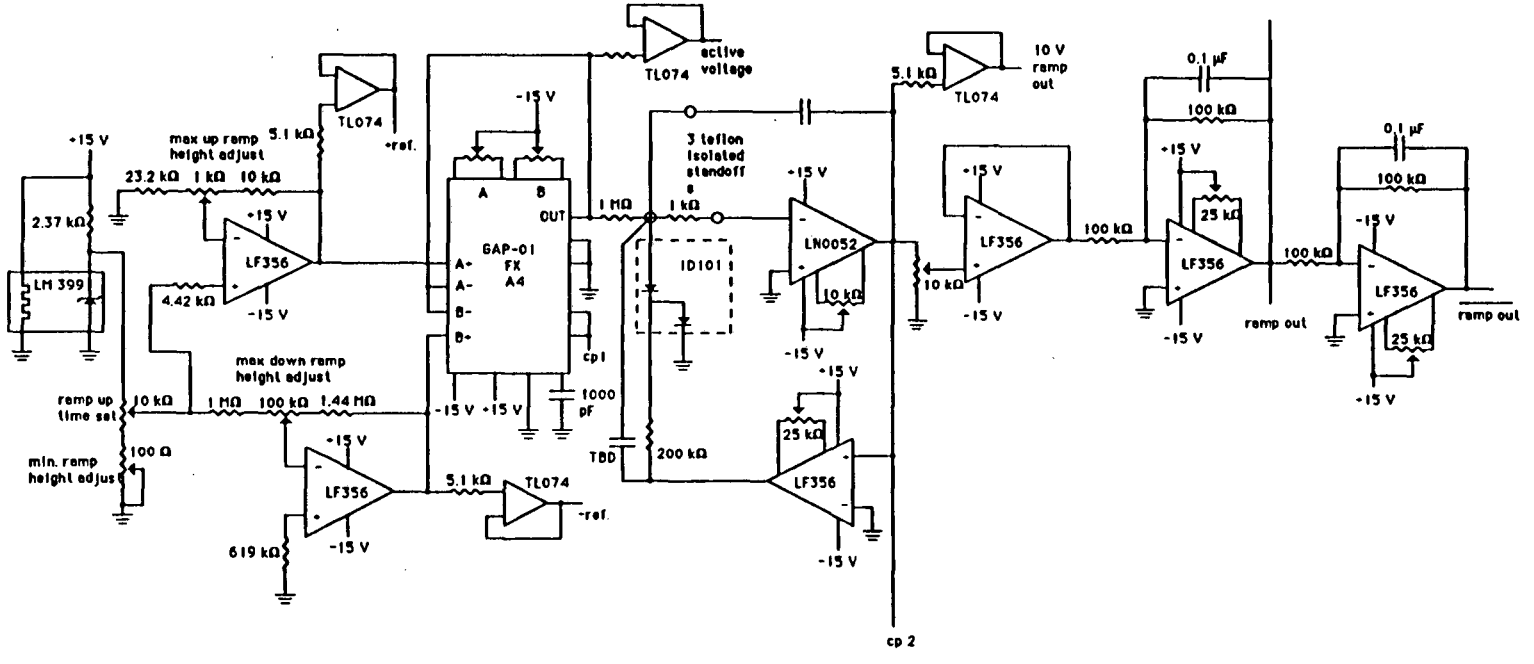


Figure 2-9 Schematic of the circuit generating the analog ramps used to scan the x and y drives.

and two between +15 V and -250 V in order to generate both the plus and minus x and y signals.

We employ a simple amplifier to do very limited signal processing before sending the signal to the computer. This amplifier may be operated in an inverting or a noninverting mode with a gain of 1 to 1000. Also, an offset is applied to the signal so that it is within the range accessible by the A to D converter in the computer.

The last piece of electronics necessary to run the STM is the motor controller circuit. This circuit controls the speed of the motor and causes it to shut off very quickly as soon as tunneling current is sensed. The schematic for this circuit is shown in Fig. 2-10.

(c) Computer control of the experiment and data analysis

The STM electronics, as well as the STM itself, are controlled by a DEC LSI 11/73 computer. This is an old machine which we still use because it is completely programmed and works well, although there are newer computers on the market today that could do the same things more quickly. A complete description of the hardware comprising this computer can be found in Eric Ganz's Ph.D. thesis.[5]

We employ two different programs (written in FORTRAN) to run the STM experiment. This is because we have two separate data taking modes. For larger images (images that cover a greater area of the surface) or for images of rough sample surfaces we have to use the slow scan mode. This method is sometimes referred to as the topographic or constant height mode. In this mode the tip is scanned across the surface at a rate which is slow enough that the

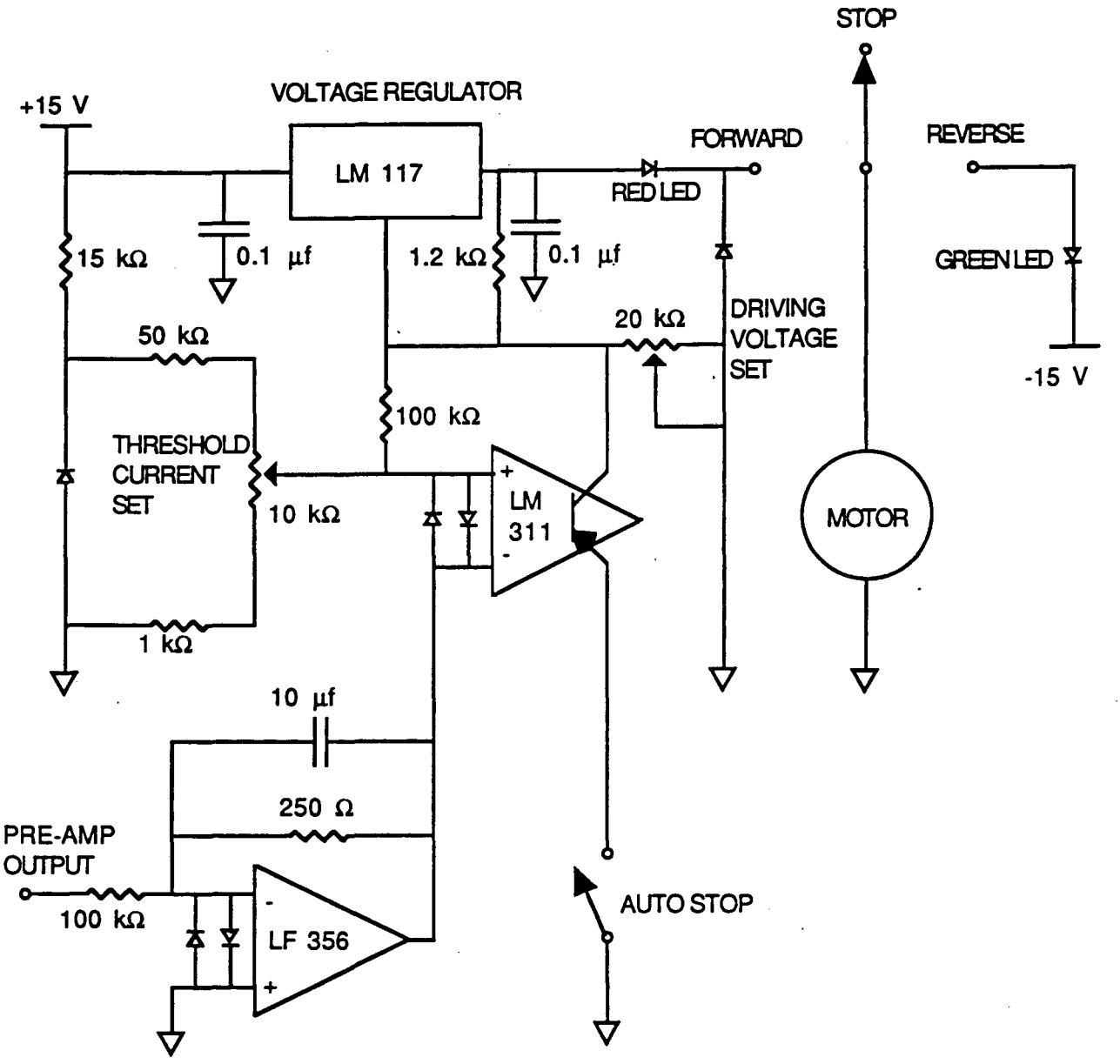


Figure 2-10 Schematic of the circuit controlling the motor used to turn the fine-adjust screw.

feedback loop can keep up with the changes in the topography of the surface and can always keep the tunneling current constant. In this method, the original method in which STM was done[3], the signal used to produce the height coordinate in the STM data is the high voltage signal which is being fed to the z drive of the piezoelectric scanner. Therefore, in this mode, the apparent height of the STM image is the actual height of the tip at each pixel location.

For the slow mode we use a data acquisition program called ACQUIR. This program will take up to 120 lines of data with 256 points along each scan line. The program stores the X, Y and Z coordinates at each point as well as an additional auxiliary data coordinate which can be the local work function or dI/dV. The menu tree for this program showing all the data acquisition and manipulation options is given in Appendix A.

The second method for acquiring STM images is the fast, or constant height, mode. In this mode the response time of the feedback circuit is adjusted to be fairly slow and the x and y scanning speeds are increased. We use an x scan speed of about 180 Hz and adjust the response time of the feedback circuit to approximately twice this value. This means that the tip is not able to track the individual features of the sample surface, but skims across the top of the sample with the feedback loop keeping the average height of the tip above the surface constant. In this mode, we use the output of the pre-amp, that is, the instantaneous current, as the intensity in the STM images. The feedback loop is still able to compensate for slow thermal drift and slight tilts of the sample surface, but this imaging mode is only suitable for use with very

flat samples as large topographic features such as steps will cause the tip to crash. However, for very flat samples such as those examined in this thesis, the fast data taking mode is usually superior. With its increased data acquisition speed some problems associated with thermal drift are minimized and it often produces higher resolution images than the slower topographical mode. Also, as will be explained in Chapter 4, it has a fundamental physical difference from the slow mode which can, in some special cases, cause the data taken in the two different modes to emphasize different features.

For use in the fast, constant height, mode, we use a data acquisition program called FASTD. The FASTD program can acquire images of 128 x 128 pixels at a rate of about 1 Hz per image, and more dense images of 256 x 256 pixels at a rate of about 0.33 Hz. The menu tree for the FASTD program showing all the data acquisition and manipulation options is given in Appendix A.

The bulk of the data manipulation and analysis is performed on the Tektronix 6130 computer. The STM images are translated into ascii files previous to transfer to the Tektronix and then KERMIT is used to accomplish the actual transfer. The Tektronix uses three programs for STM data. The first, CONVERT, simply converts the ascii file to a more compact file which is in the format used by the other two Tektronix programs. The second program CALIB, is used primarily to correct the STM images for distortions due to thermal drift or non-orthogonality of the x and y drives. (For a detailed description of this process see E. Ganz's thesis[5]). This program is

also capable of producing a model of the data for use in determining the relative orientation and spacing of various features in the image.

The third Tektronix program is by far the largest. This program is called FFT because one of its main functions is to calculate a fast Fourier transform (FT) of the image. Using the FT it is possible to low-pass filter the image or perform a lattice average in order to improve the appearance of the data and to elucidate important aspects of the image.

One type of filtering I have employed for many of the images shown in this thesis is illustrated in Fig. 2-11. This figure describes the filtering of an STM image of 1T-$TaS_2$ taken in the C phase, which will be fully discussed in Chapter 4. Figure 2-11(a) is the FT of the raw STM data which is shown in Fig. 2-11(b) (this image has been apodized, see the discussion of apodization in Chapter 6). Figure 2-11(c) is the FT after filtering. In this filtering method, only the peaks in the FT are saved, the rest of the transform is replaced with zeroes. The final image generated from the filtered transform is shown in Fig. 2-11(d). Although this is a very severe form of filtering, if done carefully it can greatly clarify the STM images. All of the images shown in this thesis which are described as "filtered" have been filtered in this way.

In a related procedure, the FT can be used to selectively keep one aspect of the image while discarding all other information. The usefulness of this procedure is illustrated in Fig. 2-12 (this data, 1T-$TaS_2$ in the I phase, is discussed in Chapter 5). Here just the lattice spots in the FT are saved and the resulting, modified, transform is used to produce an image showing just the atomic

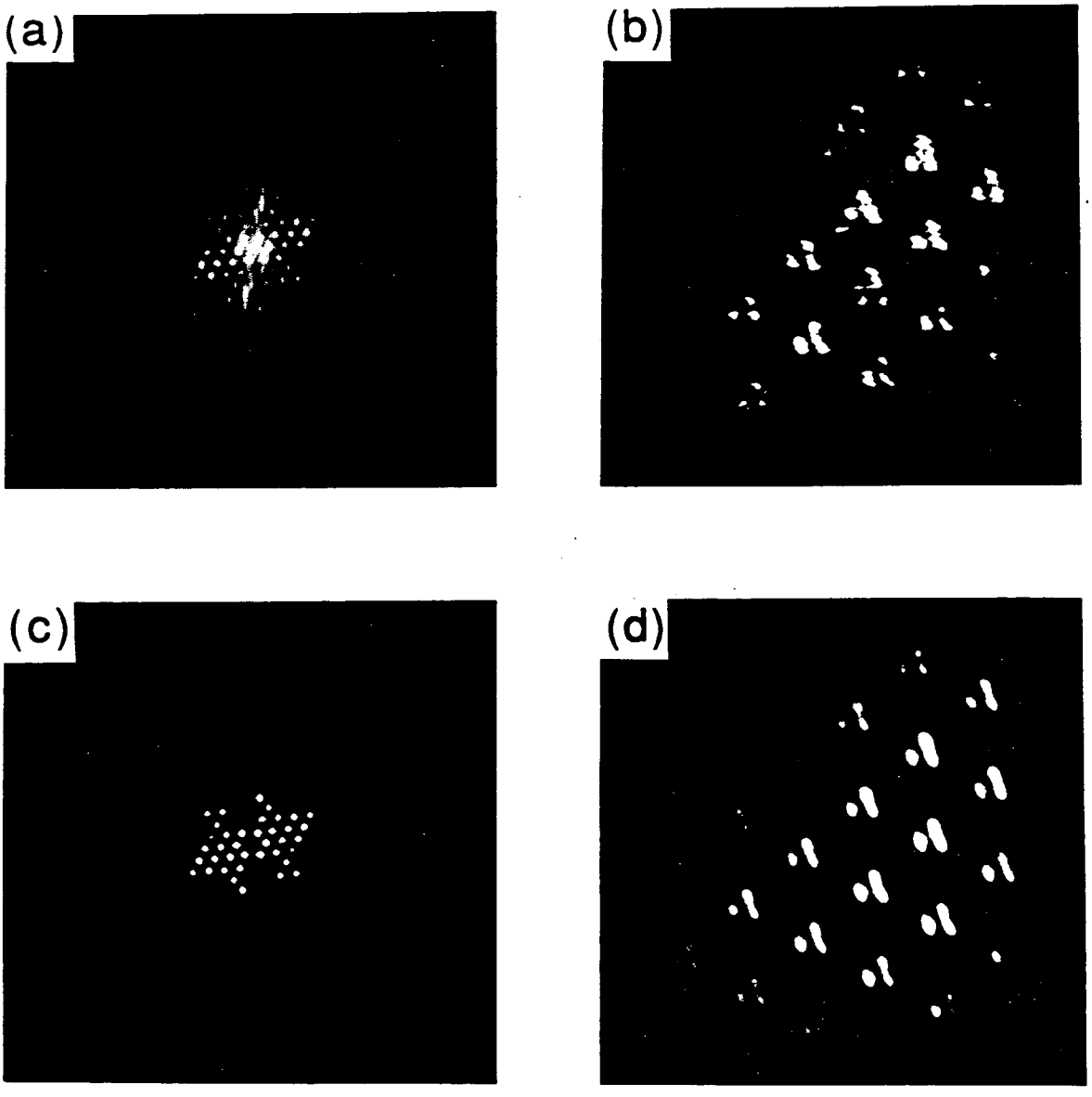


Figure 2-11 (a) The Fourier transform of the raw STM data. (b) The raw STM data. (c) The filtered Fourier transform generated by saving only the peaks in (a) and replacing the rest of the transform with zeroes. (d) The real space data generated by back-transforming (c).

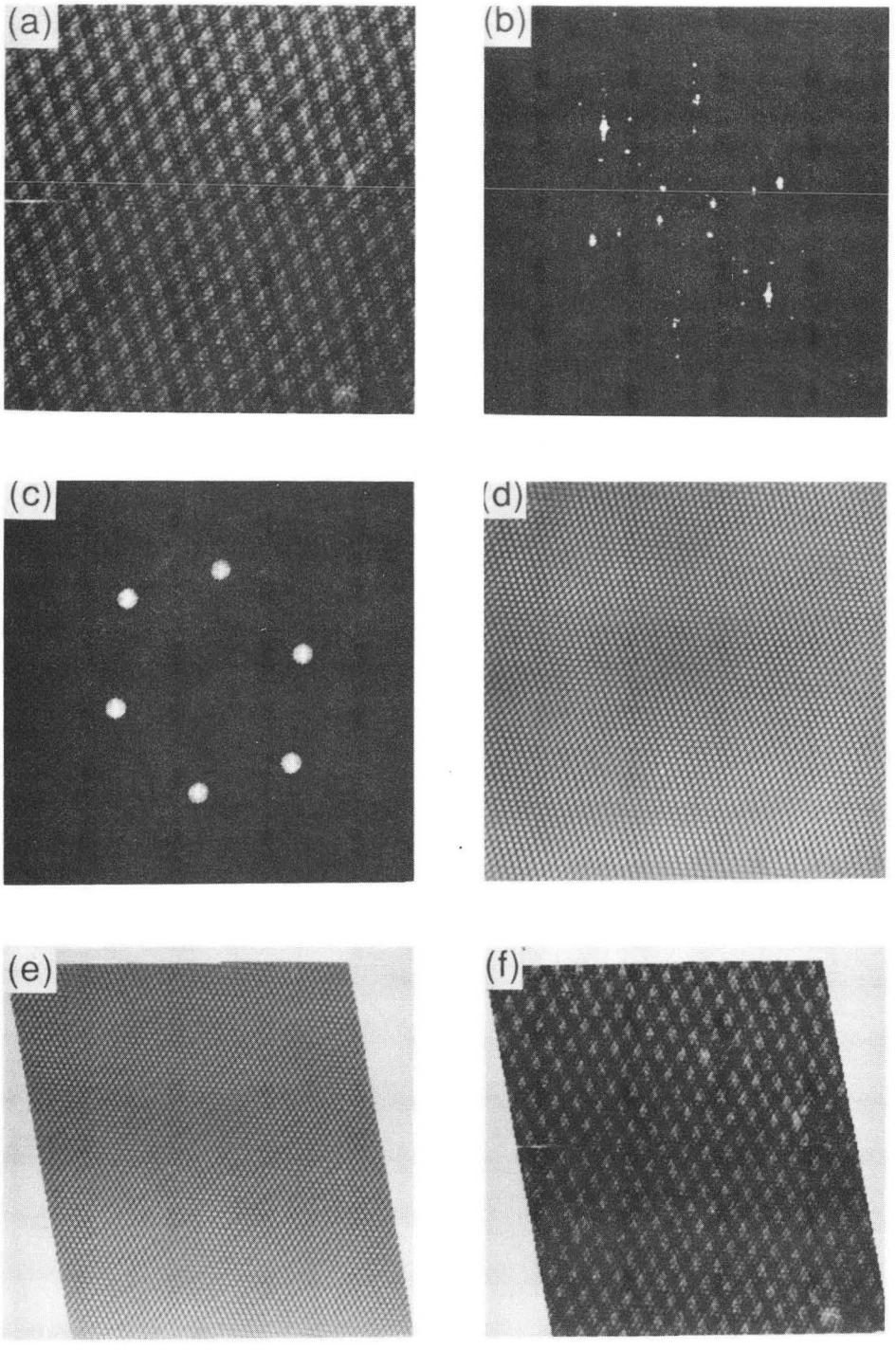


Figure 2-12 (a) Raw STM data of 1T-$TaS_2$ in the I phase (b) FT of (a). (c) Modified FT with only the lattice peaks saved. (d) Back-transform of (c). (e) Same as (d) after being skewed by the CALIB program. (f) Raw data shown in (a) after the linear skewing transform generated for (e) has been applied. (XBB-910-8708)

positions, shown in Fig. 2-12(d). This image can then be used with the program CALIB to produce a linear skewing transform which will map the lattice onto a hexagonal grid. (Many of our images are skewed because of thermal drifts and non-linearities of the scanning drives.) The skewing transform thus calculated can then be applied to the raw data file, as is shown in Fig. 2-12(f). Using the corrected file, measurements such as the orientation of the CDW relative to the lattice can be made.

In addition to the Fourier transform options, the FFT program allows for a wide variety of data manipulations including apodizing the image, measuring the position and intensity of peaks in the FT, various schemes smoothing the data and decreasing the effects of noise, displaying a 3D projection of the data, or deleting various portions of the data. Also, this program has subroutines which can calculate various kinds of model data, so that the STM image one would expect to acquire under various circumstances can be examined. Examples of these models will be used in later chapters. The menu trees for both the CALIB and the FFT programs are given in Appendix A.

[1]W.J.Kaiser and R.C.Jaklevic, Surf. Sci. **181**, 55 (1987).

[2] B.Drake, R. Sonnenfeld, J.Schneir, P.K.Hansma, G.Slough, and R.V.Coleman, Surf. Sci. **181**, 92 (1987).

[3] G. Binnig and D.P.E.Smith, Rev. Sci. Instrum. **57**, 1688 (1986).

[4]B. Drake, R. Sonnenfeld, J. Schneir, and P.K.Hansma, Surf. Sci. **181**, 92 (1987).

[5]E.D.Ganz, Ph.D. thesis, University of California, Berkeley, California 1988.

# Chapter III

## 1T-$TaS_2$: Description of the material

Tantalum disulphide is a member of the family of transition metal dichalcogenides, a group of layered materials which, because of their quasi-two-dimensional structure, exhibit a variety of interesting properties. One of the most frequently studied characteristics of these materials is the charge density wave (CDW) that forms below some critical transition temperature in most of the members of the family. We have used scanning tunneling microscopy to study intensively the CDW in 1T-$TaS_2$ and to resolve some of the remaining questions about the subtleties of its structure.

The transition metal dichalcogenides grow in several different polytypes distinguished by the coordination between the metal and the chalcogen atoms. All of the polytypes consist of one or more three-layer sandwiches, with an inner layer of metal atoms enclosed by layers of chalcogenide atoms. The individual layers of the sandwiches are arranged in hexagonal close-packed planes. Within the three-layer sandwich the atoms are bound by strong covalent interactions, while the bonds between the sandwiches are quite weak, consisting predominantly of van der Waals interactions. This means that crystals of the layer-structure dichalcogenide materials cleave very easily, separating along the planes between the sandwiches and creating atomically-flat surfaces.

For this thesis work I have studied the 1T polytype of $TaS_2$. The 1T polytype has octahedral coordination between the metal

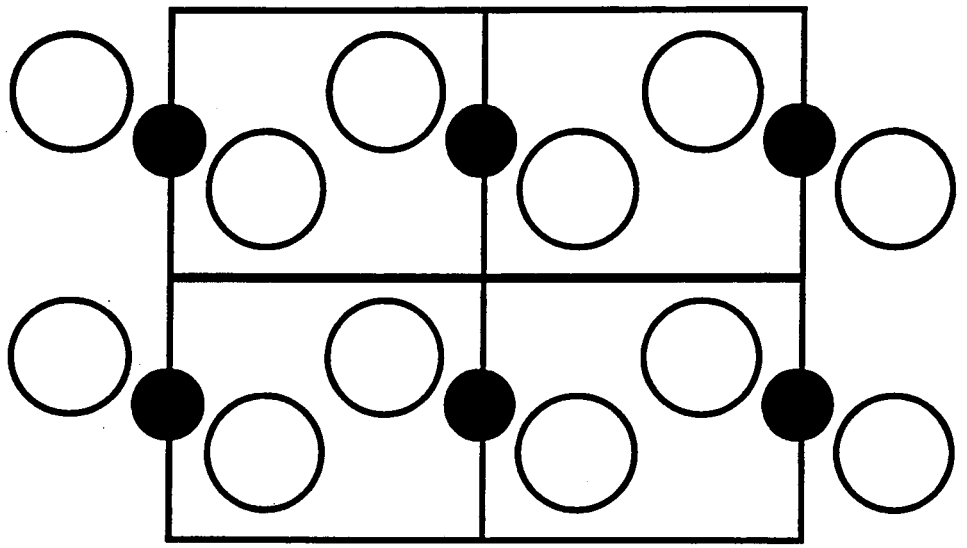

Figure 3-1. Side view of 1T-$TaS_2$ crystal. The larger open circles represent the sulfur atoms while the smaller solid circles represent the tantalum atoms. The material cleaves along the heavy horizontal line.

atoms and the chalcogenide atoms and has only one three-layer sandwich per unit cell[1] (see Fig. 3-1). Because of its high degree of spatial symmetry, the Fermi surface of 1T-$TaS_2$ is also highly symmetric[2] (see Fig. 3-2). This is the necessary condition for the formation of a CDW.

When a material possesses a highly symmetric Fermi surface, it is sometimes possible to lower the total free energy of the system by introducing a slight periodic lattice distortion (PLD). This distortion can be thought of as a static phonon. The PLD creates a gap in the electronic density of states in much the same way that the atomic lattice itself causes a gap at the Brillouin zone edges. If the PLD has a wavevector of $\mathbf{q}=2\mathbf{k}_F$ (where $\mathbf{k}_F$ is the Fermi wavevector), then the gap which it introduces has the effect of lowering the energy for the electronic states lying just below the Fermi energy ($E_F$) and raising the energy of the electronic states lying just above $E_F$. Since the electronic states above $E_F$ are unoccupied while those below $E_F$ are occupied, the net result is to lower the total electronic energy of the system. In the case where the Fermi surface is highly symmetric, a single wavevector $\mathbf{q}$ can gap a large section of the Fermi surface. In this case, the lowering of the electronic energy more than compensates for the lattice strain energy due to the PLD and the distorted state is energetically favorable.

Since the PLD causes a slight change in the positions of the ion cores[3] ($\approx$0.2 Å), the conduction electrons are now subjected to a modified electric potential. This causes the electronic charge density to go from being uniform, as it would be in the undistorted

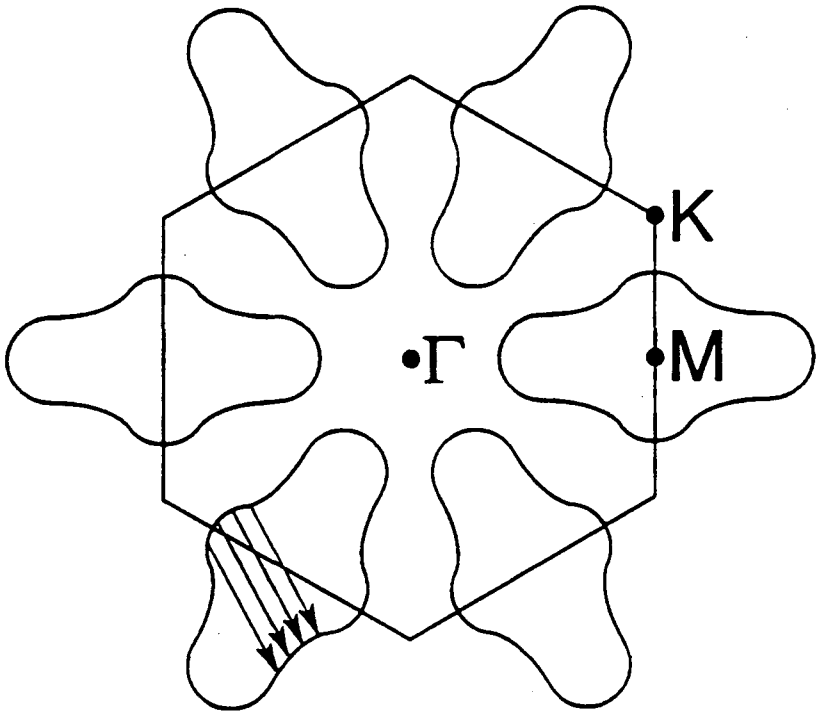


XBL 915-4829

Figure 3-2. Fermi surface of 1T-$TaS_2$ (from Ref. 2).

material, to possessing a distribution known as a charge density wave (CDW). This CDW can be well described by

$$\rho = \rho_o \cos(2k_F x + \phi).$$

The modified electronic charge density is illustrated in Fig. 3-3. Since the electrons which participate in the tunneling current in a scanning tunneling microscope are those near the Fermi energy, the STM is able to image the charge density wave, as was first shown by Coleman *et al.*[4]

It should be noted that since the CDW wavevector is determined by the Fermi surface, it is not, in general, proportional to a sum of the lattice vectors. This implies that the CDW will be incommensurate, that is,

$$n\Lambda_{CDW} \neq i\mathbf{a_o} + j\mathbf{b_o} + k\mathbf{c_o}$$

where n, i, j, and k are integers, $\Lambda_{CDW}$ is the CDW lattice translation vector and $\mathbf{a_o}$, $\mathbf{b_o}$, and $\mathbf{c_o}$ are the atomic lattice translation vectors. The important difference between a commensurate and an incommensurate CDW in the one-dimensional case are illustrated in parts (b) and (c) of Fig. 3-3.

In the case of 1T-$TaS_2$, a triple CDW exists at all temperatures below 543K, with the three standing waves oriented at 120° relative to each other (except in the triclinic phase). When cooled, the material first enters the incommensurate (**I**) phase (543-353K). In this phase the CDW is aligned with the lattice and has a wavelength of 3.53 $a_o$, where $a_o$ is the lattice constant of 3.346Å. Further cooling takes the sample through two first order phase transitions, first into the nearly-commensurate (**NC**) phase (353->183K), and

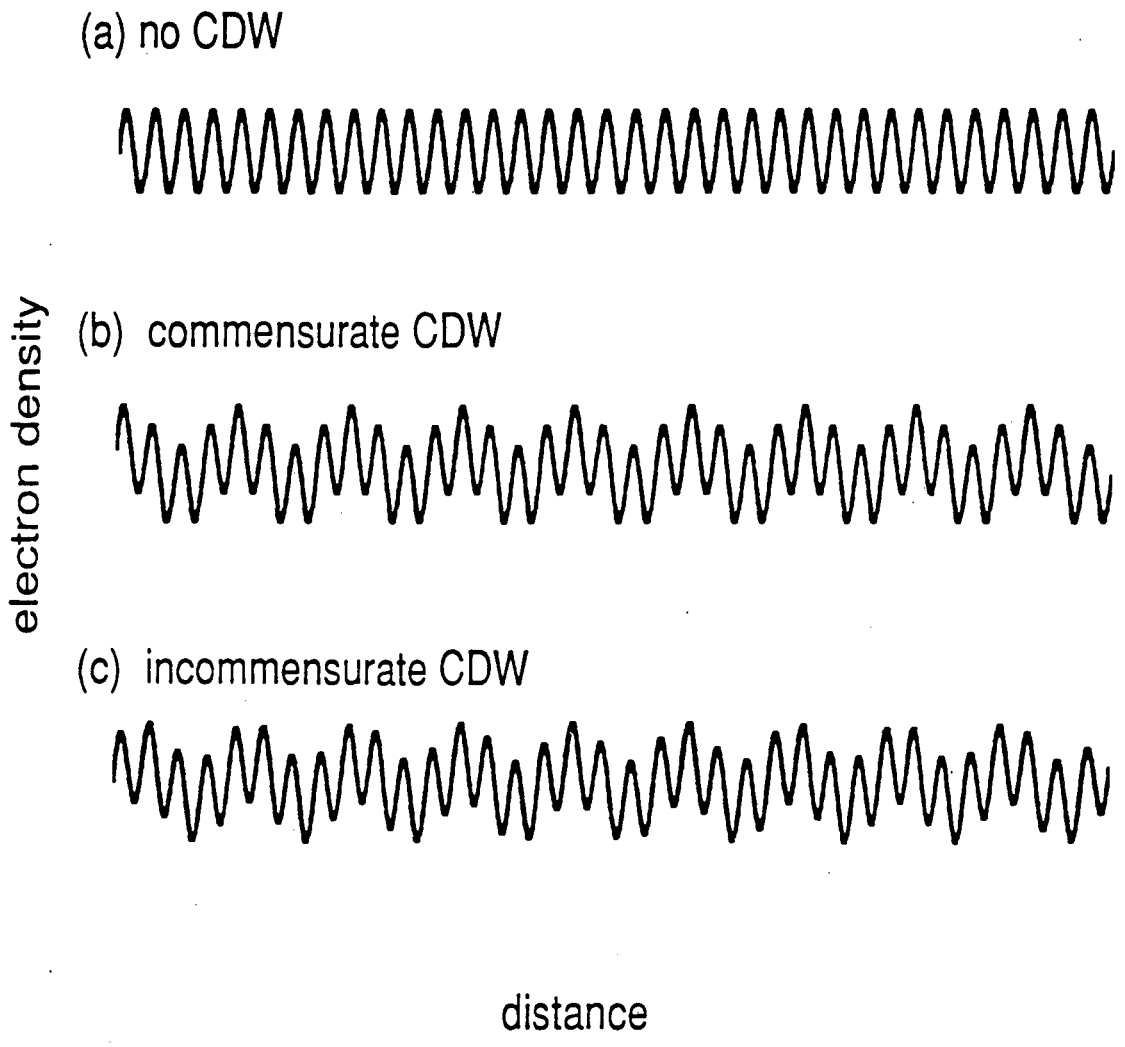


Figure 3-3 (a) The electronic charge density when no CDW is present, (b) when a commensurate CDW is present, and (c) when an incommensurate CDW is present.

finally at T=183K into the commensurate (**C**) phase. In the **C** phase the CDW wavefronts make an angle of $\Phi$=13.9° relative to the lattice and the CDW has a wavelength of 12.06Å, making it fully commensurate with the underlying atomic lattice. The configuration of the CDW relative to the atomic lattice in this phase is displayed in Fig. 3-4. In the **NC** phase the CDW has rotated most of the way towards the commensurate configuration it adopts in the **C** phase,[2] but the angle $\Phi$ is a little less than the commensurate angle of 13.9°, varying from about 11.6° at 331K to 13.1° at 250K. In this phase the CDW wavelength also varies with temperature, but it always has an incommensurate value. Since 1T-$TaS_2$ is strongly hysteretic, on warming it one obtains the nearly commensurate triclinic (**T**) phase (223->283K) followed by a transformation back to the **NC** phase at 283K. In the **T** phase the three simultaneously occurring CDWs are not all oriented with the same angle relative to the lattice, breaking the hexagonal symmetry of the system. In this phase, as in the **NC** phase, the CDW parameters vary with temperature. Table 3-1 summarizes the temperature ranges of these phases and their important characteristics.

The PLD that is concommitant with the CDW can be studied with x-ray diffraction,[2,5] electron diffraction,[2,6] and atomic beam diffraction.[7] In the past these diffraction techniques, along with high-resolution electron microscopy (HREM),[8] have been the major methods that have given insight into the detailed structure of the different phases of the CDW on the atomic scale. For the **NC** and **T**

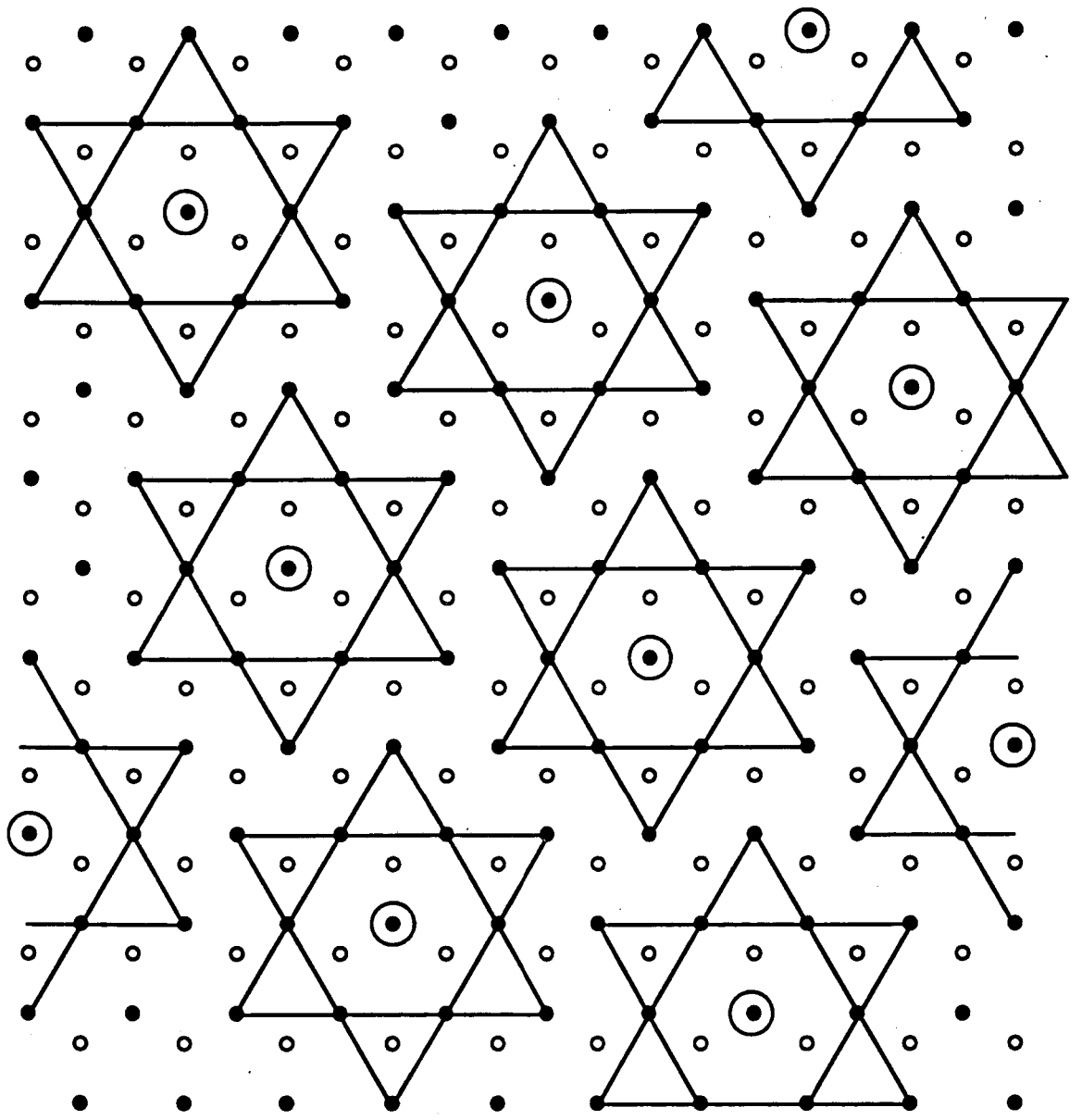

Figure 3-4 Registration of the CDW in the commensurate phase. The small solid circles represent the tantalum atoms, the small open circles represent the sulfur atoms on the surface, and the larger open circles represent the CDW maxima formed by constructive interference of the three CDWs oriented at 120° relative to each other. The periodic lattice distortion draws the inner Ta atoms of the six pointed star towards the center atom by about 0.2 Å, and the outer atoms on the points of the star by a lesser amount.

| Phase | Temperature | Φ (deg) | Comments |
|---|---|---|---|
| Normal | above 543 K | | No CDW is known to exist. Difficult to study because it transforms to the 2H polytype. |
| I | 543>T>354K | 0 | CDW is uniformly incommensurate but is aligned with the atomic lattice. |
| NC | T↑ 353<T<183K<br>T↓ 283<T<253K | 11.6°<br>to<br>13.1° | CDW is incommensurate and rotated away from the lattice. Hexagonal domain structure found to be present |
| C | T↑ T<183K<br>T↓ T<223K | 13.9° | CDW is uniformly commensurate. |
| T | T↓ 223<T<283K | 12-13° | CDW loses its hexagonal symmetry. Discommensurate stretched honeycomb domain structure found to be present. |

Table 3-1. The phases of the CDW in 1T-$TaS_2$.

phases of 1T-$TaS_2$, diffraction techniques have proven indispensable in providing basic data to determine the quite complicated temperature-dependent structure. However, there was still the challenging question of how these two phases are actually arranged on an atomic scale within a single layer, i.e., whether they are continuously incommensurate, or form a domainlike discommensurate structure. In the latter case, the CDW was proposed to be commensurate within a single domain and incommensurate only over a finite width at the domain boundaries. This situation was proposed by Nakanishi and Shiba,[9,10] using a theory first developed by McMillan,[11] to explain x-ray diffraction data.

In 1976 McMillan proposed that the lowest energy state of an incommensurate CDW near a lock-in transition was a distorted plane wave. This theory applies to some systems where there is some interaction between two periodic properties which have non-proportional periods (in this case the CDW and the atomic lattice). In such a system, it is often the case that one term in the free energy would be lower if the two lattices became commensurate. Therefore, there exists a competition between the terms in the free energy that determine the individual periodicities of the two lattices and the term that promotes their commensurability. Depending on the relative magnitude of these terms, the system may adopt a discommensurate configuration. In this case, the two properties become locally commensurate within domains, and undergo phase slips at the domain walls, called discommensurations, that preserve the average incommensurate periodicities.

Discommensurations (DCs) have been found to exist in such diverse systems as ferroelectrics,[12] absorbate monolayers on semiconductor surfaces,[13] mass density waves in graphite intercalation compounds[14] and, the system for which they were first proposed, charge density waves in layered dichalcogenides.[15] In several materials, especially 2H-$TaSe_2$, CDW DCs are readily observable with scanning transmission microscopy because the domains are relatively large (300 Å).[16] However, because the domains in 1T-$TaS_2$ would be much smaller, domains and DCs in this material have been much harder to verify. (The size of the domain depends solely on the mismatch between the closest commensurate wavevector and the average wavevector, which is known from diffraction studies.)

In the case of 1T-$TaS_2$, in both the **NC** phase and the **T** phase the CDW is close to being commensurate. Theoretical calculations for these phases have predicted discommensurate models for these two phases. For the **NC** phase,[9] the model predicts hexagonal domains which are about 70 Å across at room temperature. A schematic of the **NC** model is shown in Fig. 3-5. For the **T** phase,[10] a stretched-honeycomb model was calculated. In this case the predicted domains are about 250 Å long and only about 40 Å wide. Figure 3-6 is a schematic of the proposed discommensurate model for the **T** phase. Both models predict that the CDW will exhibit amplitude as well as phase (orientation) modulations, with the CDW amplitude greater in the center of the domains where it is commensurate, and lower at the DCs, where the CDW undergoes its phase slip. The DCs themselves consist of a slip of one atomic

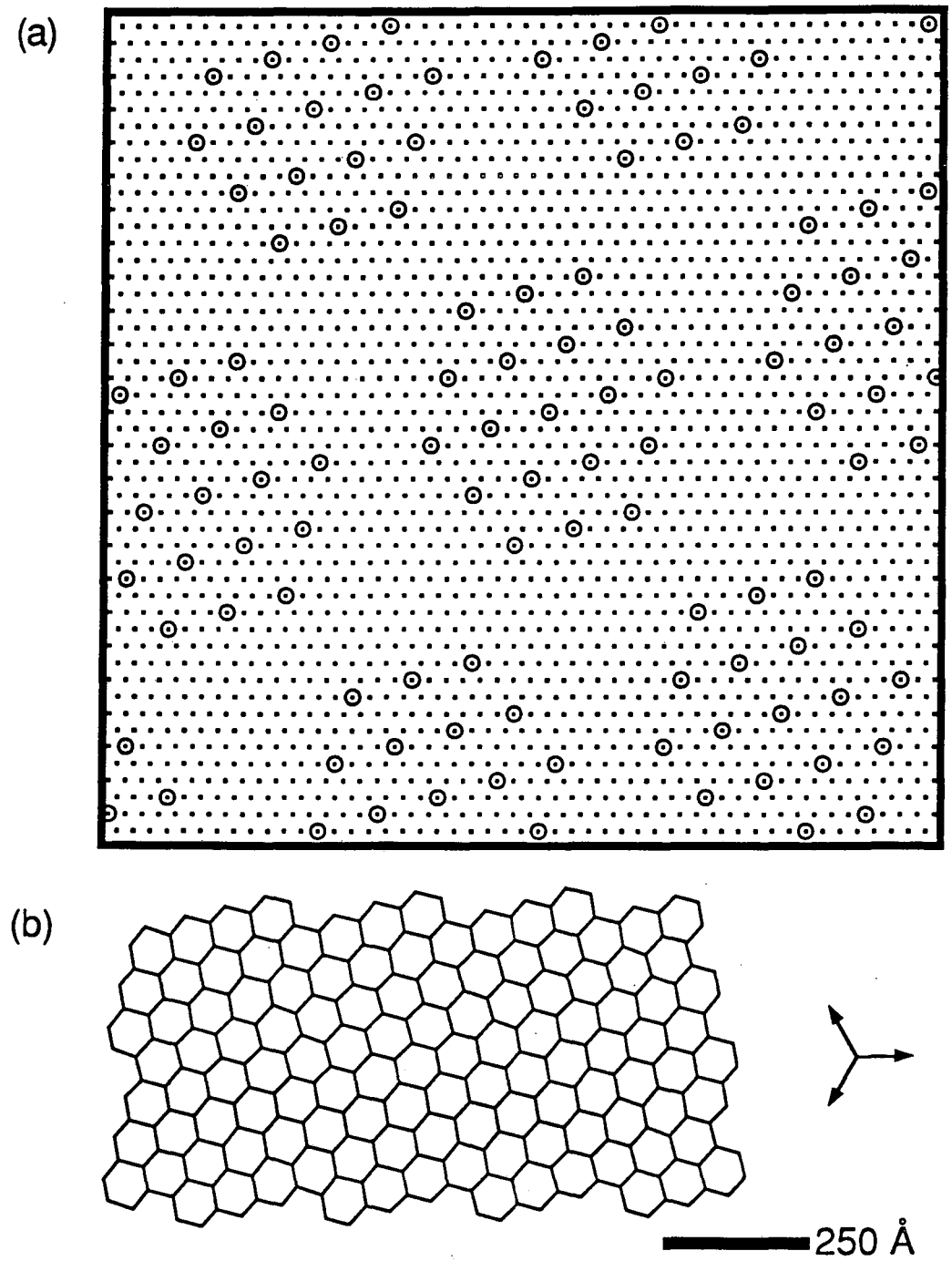


Figure 3-5 Schematics of the **NC** phase model proposed by Nakanishi and Shiba. (a) Small scale structure showing the registration of the CDW maxima relative to the Ta lattice. (b) Large scale structure illustrating the size and orientation of domains.

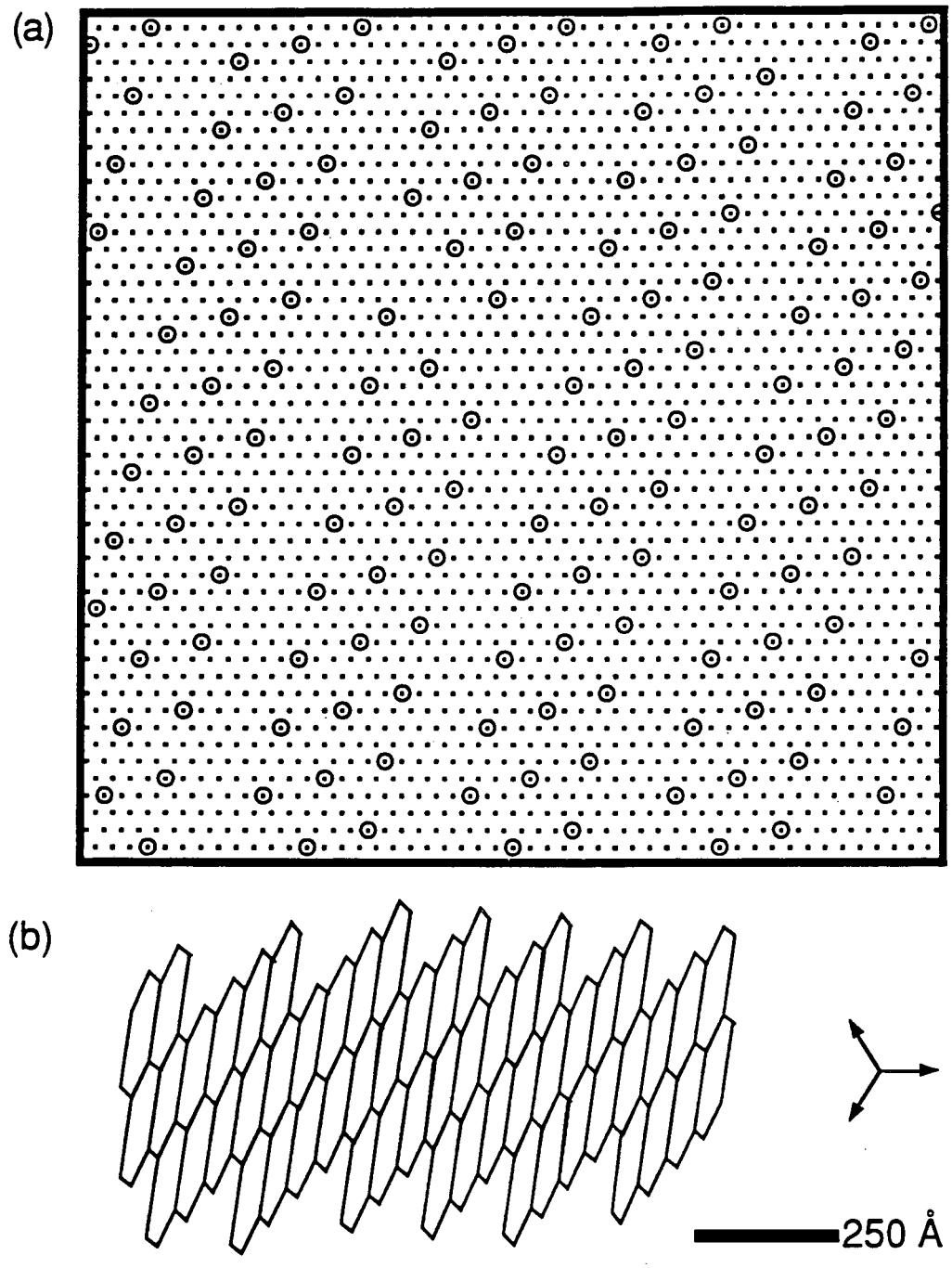


Figure 3-6 Schematics of the **T** phase model proposed by Nakanishi and Shiba. (a) Small scale structure showing the registration of the CDW maxima relative to the Ta lattice. (b) Large scale structure illustrating the size and orientation of domains.

lattice unit by the CDW, in the direction which causes the CDW wavevector averaged over several domains to approach the uniformly incommensurate wavevector required by the geometry of the Fermi surface.

It should be noted that both of these models include adjustable parameters. Although the main attributes of the models remain constant, the degree of variation in amplitude and phase are not determined theoretically. In particular, these models do not require a CDW that locks in to the commensurate wavevector inside the domains. The models can encompass all cases ranging from very slight variations from a uniform orientation to a fully-locked in orientation where the CDW becomes fully commensurate within the domain.

Many experiments have been performed looking for evidence of these domains and discommensurations. Before the invention of STM, x-ray diffraction studies[9,10] not only supported the domain models, but actually provided the original data upon which the models were based. The x-ray photoemission study of Hughes and Pollack[17] was for many years the only other piece of experimental evidence supporting the domain models. This study showed that the x-ray photoemission spectrum of the *4f* lines of the Ta atoms are split, indicating two inequivalent sites for the Ta atoms. However, two high resolution electron microscopy studies[8] that achieved atomic resolution on the **NC** phase of 1T-$TaS_2$ reported that the CDW was uniformly incommensurate and found no evidence of phase slips, in contradiction with the DC theories.

In 1988 the first STM study that considered the question of the existence of domains in 1T-$TaS_2$ (part of this thesis work) was published.[18] This study found clear evidence for domains in the **T** phase but not in the **NC** phase. Subsequent studies by several groups[19] have reached a variety of conflicting conclusions about the existence and nature of the domains in the **NC** phase. The studies reported in this thesis cover all four phases of 1T-$TaS_2$ and consider the question of the existence of domains in the **NC** and **T** phases in depth. I have also examined in some detail several of the subtler points which must be considered to distinguish data with domains from uniformly incommensurate data.

The samples used in the early part of this study were supplied by P. Rauch working in F. J. DiSalvo's laboratory at Cornell University. These samples were prepared from Ta powder (99.9%-pure Wah Chang) and S (99,9999%-pure Atomergic Chemetals) in stoichiometric amounts sealed in quartz tubes (200 mm long, 16 mm i.d.) along with 58 mg of excess S (approximately 1$\mu g/mm^3$ of tube volume) and 100 mg of iodine. After the tubes were slowly heated to 550°C, and examined for complete reaction of the tantalum with the sulfur, they were heated to 900°C to complete the formation of $TaS_2$. Single crystals of the 1T polytype were grown by placing the tubes in a temperature gradient from 843 to 768°C for three weeks. The tubes were then rapidly quenched in water to retain the 1T polytype, and the crystals washed three times with dichloromethane to remove any residual iodine.

Samples used in the later experiments were prepared by my coworker, B. Burk, working in A. Zettl's laboratory here at the

University of California. These samples were prepared from Ta wire (99.9%-pure Alpha) and S (99.999%-pure Fluka) in stoichiometric amounts sealed in quartz tubes (20.0-cm long, 2.4-cm i.d.) along with 80 mg of excess S (approximately 1 mg/cm$^3$ of tube volume) and 320 mg of iodine (99.999%-pure Fisher). The temperature gradient used in this case was from 950 to 875°C and the quartz tubes were heated for two weeks. The tubes were then rapidly quenched in water to retain the 1T polytype.

[1]P.M.Williams, *Crytallography and Crystal Chemistry of Materials with Layered Structures*, edited by F.Lévy (D. Reidel Publishing Company, Dordrecht-Holland, 1976), p.51.

[2]C.B.Scruby, P.M.Williams and G.S.Parry, Philos. Mag. **31**, 225 (1975).

[3]R.Brouwer and F.Jellinek, Physica B+C **99B**, 51 (1980).

[4]R.V.Coleman, B.Drake, P.K.Hansma and G.Slough, Phys. Rev. Lett. **55**, 395 (1985).

[5]S. Tanda and T. Sambongi, Synth. Methods **11**, 85 (1985); S. Tanda, T. Sambongi, T.Tani and S.Tanaka, J. Phys. Soc. Jpn. **53**, 201 (1985).

[6]R.L.Withers and J.W.Steeds, J.Phys. C **20**, 4019 (1987); J.A.Wilson, F.J.DiSalvo and S. Mahajan, Adv. Phys. **24**, 117 (1975).

[7]P.Cantini, G. Boato and R. Corella, Physica B+C **99B**, 59 (1980).

[8]M.Kuwabara, M.Tomita, H.Hashimoto and H.Endoh, Phys. Status Solidi A **96**, 39 (1986); G. van Tendeloo, J.van Landuyt, and S.Amelinckx, Phys. Status Solidi A **64**, K105 (1981).

[9]K.Nakanishi, H.Takatera, Y.Yamada and H.Shiba, J. Phys. Soc. Jpn. **43**, 1509 (1977); K. Nakanishi and H. Shiba *ibid.* **43**, 1893 (1977).

[10]K.Nakanishi and H.Shiba, J. Phys. Soc. Jpn **53**, 1103 (1984).

[11]W.L.McMillan, Phys. Rev. B **14**, 1496 (1976).

[12]H.Bestgen, Solid State Commun. **58**, 197 (1986).

[13]A.B.McLean, R.M.Feenstra, A.Taleb-Ibrahimi and R.Ludeke, Phys. Rev. B **39**, 12925 (1989).

[14]R.Clarke, J.N.Gray, H.Homma and M.J.Winokur, Phys. Rev. Lett. **47**, 1407 (1981).

[15]C.H.Chen, J.M.Gibson and R.M.Fleming, Phys. Rev. Lett. **47**, 723 (1981).

[16]C.H.Chen, J.M.Gibson and R.M.Fleming, Phys. Rev. Lett. **47**, 723 (1981); Phys. Rev. B **26**, 184 (1982); K.K.Fung, S.McKernan, J.W.Steeds and J.A.Wilson, J. Phys. C **14**, 5417 (1981); T.Onozuka, N.Otuska and H.Sato, Phys. Rev. B **34**, 3303 (1986); Y.Koyama, Z.P.Zhang and H.Sato, *ibid.* **36**, 3701 (1987).

[17]H.P.Hughes and R.A.Pollack, Commun. Phys. **1**, 61 (1976).

[18]R.E.Thomson, U.Walter, E.Ganz, J.Clarke and A.Zettl, Phys. Rev. B **38**, 10734 (1988).

[19]G.Gammie, S.Skala, J.S.Hubacek, R.Brockenbrough, W.G.Lyons, J.R.Tucker and J.W.Lyding, J. of Microsc. **152**, 497 (1988); X.L.Wu and C.M.Lieber, Phys. Rev. Lett. **64**, 1150 (1990); C.G.Slough, W.W.McNairy, C.Wang and R.V.Coleman, J. Vac. Sci. Technol. B **9**, 1036 (1991).

# Chapter IV

## **C** phase

Because it is the simplest phase to understand, I begin my discussion of 1T-$TaS_2$ with a discussion of the **C** phase. In this phase, which occurs at temperatures below 180K, the CDW is completely commensurate with the underlying atomic lattice. Figure 4-1 displays the filtered STM data taken at 150K. It is clear that both the CDW and the underlying atomic lattice are visible. Moreover, it is evident from the STM image that the CDW is commensurate with the atomic lattice, since the lattice structure within each CDW maximum appears to be identical. The commensurate CDW present in this temperature range is well-known from x-ray diffraction studies[1] to be a hexagonal superlattice with a $\sqrt{13}\,\mathbf{a}_o \times \sqrt{13}\,\mathbf{a}_o$ unit cell rotated 13.9° from the unreconstructed unit cell of the atomic lattice (see Fig. 3-4). This is indeed the superlattice we find in our STM images of 1T-$TaS_2$ in the **C** phase.

In the **C** phase as well as the other CDW phases we find that the CDW supercell can be rotated counterclockwise ($\alpha$ rotated in the notation of Wilson *et al.*[2]), as it is in Fig. 4-1, or clockwise (ß rotated), relative to the lattice, as is shown in Fig. 4-2. It is well known from x-ray diffraction experiments that these two related superstructures can coexist in the same sample. On one occasion we found adjacent areas of $\alpha$ and ß rotation, but were unable to image the domain boundary. In all other cases, we have observed only one type of rotation across the entire surface area accessible to our

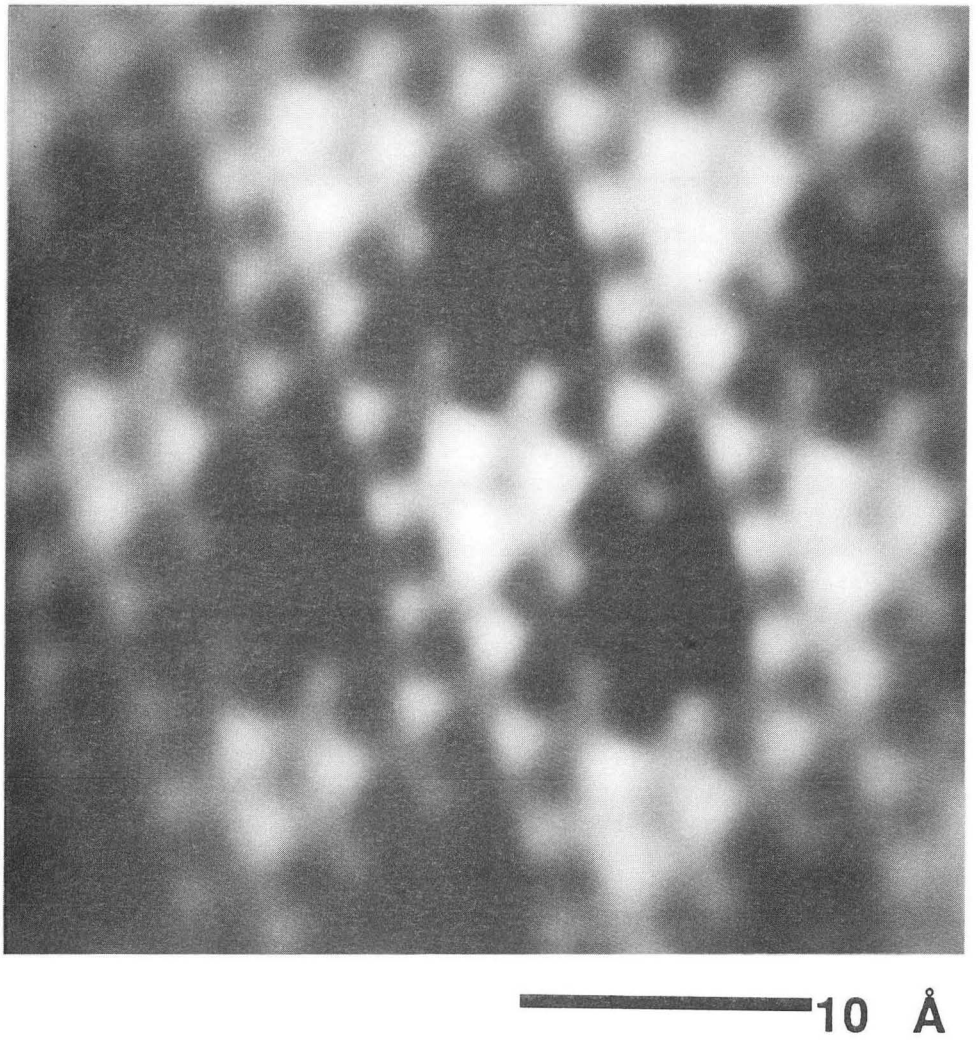


Figure 4-1 Filtered STM data in the α rotation taken at 150K in the C phase. (XBB-915-3886)

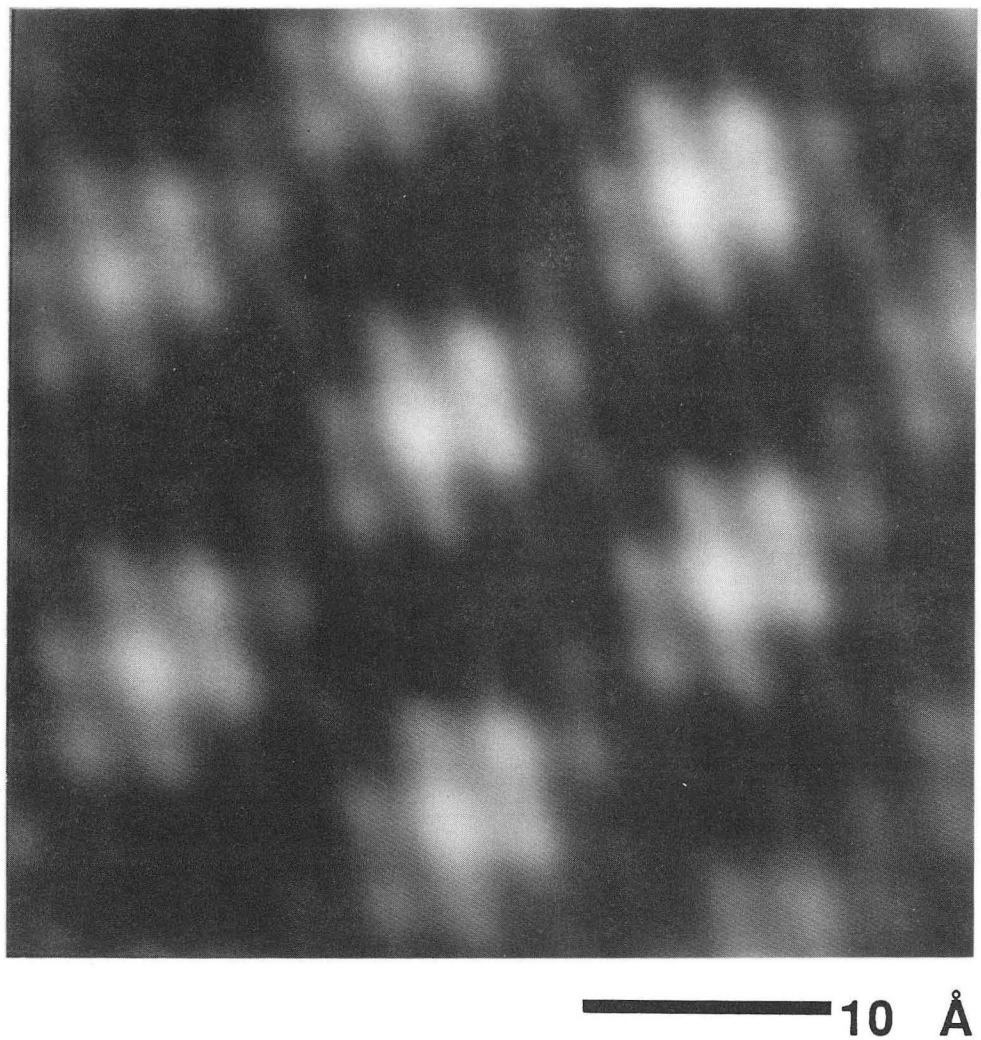


Figure 4-2 Filtered STM data in the β rotation taken at 150K in the **C** phase. (XBB-915-3887)

microscope (about 1 $\mu m^2$ at room temperature).

One surprising property of both Figs. 4-1 and 4-2 is the asymmetry of the CDW maxima. If the CDW in the tantalum layer forms the star-of-David pattern shown in Fig. 3-3, as has been the assumption in the field for many years, then the registration of the CDW in the sulfur layer should have an $\mathbf{a}_0/\sqrt{3}$ displacement from the registration in the Ta layer and should appear similar to that shown in Fig. 4-3.

Figure 4-3 is an example of model data we generate on the Tektronix computer to compare to our real STM data to help elucidate various aspects of the STM data. The model data is generated by superimposing three sine waves to represent the atomic lattice and three additional sine waves which produce the commensurate CDW. The CDW has been constructed to be at an angle of $\Phi$=13.9° relative to the lattice and to have a wavevector of $\lambda=\sqrt{13}\mathbf{a}_0$, which are the values of $\Phi$ and $\lambda$ for a commensurate CDW. The amplitude of the CDW has been chosen to be three times the amplitude of the atomic lattice in agreement with the ratio suggested by real STM images.[3] I will use similar models again in later chapters to elucidate other aspects of the CDW structure.

It is clear from Fig. 4-3 that the asymmetry in the real STM images of 1T-$TaS_2$ in the **C** phase cannot be explained by the phase shift introduced by the $\mathbf{a}_0/\sqrt{3}$ displacement between the surface sulfur atoms and the underlying tantalum atoms which support the CDW. We find a wide variety of atomic registrations in our **C** phase STM images. Examples of the apparent registrations we observe are shown in Fig. 4-4.

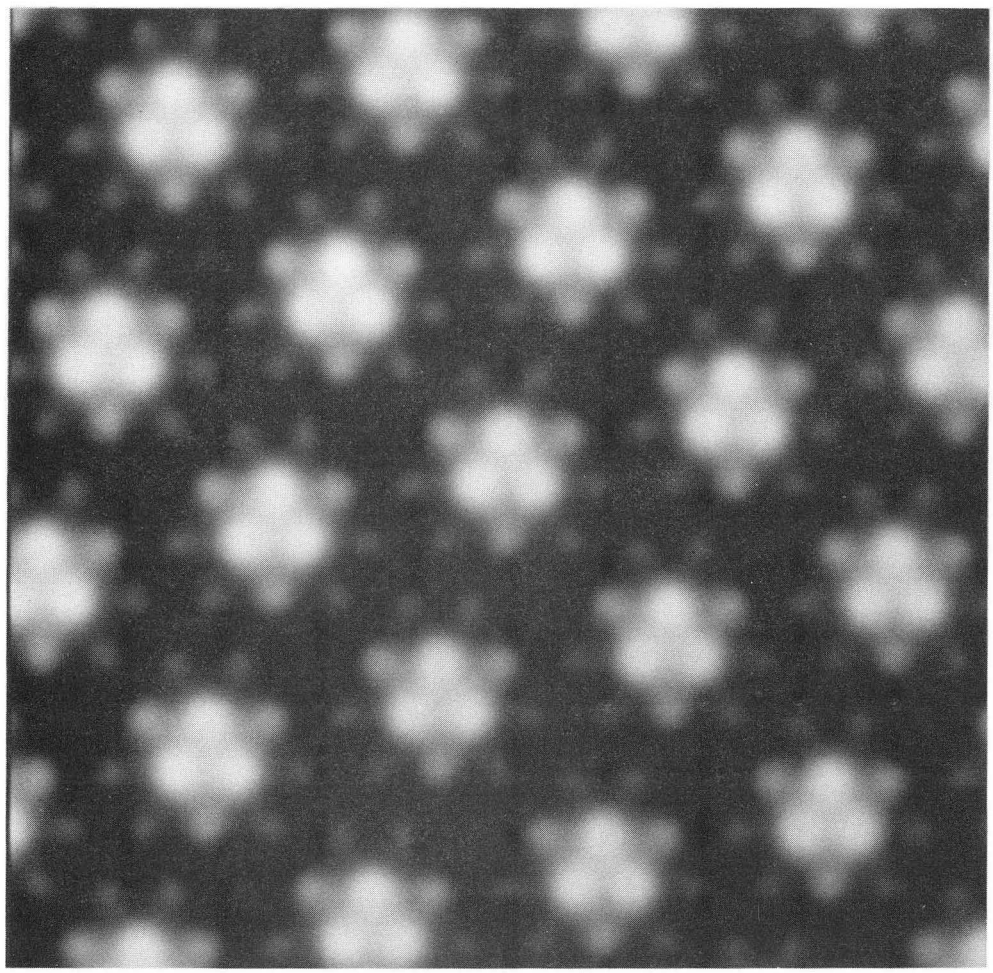

Figure 4-3 Computer simulation of ideal data for 1T-$TaS_2$ in the **C** phase. (XBB-916-4340)

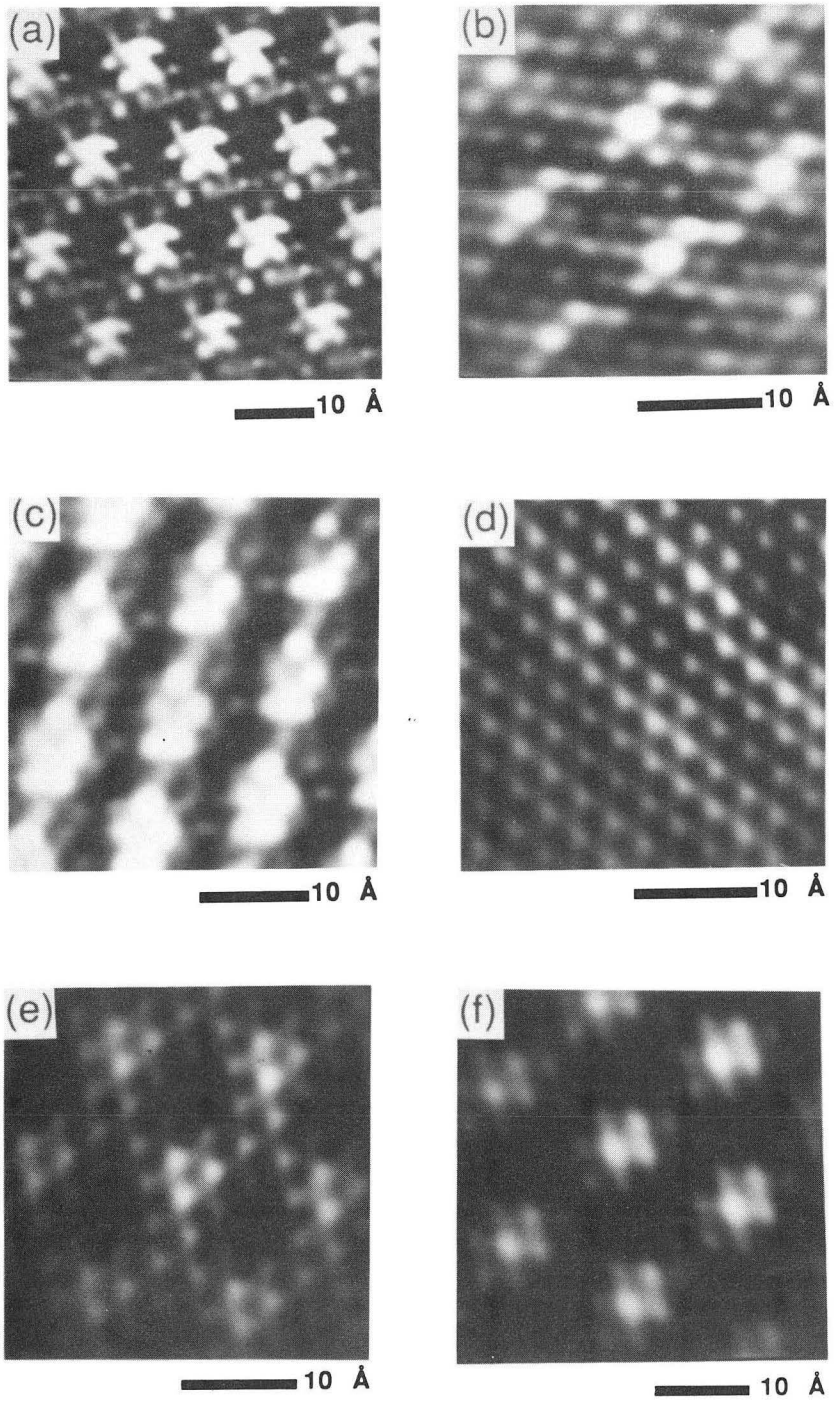


Figure 4-4 Six examples of the variety of registrations we observe in the STM images of samples in the **C** phase. All of these images have been filtered. (a), (b) (d) and (f) are in the β phase while (c) and (e) are in the α phase. (XBB-916-4627B)

The explanation for this observation comes from a well-known property of the STM: namely, STM images can be multiple images that have been superimposed. This occurs when the STM tip does not terminate in a single atom through which all of the tunneling current passes. In this case, at least two atoms on the tip contribute to the tunneling current. Since these two atoms can conceivably be at an arbitrary distance and orientation to each other, as well as being at different heights above the surface, the effect is to add together two or more STM images with an arbitrary offset and relative amplitude. This is a well-known effect present in many STM images of materials such as graphite[4].

In order to elucidate the types of effects double tips can have on an STM image, I display a computer simulations of double tip data. Figure 4-5(a) was generated in a similar way to Fig. 4-3, with the original Fig. 4-3 multiplied by 2 and offset by 6 lattice units to the right and added to the original Fig. 4-3. The result is an image with asymmetrical CDW maxima similar to those seen in the real STM data. Figure 4-5(b) was generated in the same way except that in this case three images of equal intensity were offset from each other by a single lattice vector and added together. Similar simulations can produce images mimicking any other atomic registration by simply varying the offset and relative amplitude of the two separate images which are then added together.

This idea of double tip images also explains the data reported by Sattler *et al.*[5] on 1T-$TaSe_2$.

As is clear from Figs. 4-1 and 4-2, both the atomic lattice and the CDW is clearly visible in our STM images. This is also true at all

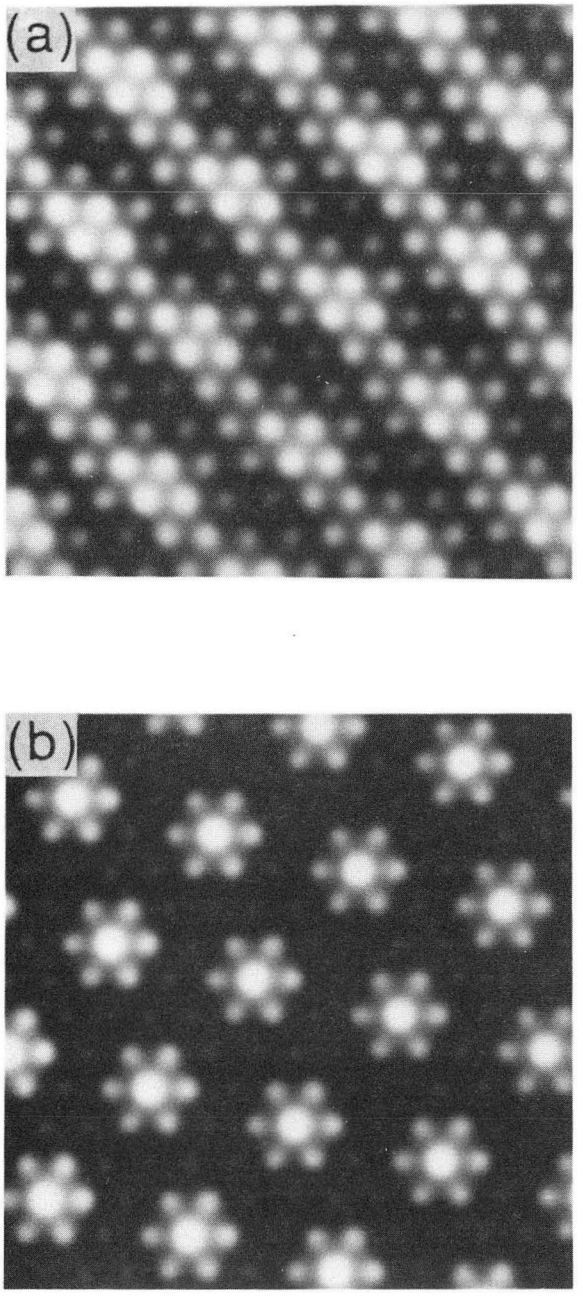


Figure 4-5 Examples of the types of images that can be generated by double (or triple) STM tips. These images are computer generated examples similar to Fig. 4-3, except that in (a) two images of Fig. 4-3 were offset from each other by six lattice units and added together and in (b) three images were offset by one lattice vector and added together. (XBB-919-7085A)

of the other temperatures at which we have taken data as will be seen in later chapters. This is in contrast to the work of Coleman *et al.*[6] who observe only a weak atomic modulation superimposed on a dominant CDW modulation. The explanation for this discrepancy lies with the fact that our images are acquired in the current imaging mode while those of Coleman *et al.* are acquired in the height imaging mode. The difference of image acquisition in these two modes can be determined using the theory developed by Tersoff.[7] This theory predicts the STM response in a few very special cases (of which a CDW is one) where the Fermi surface has collapsed to a single point in the corner of the surface Brillouin zone. In this case, the STM image corresponds, in effect, to an individual state. If we name the wavevector of this state $k_F$, the STM image obtained in the height imaging mode is proportional to $\ln(\sin^2\eta)$, while that obtained in the current imaging mode has an intensity proportional to $\sin^2\eta$, where $\eta = k_F x_t$. Here $x_t$ is the tip position along (parallel to) the sample surface. This means that the data acquired in height imaging mode reflects pathological nodes where $\ln(\sin^2\eta)$ goes to $-\infty$, while that acquired in current imaging mode does not have these nodes.

This fact explains the anomalously large corrugations observed at the CDW wavelength by Coleman *et al.*[6] Since the CDW corrugations are anomalously large in this case, the relative contribution of the atomic lattice is correspondingly smaller. Our method of using the current imaging mode is not affected by this problem, and so the apparent CDW modulation is very comparable to the apparent atomic modulation in most of our images.

[1]C.B.Scruby, P.M.Williams, and G.S.Parry, Philos. Mag. **31**, 255 (1975).

[2]J.A.Wilson, F.J.DiSalvo, and S.Mahajan, Adv. Phys. **24**, 117 (1975).

[3]B. Giambattista, A. Johnson, W.W.McNairy, C.G.Slough and R.V.Coleman, Phys. Rev. B **38**, 3545 (1988).

[4]H.A.Mizes, S.Park, and W.A.Harrison, Phys. Rev. B **36**, 4491 (1987).

[5]K.Sattler, U.Mueller, J.Xhie, N.Venkatesvaren and G.Raina, Bull. Am. Phys. Soc. **35**, 208 (1990).

[6]R.V.Coleman, B.Giambattista, P.K.Hansma, A.Johnson, W.W.McNairy and C.G.Slough, Adv. Phys. **37**, 559 (1988).

[7]J.Tersoff, Phys. Rev. Lett. **57**, 440 (1986).

# Chapter V

## **I** phase

The second phase of 1T-$TaS_2$ that I will discuss is the incommensurate (**I**) phase. This phase occurs between 543K and 354K. In this phase the CDW is aligned with the lattice, although the CDW wavevector is incommensurate. At 354K the material undergoes a first order phase transition to the **NC** phase. We have studied the transition from the **I** to the **NC** phase with care because the rather large rotation ($\Phi \approx 11°$) of the **q** wave vector of the CDW relative to the lattice enables one to observe the transition in real time. This transition is quite dramatic since the in the **I** phase the CDW is aligned with the hexagonal atomic lattice so that the rotation of the CDW superlattice is observed directly.

Figure 5-1 shows the measured resistivity of our sample around the transition. In accordance with previous transport measurements[1] we find that the resistivity shows a small but significant hysteresis of 2K at the transition. In Fig. 5-2 I display the filtered data taken well above the transition (T = 360 K). The underlying atomic lattice is clearly visible in this image and thereby serves as a reference for the CDW. Examination of the details of the image will reveal that the CDW ($\lambda_{CDW} \approx 12$ Å) is aligned with the atomic lattice ($a_o = 3.346$ Å) at this temperature. Figure 5-3 shows the filtered STM image taken just below the transition. We find that after the transition the CDW has rotated by 10.9° relative to its position before the transition (or equivalently, relative to the atomic lattice) and is now in the **NC** phase. To determine whether

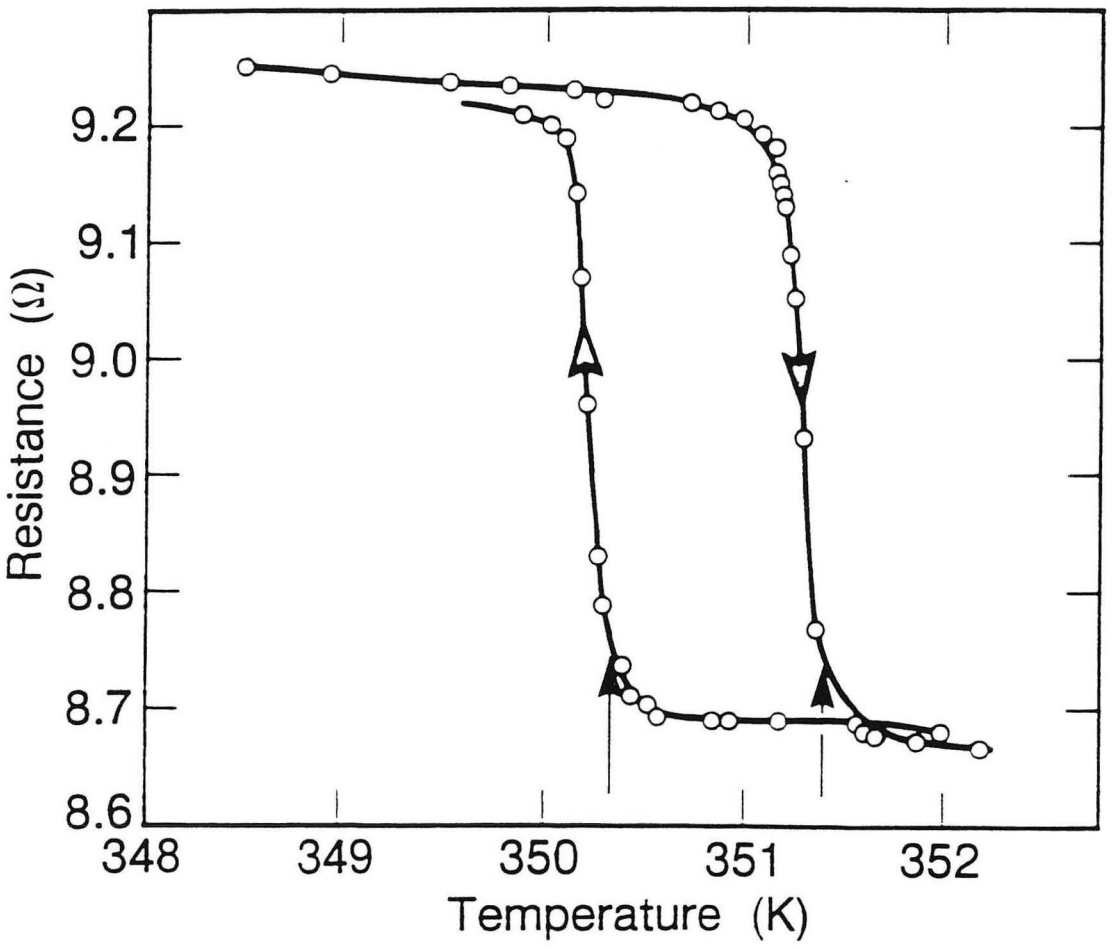


Figure 5-1 The measured resistivity of our sample around the **I** to **NC** transition.

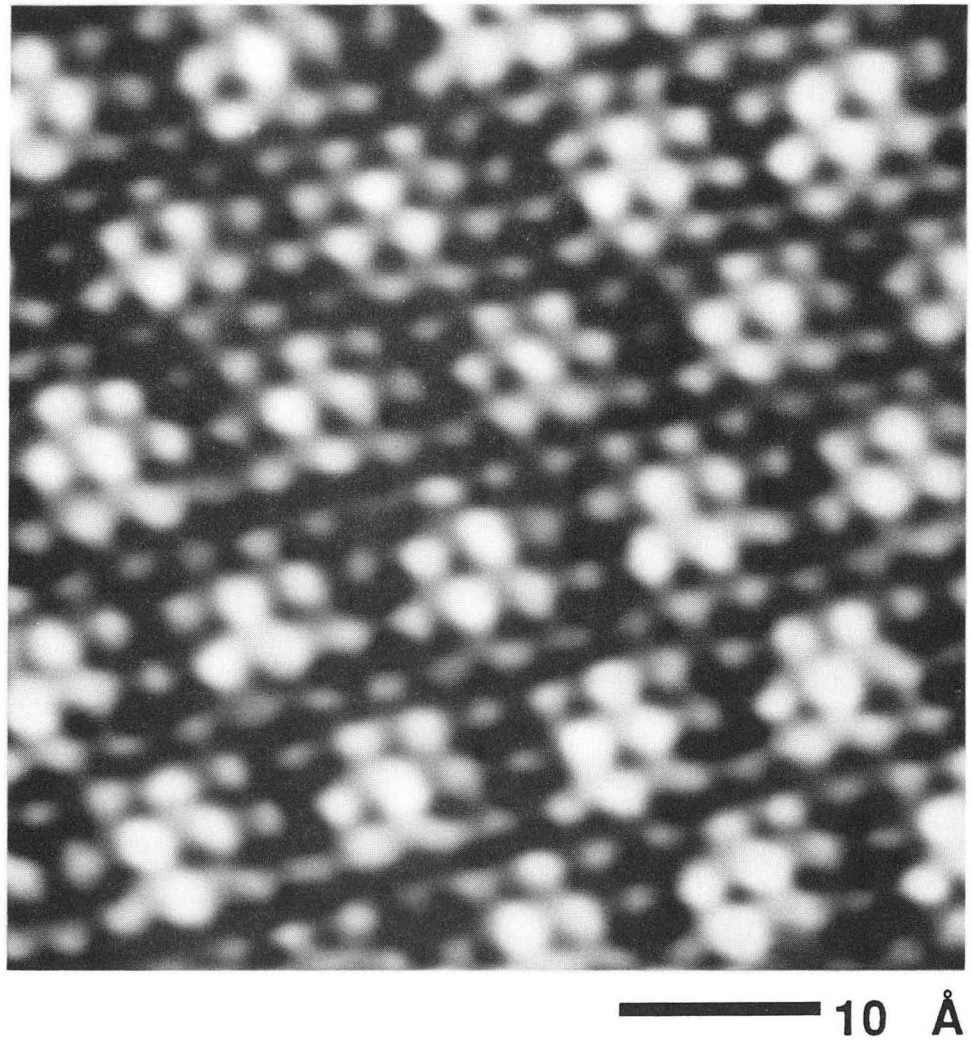


Figure 5-2 Filtered STM data taken in the **I** phase well above the transition (T = 360 K). (XBB-882-755)

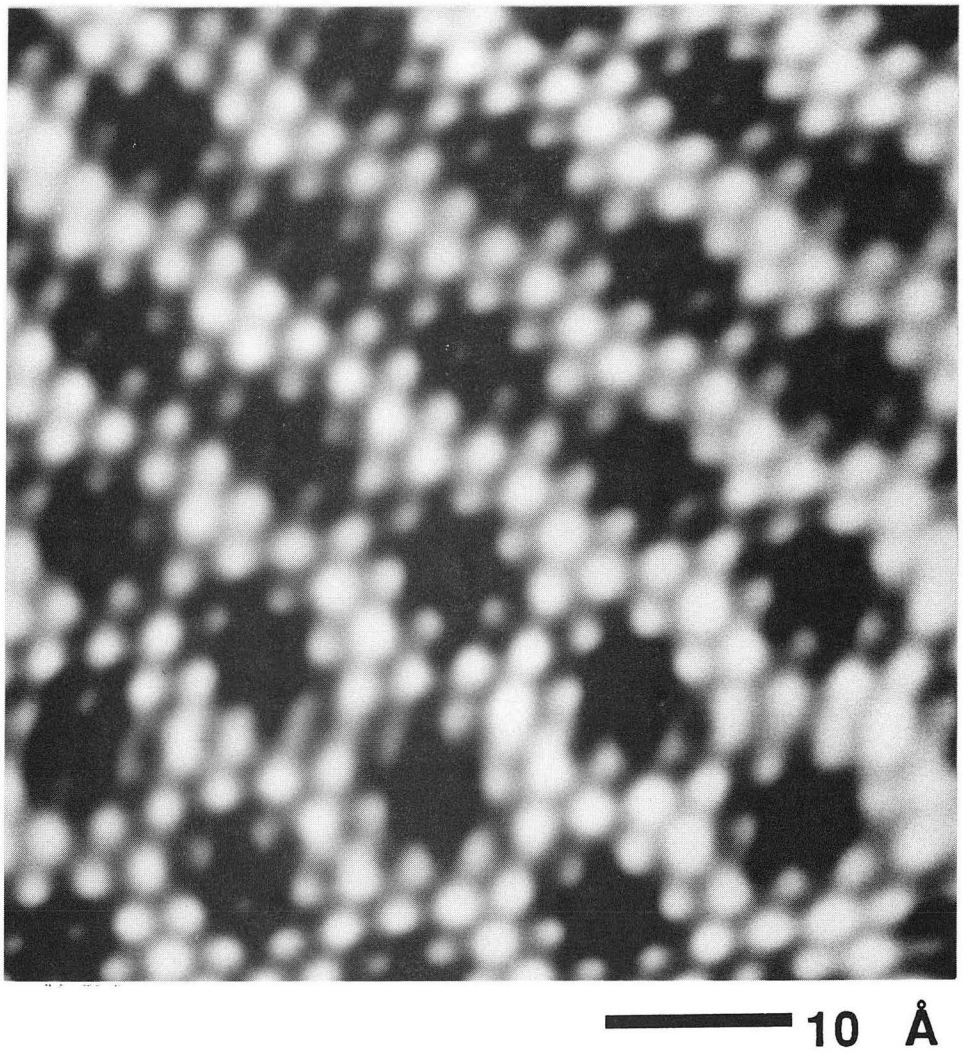


Figure 5-3 Filtered STM data taken just below the transition in the **NC** phase. (XBB-883-2151)

the surface transition occurs at the same temperature as the bulk transition we have also studied the transition for both increasing and decreasing temperature, continuously monitoring any changes in the CDW structure relative to the lattice, while simultaneously measuring the bulk resistivity. We were able to capture the surface transitions, indicated in Fig. 4-1 by the vertical arrows, to within a few hundredths of a kelvin. Obviously, the differences between the bulk and surface transitions are very small, comparable to our estimates of temperature gradients between the sample and thermometer. We therefore conclude that the nature of the transition is the same at the surface as in the bulk, suggesting that the CDW structure should be identical.

This fact also supports the assumption that the CDW structure we observe is identical to the undisturbed CDW structure, although we are applying a small (0.1 - 20 mV) bias between the scanning tip and the sample surface. Tunneling studies[2] of 1T-$TaS_2$ show that the CDW gap is about 0.1 - 0.5 V over the 150 - 320 K temperature range. We can safely assume, therefore, that the tunneling current is only a small perturbation to the static CDW. This conclusion is further supported by the fact that the STM images do not depend significantly on the amplitude or the polarity of the bias voltage.

An extremely interesting property of the CDW in the I phase becomes apparent only upon examination of the Fourier transform. If we take the Fourier transform of a larger area image such as that shown in Fig. 5-4(a), we obtain the very complicated pattern of peaks shown in Fig. 5-4(b). These peaks are quite reminiscent of the satellite peaks present in the Fourier transform when the CDW is

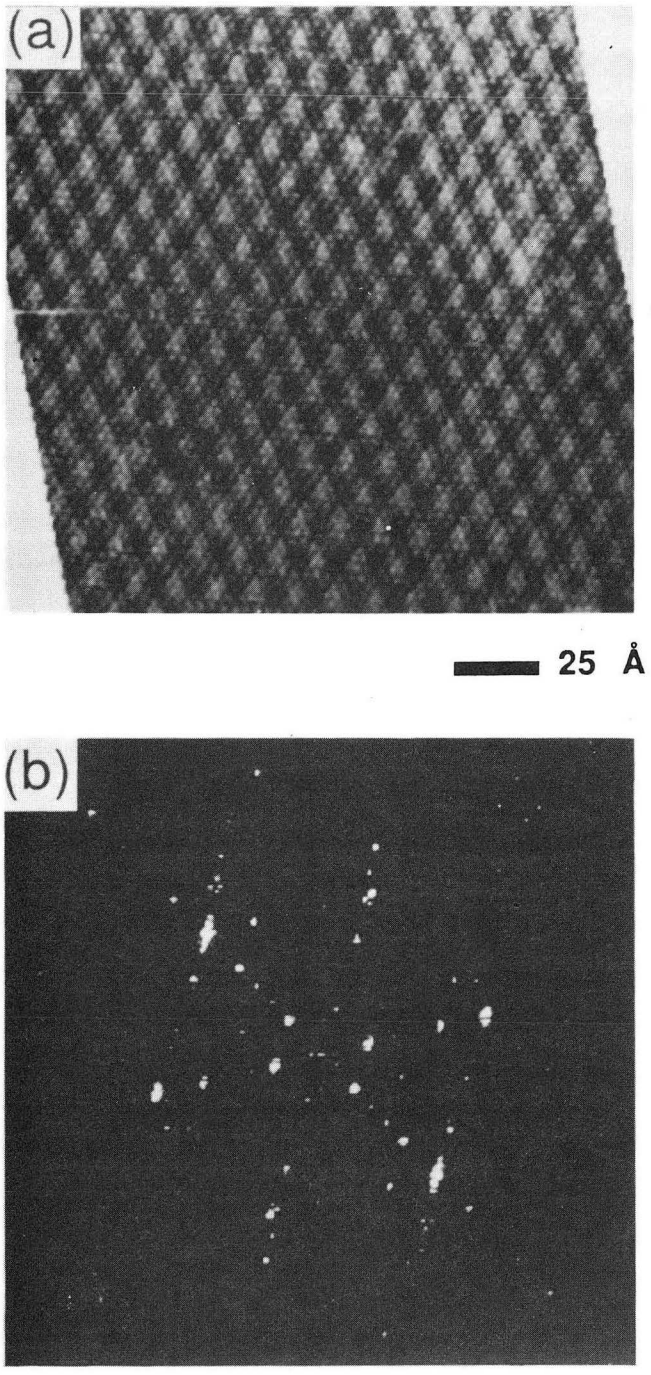


Figure 5-4 (a) Filtered STM image of 1T-$TaS_2$ taken at 360K in the I phase. (b) Fourier transform of (a). (XBB-910-8707)

discommensurate (see Chapter 6). However, these satellite peaks are in a significantly different orientation from those in the case of the discommensurate CDW in the **NC** phase. In the **NC** case, the satellite peaks do not appear on the line between the fundamental CDW peak and the origin of the FT, which is where they occur in this case. Further experiments, planned by my coworker Brian Burk, are needed to understand the significance and interpretation of the satellite spots in the **I** phase.

[1]R.Inada, Y.Onuki, and S.Tanuma, Physica B + C **99B**, 188 (1988); Phys. Lett. **69A**, 453 (1979).

[2]S.Noutomi, T.Futatsugi, M.Naito, and S.Tanaka, Solid State Commun. **50**, 181 (1984).

# Chapter VI

## **NC** phase

As 1T-$TaS_2$ is lowered in temperature from the **I** phase it undergoes a phase transition into the nearly commensurate (**NC**) phase at 354K. As was discussed in Chapter 3, in the **NC** phase the CDW is at an average angle which causes it to be incommensurate with the underlying atomic lattice. Using an x-ray diffraction study, Nakanishi and Shiba[1,2] proposed a discommensurate domain model for the **NC** phase that is illustrated in Fig. 3-5.

In 1988 the first STM study that considered the question of the existence of domains in 1T-$TaS_2$ was published.[3] This study found clear evidence for domains in the **T** phase but not in the **NC** phase. In a subsequent study, Gammie *et al.*[4] reported observing point discommensurations (DCs), in contrast with both the domain theory of Nakanishi and Shiba and the previous idea of a uniformly incommensurate CDW. Later, Wu and Lieber[5] observed a domain-like structure in real space STM images of the **NC** phase with amplitude and phase modulation in apparent agreement with the theoretical predictions. More recent STM and atomic force microscopy (AFM) results by Slough *et al.*[6] and Garnæs *et al.*[7] show evidence for an amplitude-modulated domain structure in the **NC** phase, but suggest that the CDW in this phase is uniformly incommensurate across most of the sample and thus does not exhibit discommensurations. Finally, Coleman *et al.*[8] used an argument based on the relative phases of the CDW maxima and the atomic lattice in the center of

the apparent domain structure to determine that the observed domains are true domains and not interference effects.

All of the previous STM studies employed only real space STM data in the search for discommensurate structures in the **NC** phase. In part (a) of this chapter I argue why real space data are insufficient for conclusively proving the existence of DCs and domains in this phase. Instead, it is necessary to examine the Fourier transform of the real space data for the telltale satellite spots that unequivocally prove the existence of a discommensurate structure. In part (b) I discuss our experimental STM results, making use of the Fourier transforms to uncover the details of the CDW superstructure in this phase.

(a) Discussion of Computer Simulations

To elucidate the subtleties of the interpretation of STM images of 1T-$TaS_2$ in the **NC** phase my coworker Brian Burk and I have generated computer simulations of the appearance of STM images in the presence and absence of domains and DCs. First we consider the case where there are no amplitude or phase modulations present in the simulated CDW. Figure 6-1(a) shows such an image. In the same way as was shown for the simulation discussed in chapter 4, we generated this image by superimposing three sine waves to represent the atomic lattice and three additional sine waves which produce the uniformly incommensurate CDW. The atomic lattice constant ($a_o$ = 3.346 Å) and the CDW wavevector ($\lambda_{CDW}$ = 11.74 Å) were chosen to agree with those in the **NC** phase at room temperature measured by x-ray diffraction[6]. The CDW was

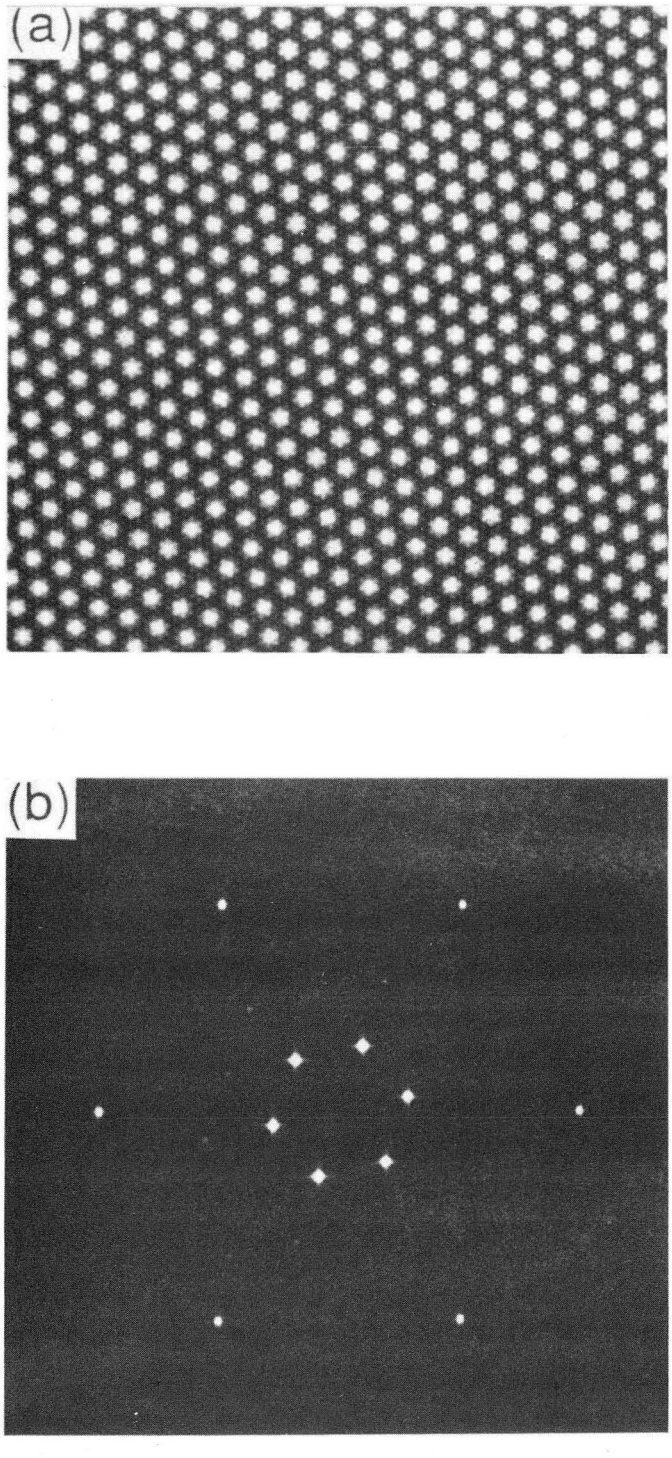


Figure 6-1 (a) Real space computer generated model of a uniformly incommensurate charge density wave with the average parameters known for the CDW in 1T-$TaS_2$ at room temperature from x-ray diffraction studies. (b) Fourier transform of (a). (XBB-910-8779A)

constructed to be at an angle of $\Phi$ =11.8° relative to the lattice, which is the average angle of $\Phi$ measured by x-ray diffraction[6]. The amplitude of the CDW sine waves were chosen to be three times the amplitude of the atomic lattice sine waves in agreement with the amplitude ratio suggested by real STM images.[9]

The method of construction of this image becomes more clear upon examination of the Fourier transform, shown in Fig. 6-1(b). This figure clearly shows that the only Fourier components in the image are at the fundamental frequencies of the CDW and the lattice. Nevertheless, upon modifying the gray scale in the real space image, we resolve apparent "domains", caused by the beating of these two sets of frequencies. Figure 6-2(a) is identical to Fig. 6-1(a) except that the cut-off level for the gray-scale on the computer screen has been adjusted to emphasize only the brightest points in the image. This procedure of modifying the computer gray scale to emphasize certain important properties of STM images has been routinely applied by many authors, including most of the published images purporting to demonstrate domains in 1T-$TaS_2$.

A close inspection of Fig. 6-2(a) will reveal that the CDW appears not only to exhibit amplitude domains, but the effect of the moiré pattern is also to produce apparent phase slips between the false "domains". The presence of apparent domains and phase slips is in spite of the fact that the image represents a uniformly incommensurate CDW with no inherent true amplitude or domain structure whatsoever. These false "domains" and apparent phase slips are due solely to interference (or beating) between the CDW and the underlying lattice that produces the moiré pattern.

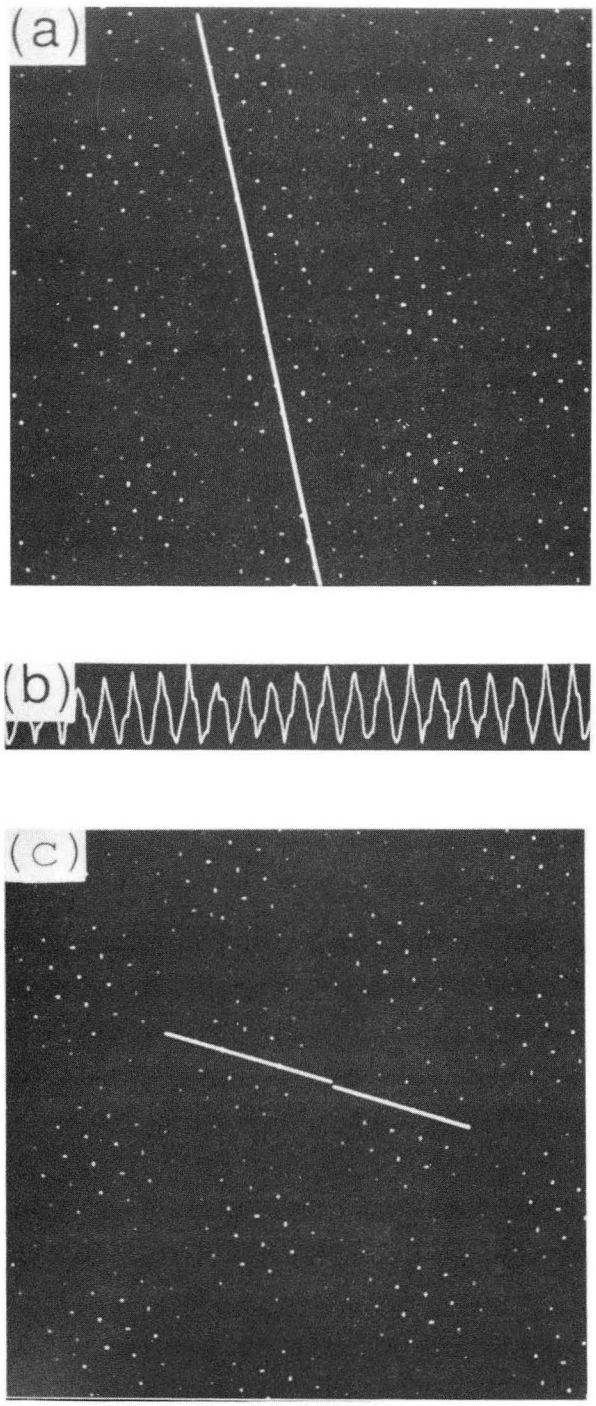


Figure 6-2 (a) Same model as was displayed in Fig. 6-1(a) except that the computer grayscale has been adjusted to emphasize the moiré pattern. (b) Single line through (a). (c) Same as (a) with two lines drawn on the model to illustrate the apparent phase slip.

(XBB-900-10069A)

Indeed, all of the characteristics of CDW amplitude and phase modulations that have been described in previous STM studies can be observed in the moiré pattern in Fig. 6-2(a). The apparent amplitude modulations can be observed without adjusting the computer gray-scale by displaying the CDW amplitude along a line of maxima, as shown in Fig. 6-2(b). The apparent phase modulation can be seen by sighting along a line of CDW maxima at a glancing angle. The maxima do not appear to be collinear; the interference of the two lattices create an apparent phase shift of one lattice constant between one "domain" and an adjacent one. This effect is emphasized by the lines drawn on Fig. 6-2(c) in two adjacent "domains". The size and orientation of the "domains" in the moiré pattern both agree with the values predicted by Nakanishi and Shiba's DC theory. This is in no way unexpected. These values are dictated by the values of the average CDW wavevectors known from x-ray diffraction studies and used in the calculation of the DC model. The moiré pattern even mimics the effect of causing the CDW to appear at the commensurate angle (13.9°) inside a single "domain" [this is determined by measuring the angle relative to the lattice of the lines in Fig 6-2(c)].

It is illuminating to contrast Figs. 6-1 and 6-2 with Fig. 6-3. Figure 6-3(a) is a computer simulation generated in the same way as Fig. 6-1 except that now the amplitude and phase modulations predicted by Nakanishi and Shiba have been added to the image. This added superstructure is most easily seen in Fig. 6-3(b), which is a Fourier transform of the real space image shown in Fig. 6-3(a). In this case, a set of satellite spots ring each fundamental CDW peak.

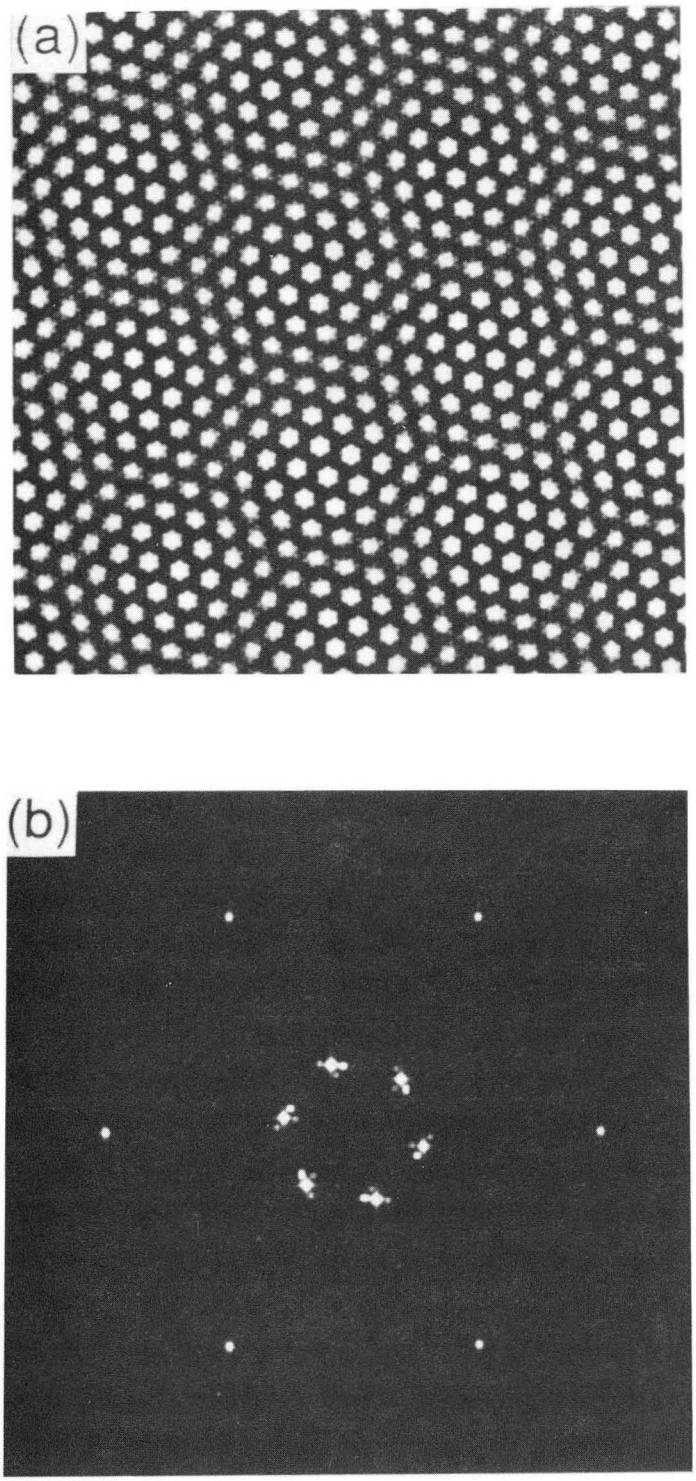


Figure 6-3 (a)Real space computer generated model of a discommensurate CDW with the parameters given by Nakanishi and Shiba in their proposed model for the configuration of the CDW in the **NC** phase of 1T-$TaS_2$. (b) Fourier transform of (a). (XBB-910-8778A)

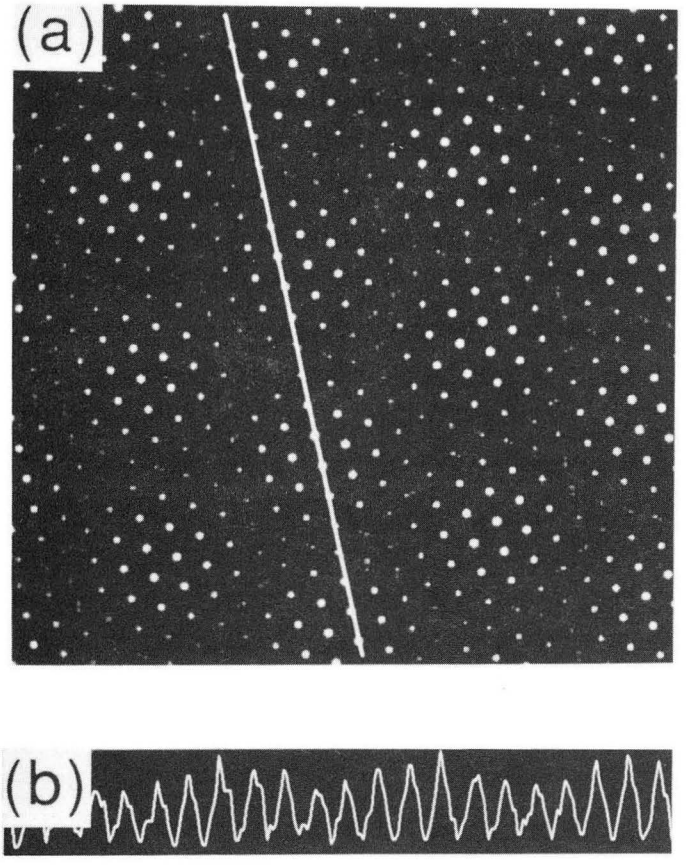


Figure 6-4 (a) Same model as was displayed in Fig. 6-3(a) except that the computer gray-scale has been adjusted to emphasize the moiré pattern. (b) Single line through (a). (XBB-910-8774A)

Such satellites are always present when the CDW exhibits domains and DCs. Figure 6-4(a) is the same as Fig. 6-3(a) except for an adjustment of the computer gray-scale, and Fig. 6-4(b) is a single line scan through the CDW maxima. By comparing Figs. 6-2(a) and 6-4(a), or Figs. 6-2(b) and 6-4(b), one sees that unequivocal determination of the presence of amplitude domains and DCs in the CDW in 1T-$TaS_2$ from real space STM images is extremely difficult. However, it is equally apparent from Figs. 6-1(b) and 6-3(b) that the Fourier transform of the real space image provides a method for reliable discrimination between the two cases.

The origin and significance of these satellite spots are easy to understand. In the case of a one-dimensional discommensurate CDW the wavefunction of the CDW can be written as[1]

$$\Psi_{CDW} = \Psi_{IC}(x) \cdot M(x) \qquad (6\text{-}1)$$

where $\Psi_{IC}(x)$ is the wavefunction for the uniformly incommensurate CDW and M(x) is a modulation envelope. This modulation envelope can be expressed as a Fourier series in the modulation wavevector $k_D$;

$$M(x) = \sum f_n \cdot e^{i(nk_Dx)}. \qquad (6\text{-}2)$$

Only the first two terms in this Fourier expansion are relevant since they are much larger than the higher order terms.[1] These are the n=0 and the n=1 terms. So we have

$$\Psi_{CDW} = f_0 \cdot \Psi_{IC}(x) + f_1 \cdot \Psi_{IC}(x) \cdot e^{i(k_D x)}. \quad (6\text{-}3)$$

Since

$$\Psi_{IC} = \Psi_o e^{i(k_{IC} x)}, \quad (6\text{-}4)$$

where $k_{IC}$ is the incommensurate wavevector, this formula produces terms in the Fourier expansion at $k_{IC}$ and at $k_{IC}+k_D$. Generalizing to the two-dimensional case, the term at $k_{IC}$ is the fundamental incommensurate peak seen in the Fourier transform and the terms at $k_{IC}+k_D$ are the satellite peaks which are the signature of the modulation, i.e. of the domain structure.

Previous STM studies have relied solely on real-space STM images to attempt to identify the presence or absence of CDW amplitude and phase modulations, and since the authors did not adequately account for the interference effect of the two lattices, the conclusions have been questionable. The tests used for the determination of the presence of domains have included; (1) looking for variations in the CDW amplitude (refs. 5, 6, and 7), (2) sighting along rows of CDW maxima in the real space image to look for phase slips (refs. 4 and 5), (3) measuring the local angle of the CDW relative to the lattice of the real space image and comparing it to the commensurate angle of 13.9° (refs. 3, 4, 5, and 7), (4) examining the fine structure of the real space images of the CDW to find areas where the CDW maxima or minima appear identical thus proving local commensurability (refs. 3 and 5), (5) examining the Fourier transform of the real space data for a spot at the commensurate

wavevector (ref. 7), and (6) examining the relative phase of the CDW maxima and the atomic lattice at the center of the apparent domains (ref. 8).

Of these tests, (1), (2) and (3) fail because the moiré pattern passes them so they do not prove the existence of domains. In addition tests (3), as well as test (4), are faulty because they only test for a fully "locked-in" domain structure. It is interesting to note that different groups have reached opposite conclusions about the real space images using these second two tests.[10] Test (5) fails because a spot at the commensurate wavevector is not expected even in the domain model. Finally, test (6) fails because of the multiple tip affect described in Chapter 4. This effect causes the apparent phase of the CDW relative to the atomic lattice to vary randomly, rendering the measurement of this phase meaningless. Thus it is clear that, to date, no one has examined STM data adequately to determine the presence or absence of domains in 1T-$TaS_2$.

One last aspect of the search for satellite spots in the Fourier transforms of real STM data needs to be mentioned before I go on to a discussion of the STM data. That is, that if I perform a Fourier transform (FT) of the raw data such as that in Fig. 6-5(a), (a computer simulation of a CDW exhibiting domains), it is clear that any satellite spots that might be present are difficult to detect because of the bright streaks caused by the edges of the image [Fig. 6-5(b)]. In order to remove these streaks and obtain the cleanest possible FT, it is necessary to apodize the STM image to remove the effects of the image edges in the FT. To do this, the real space data

are multiplied by a window function, cos $\alpha$. Since our images are 256 x 256 pixels, we used a window

$$f = [\cos \pi \cdot (x-128)/256 - 1] \cdot [\cos \pi \cdot (y-128)/256 - 1], \qquad (6\text{-}5)$$

where x and y are the pixel indices in the data array. Figure 6-5(c) shows the result of this filter on the real space image while Fig. 6-5(d) is a FT of the apodized image. In this figure the satellite spots around the CDW peaks are clearly visible. For this reason, all of STM data presented in this thesis were apodized before being Fourier transformed.

(b) Discussion of Experimental Data

In the **NC** phase, especially at higher temperatures, the domains are hexagonal in shape and only a few CDW wavelengths across, reducing the number of CDW maxima or minima to compare for a high degree of similarity [test (4) from above] to about seven. This can clearly be seen in Fig. 6-6(a), an STM image of 1T-$TaS_2$ taken at 343K. The very small size of the domains at this temperature also makes the determination of the angle of the CDW inside the domains very inaccurate [test (3) from above]. In Fig. 6-6(a) an apparent amplitude modulation is present, but as was discussed in part (a), this could be due to a moiré pattern.

As was shown earlier, the presence or absence of satellite spots in the Fourier transform is the key to solving this problem. Figure 6-6(b) is a Fourier transform of Fig. 6-6(a). The satellite spots around the fundamental CDW peaks (as well as around the

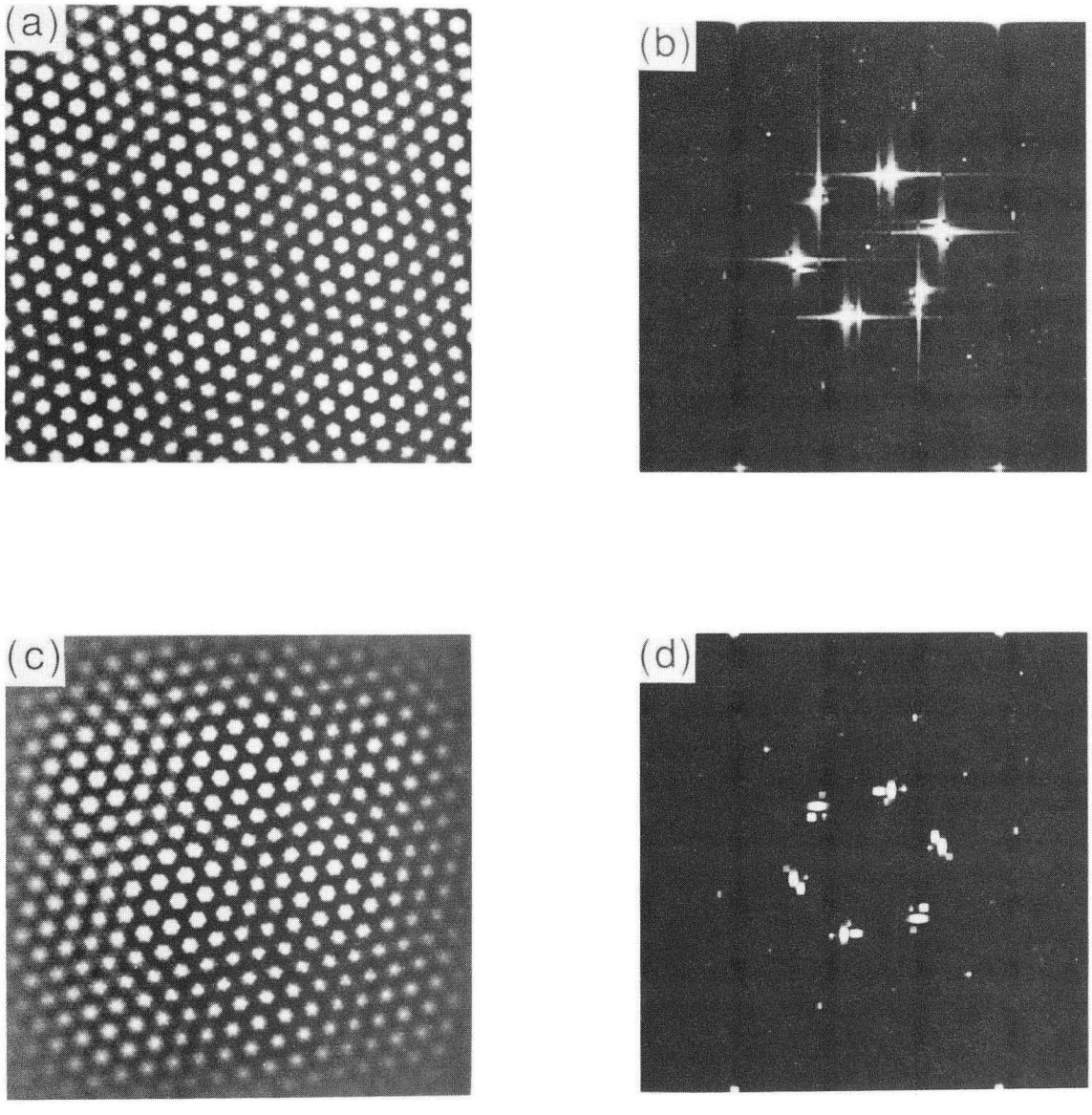


Figure 6-5 (a) Computer simulation of CDW exhibiting domains. (b) Fourier transform of (a). (c) Apodized image of (a). (d) Fourier transform of (c). (XBB-910-7940B)

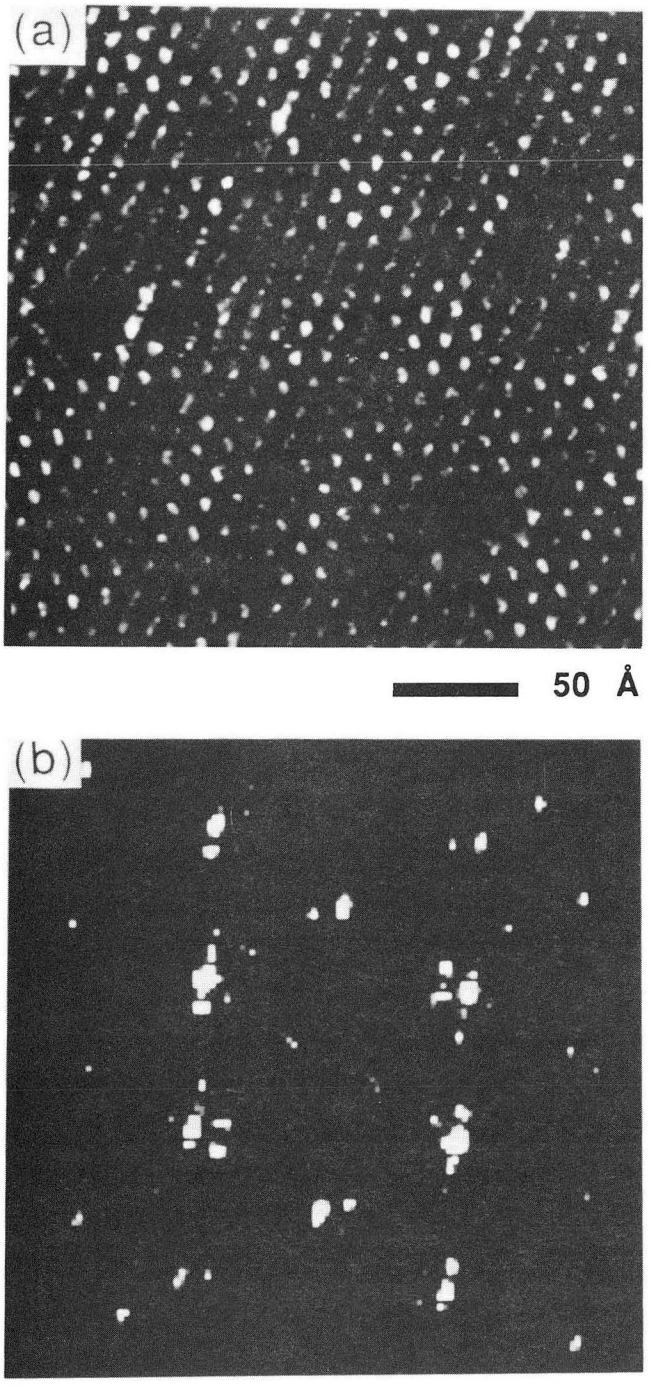


Figure 6-6 (a) Apodized real space STM data of 1T-$TaS_2$ acquired at 343K. (b) Fourier transform of (a). (XBB-916-4623A)

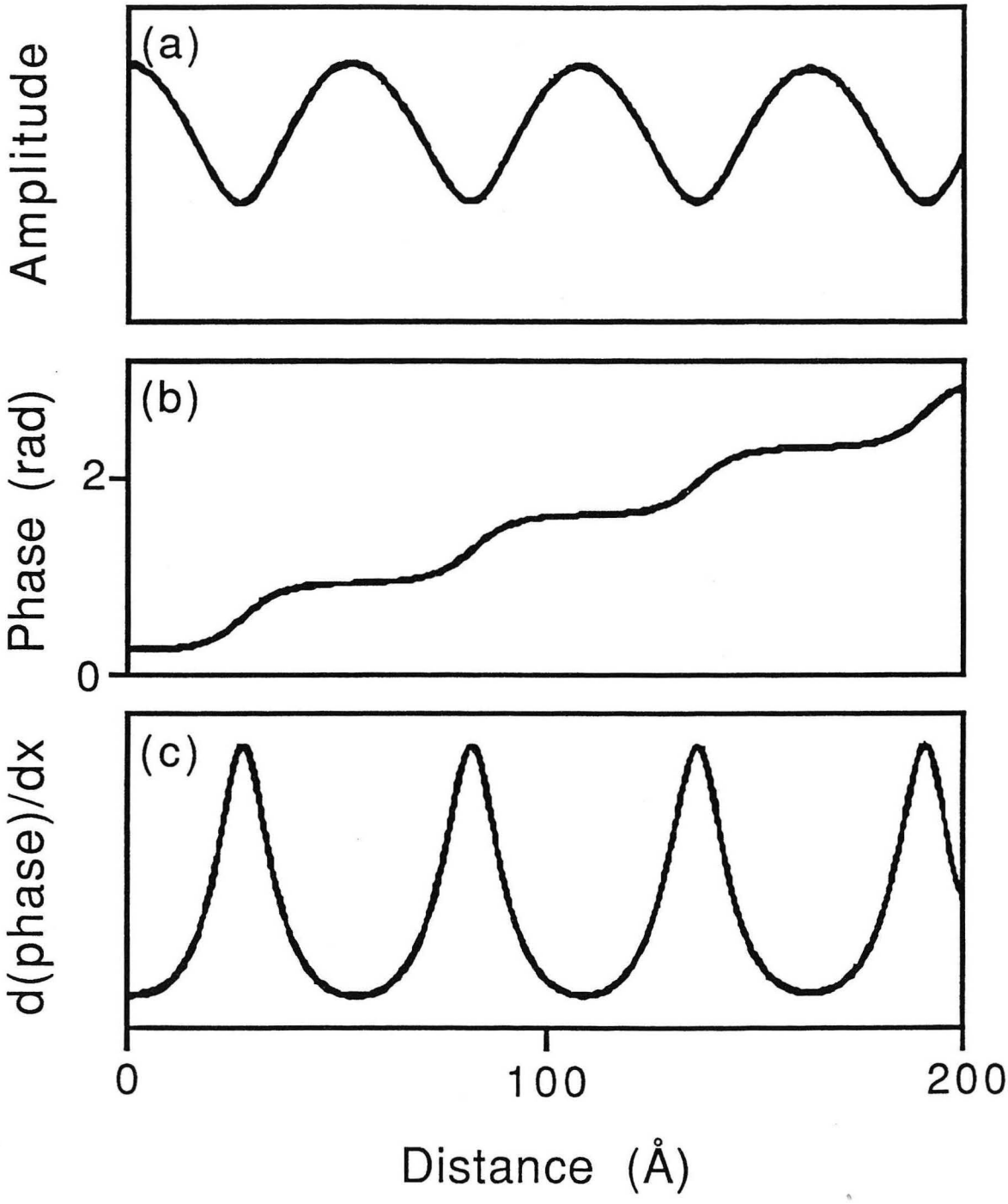


Figure 6-7 Graphs generated by an analysis of the satellite spots in Fig. 6-6(b). (a) CDW phase vs. distance, (b) CDW amplitude vs. distance, (c) derivative of the CDW phase vs. distance.

higher order peaks) are clearly visible in this image. Figures 6-7(a), 6-7(b) and 6-7 (c) are graphs of the CDW phase, amplitude and the derivative of the CDW phase determined from the satellite spots position and intensity in Fig. 6-6(b).

Figures 6-8 through 6-15 are similar to Fig. 6-6 and 6-7 except that the data were taken at different temperatures. Figures 6-8 and 6-9 are of data acquired at room temperature (295 K), Figs. 6-10 and 6-11 data acquired using a bath of ice water (273 K), Figs. 6-12 and 6-13 data acquired at 225K and Figs. 6-14 and 6-15 data acquired using an ice bath of octane (215 K). In each case, the (a) part of the first figure is of the apodized STM data and the (b) part of the first figure is the Fourier transform. Likewise, the graphs in the second figures are constructed by the measurement of the satellite spots off of the FT in the first figure.

These figures clearly prove that the CDW in 1T-$TaS_2$ in the **NC** phase is arranged into domains separated by diffuse DCs as predicted by Nakanishi and Shiba at all temperatures within the **NC** phase. Satellite spots are easily discernible in each of the Fourier transforms, unequivocally proving the existence of a discommensurate structure as was explained in part (a) of this chapter. In addition, the graphs constructed from the FTs at each temperature clearly show areas where the CDW phase is constant (i.e. the CDW is commensurate) and the CDW amplitude is enhanced, separated by regions of decreased CDW amplitude and rapidly changing phase (the discommensurations).

Using the graphs of the derivative of the CDW amplitude vs. distance we have extracted the domain periodicity for each

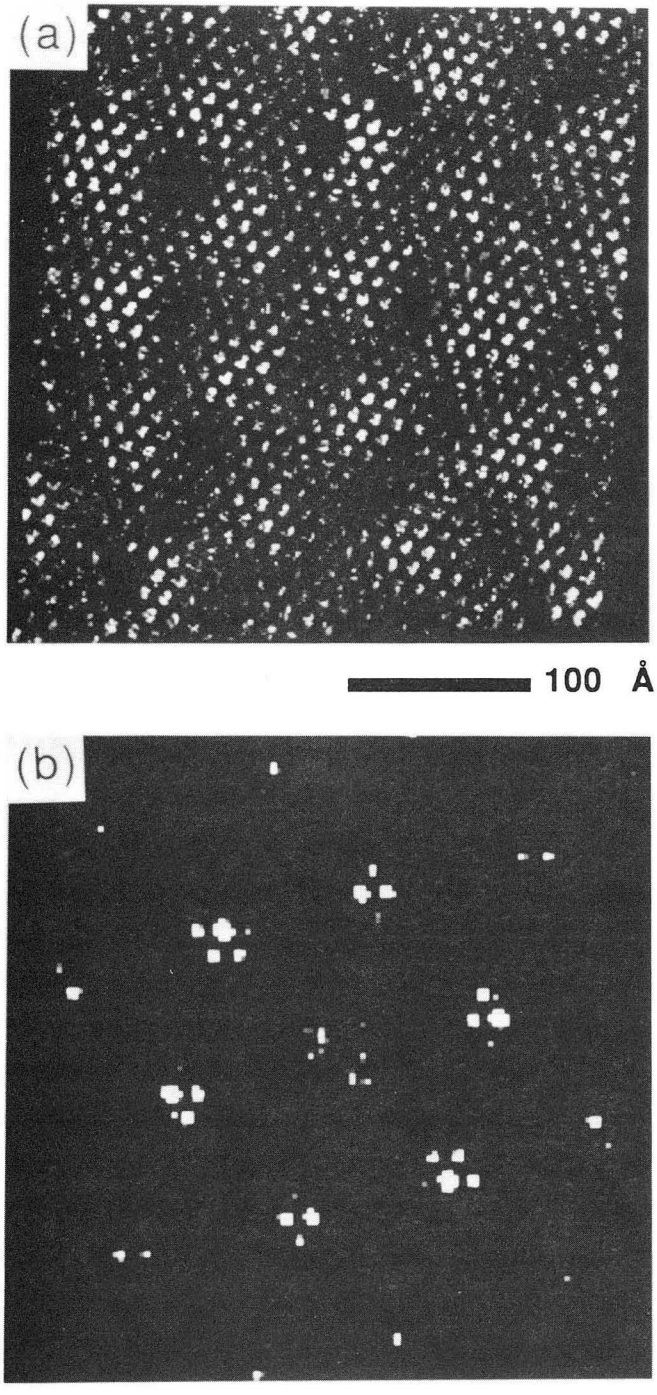


Figure 6-8 (a) Apodized real space STM data of 1T-$TaS_2$ acquired at 295K. (b) Fourier transform of (a). (XBB-915-3953A)

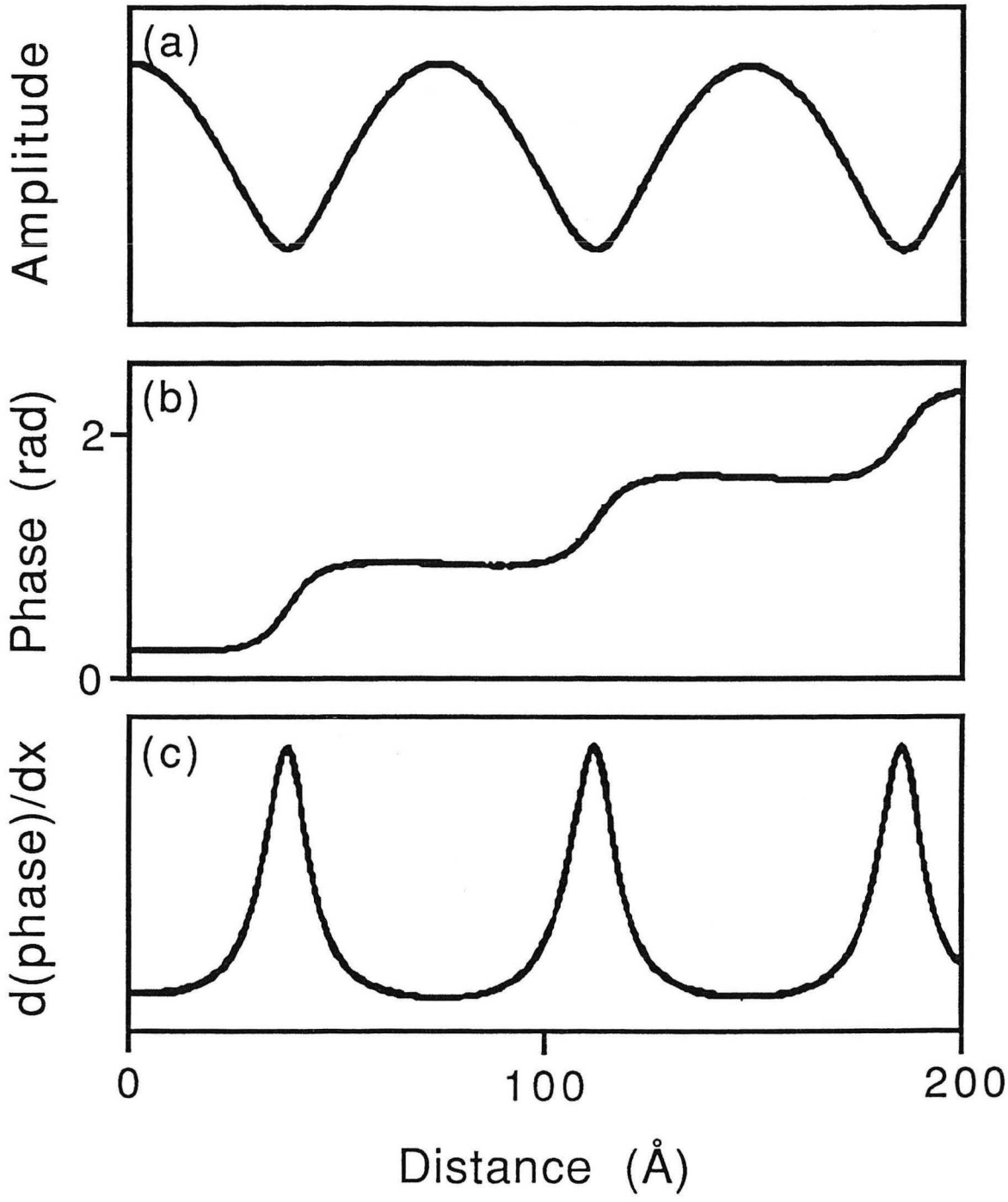


Figure 6-9 Graphs generated by an analysis of the satellite spots in Fig. 6-8(b). (a) CDW phase vs. distance, (b) CDW amplitude vs. distance, (c) derivative of the CDW phase vs. distance.

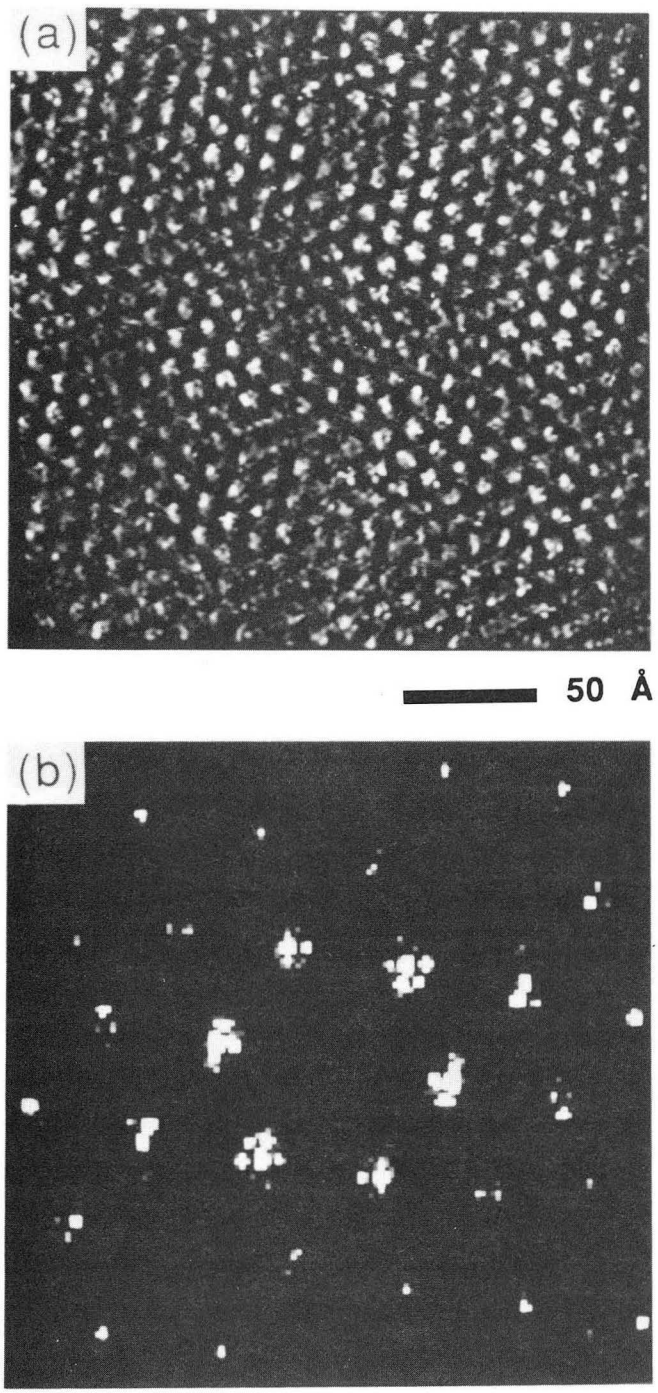


Figure 6-10 (a) Apodized real space STM data of 1T-$TaS_2$ acquired at 273K. (b) Fourier transform of (a). (XBB-915-3950A)

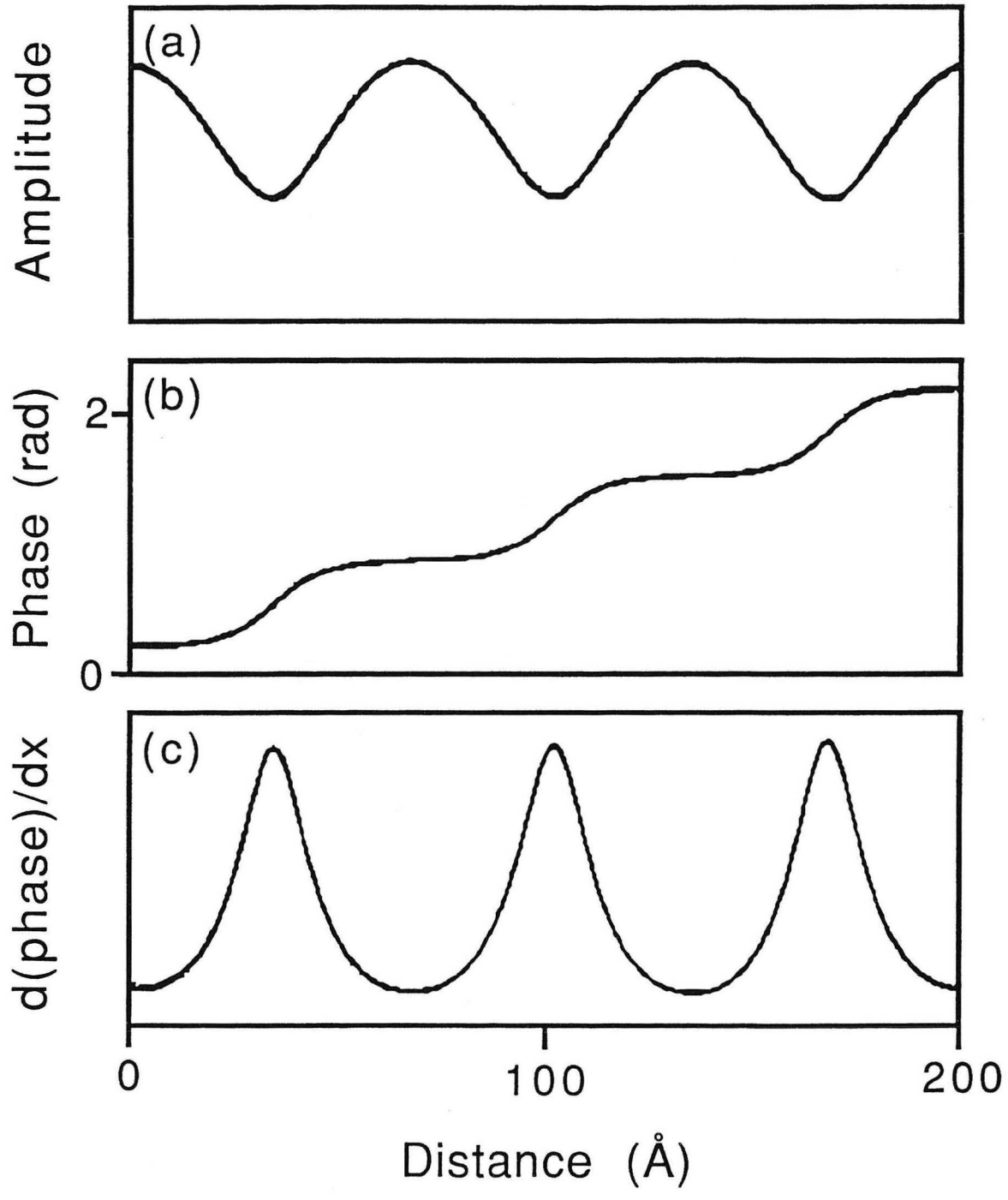


Figure 6-11 Graphs generated by an analysis of the satellite spots in Fig. 6-10(b). (a) CDW phase vs. distance, (b) CDW amplitude vs. distance, (c) derivative of the CDW phase vs. distance.

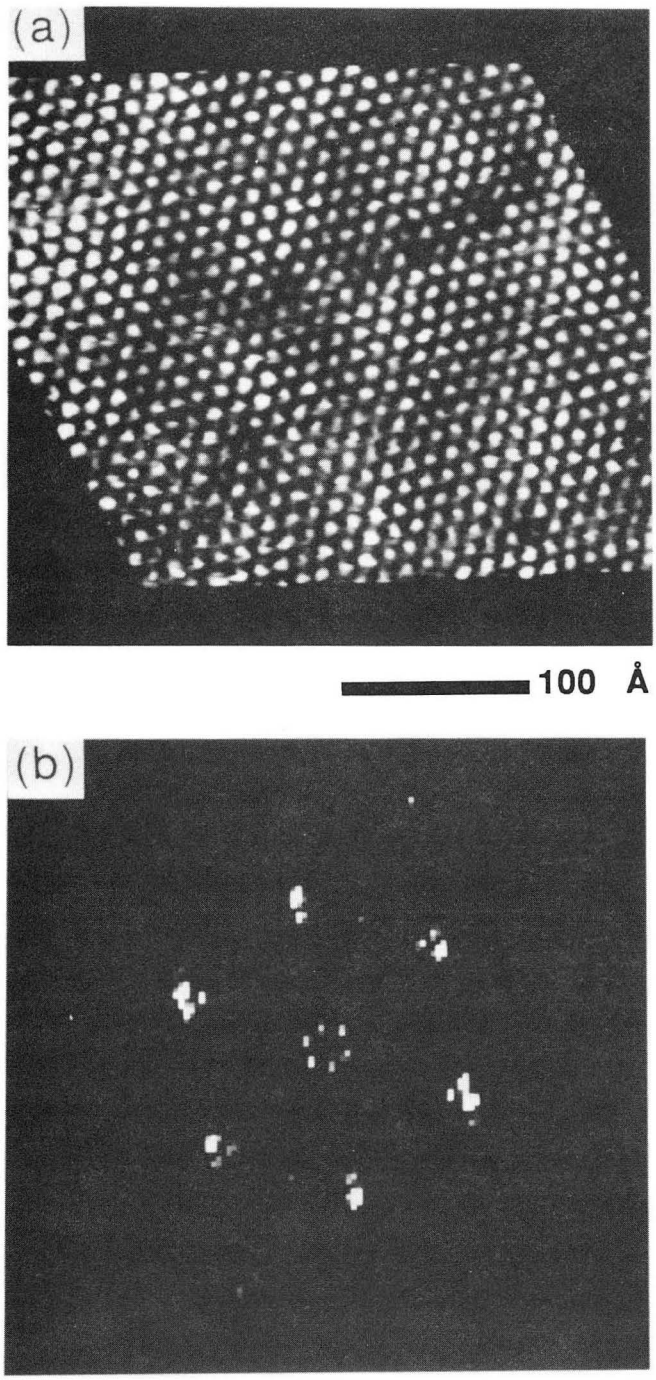


Figure 6-12 (a) Apodized real space STM data of 1T-$TaS_2$ acquired at 225K. (b) Fourier transform of(a). (XBB-915-3947A)

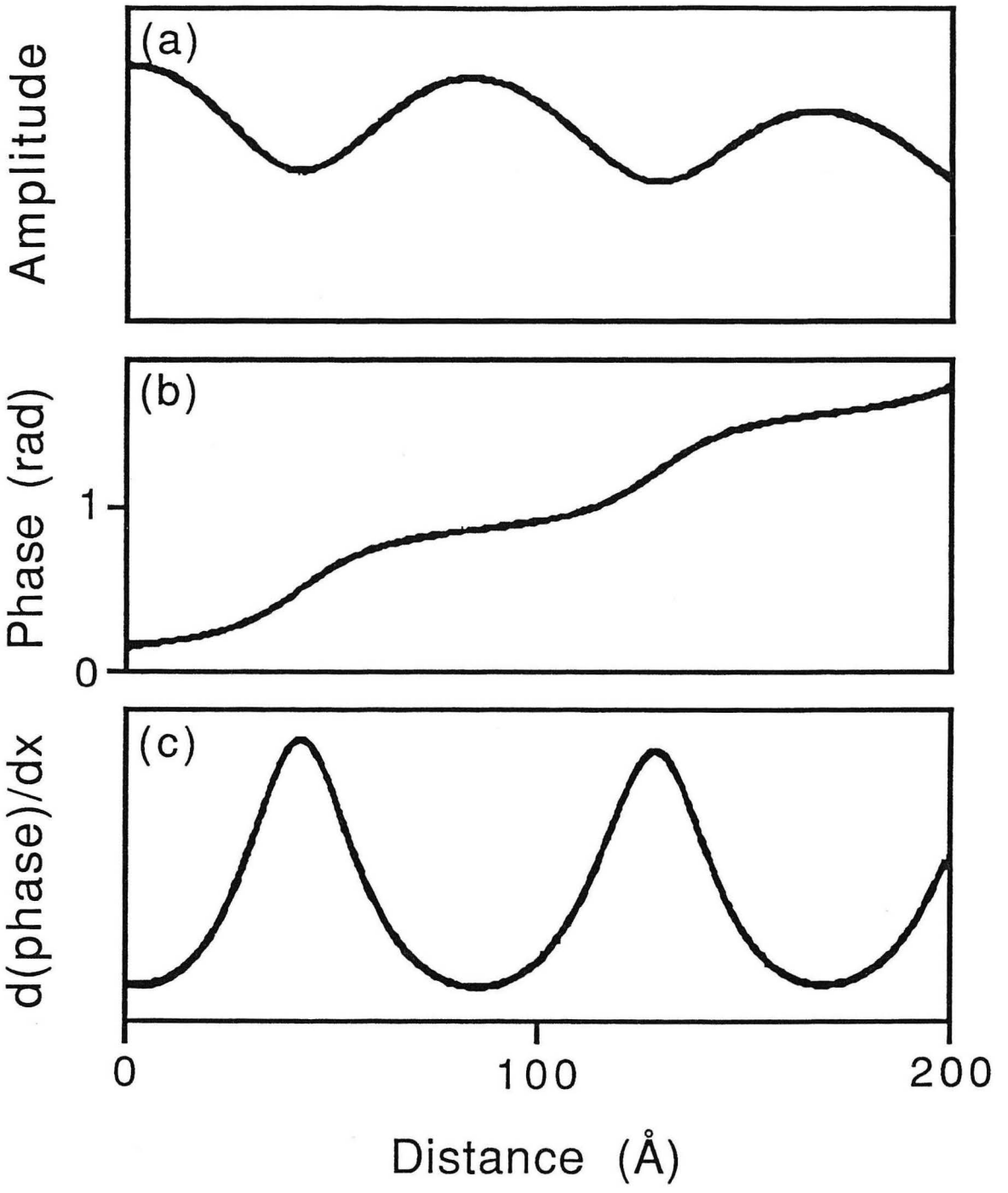


Figure 6-13 Graphs generated by an analysis of the satellite spots in Fig. 6-12(b). (a) CDW phase vs. distance, (b) CDW amplitude vs. distance, (c) derivative of the CDW phase vs. distance.

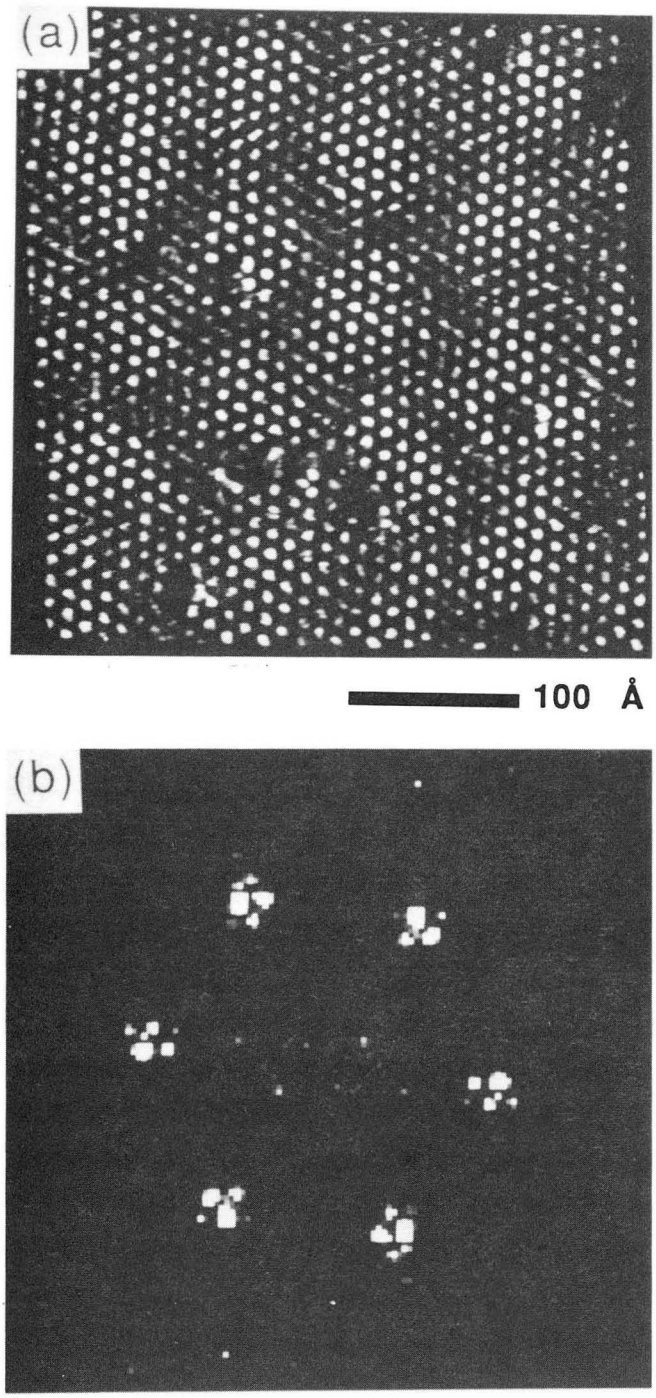


Figure 6-14 (a) Apodized real space STM data of 1T-$TaS_2$ acquired at 215K. (b) Fourier transform of (a). (XBB-915-3954A)

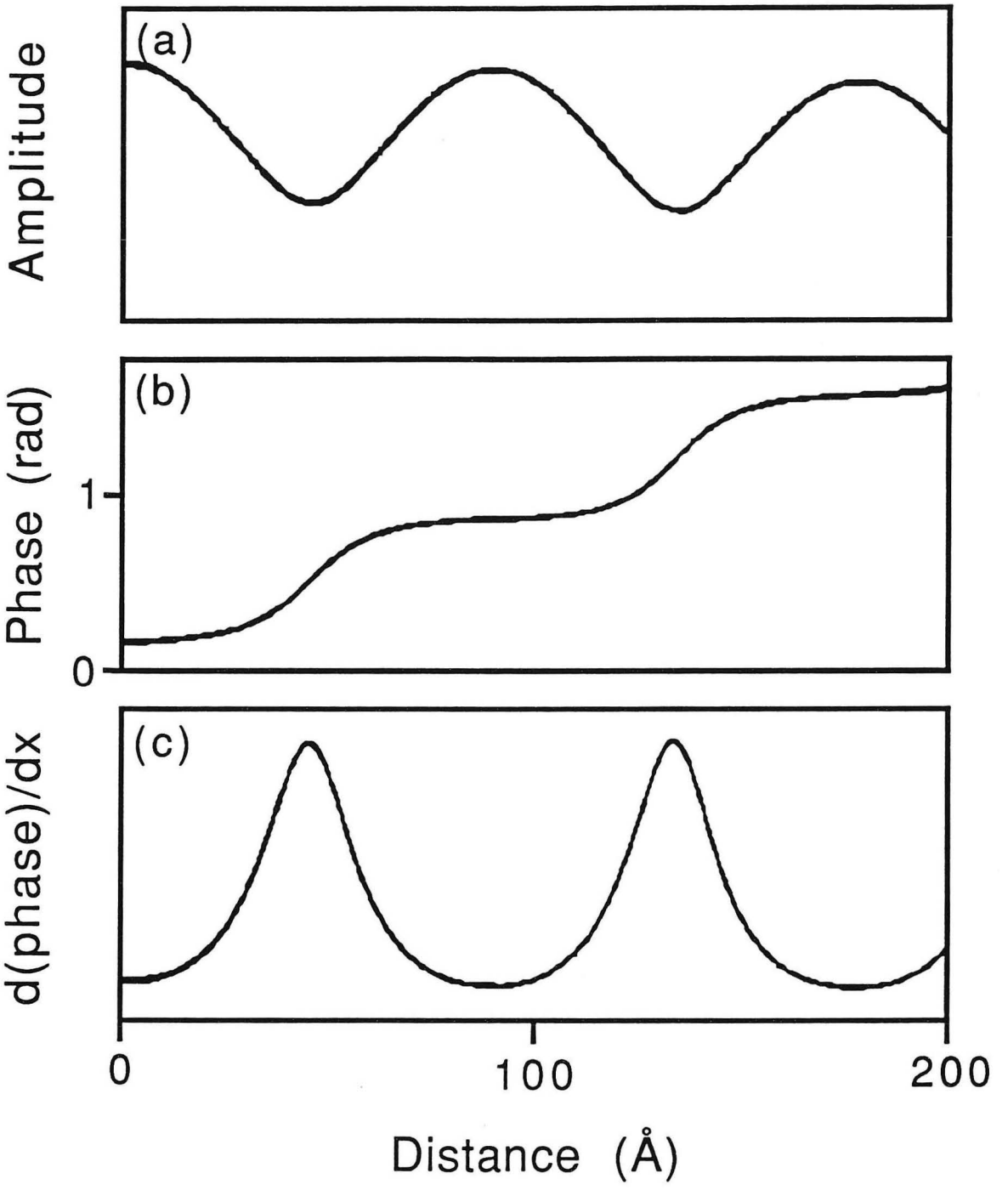


Figure 6-15 Graphs generated by an analysis of the satellite spots in Fig. 6-14(b). (a) CDW phase vs. distance, (b) CDW amplitude vs. distance, (c) derivative of the CDW phase vs. distance.

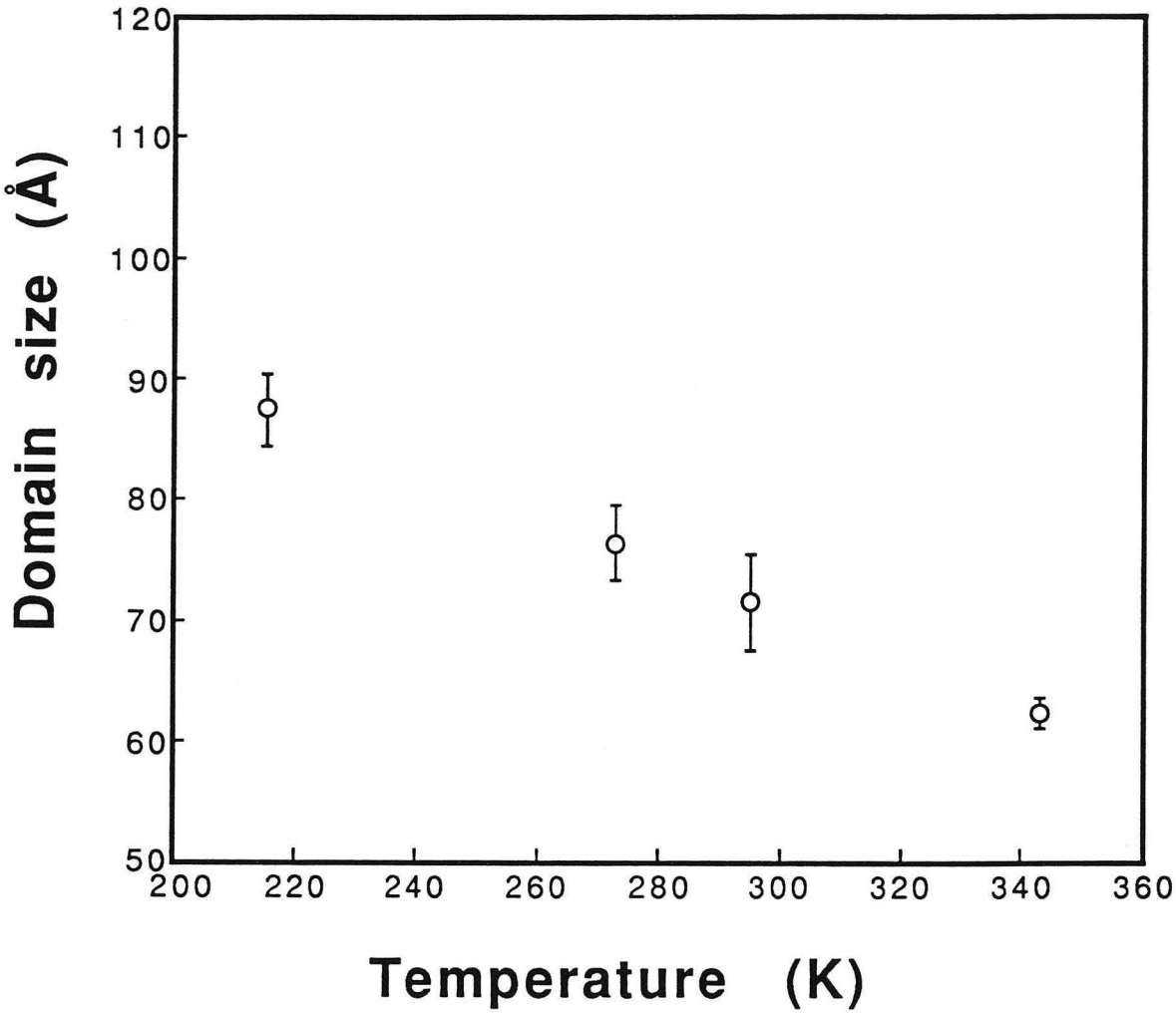


Figure 6-16 Domain period versus temperature for our STM data of 1T-$TaS_2$ in the **NC** phase. The error bars are at $\pm\sigma$.

temperature (averaging over at least 5 images at each temperature). (The data at 225K were not included in this and the following figures because we had too few high-quality images.) Figure 6-16 is a graph of the domain period vs. temperature for our data. It is interesting to note that, within experimental error, the domain period increases linearly with decreasing temperature.

In addition, we have measured the locations of the fundamental CDW wavevectors directly off of the Fourier transforms. A comparison of our measurements (again averaged over at least 5 images at each temperature) of the CDW angle relative to the lattice with the measurements of Wu and Lieber[5] (measured from real space STM data) and Scruby *et al.*[11] and Yamada *et al.*[12] (both x-ray diffraction studies) is shown in Fig. 6-17. One interesting fact to note about Fig. 6-17 is that, if the linear trend that we observe down to 215K continues down to the transition temperature T=180K, the CDW angle $\Phi$ will not make a smooth continuous transition to the commensurate angle of 13.9° at the transition temperature.

Assuming that the domain periodicity occurs at the lattice and CDW beating frequency, a simple relation between the domain periodicity, the CDW angle and the CDW wavelength is given by Eq. 6-6.

$$\text{Domain Periodicity} = \frac{a_o}{\sqrt{(\delta\Phi)^2 + (\delta\lambda/\lambda)^2}}, \qquad (6\text{-}6)$$

where $\delta\Phi$ is the difference between $\Phi$ and $\Phi_{commensurate}$ = 13.9° and is given in radians, and $\delta\lambda$ is the difference between $\lambda$ and

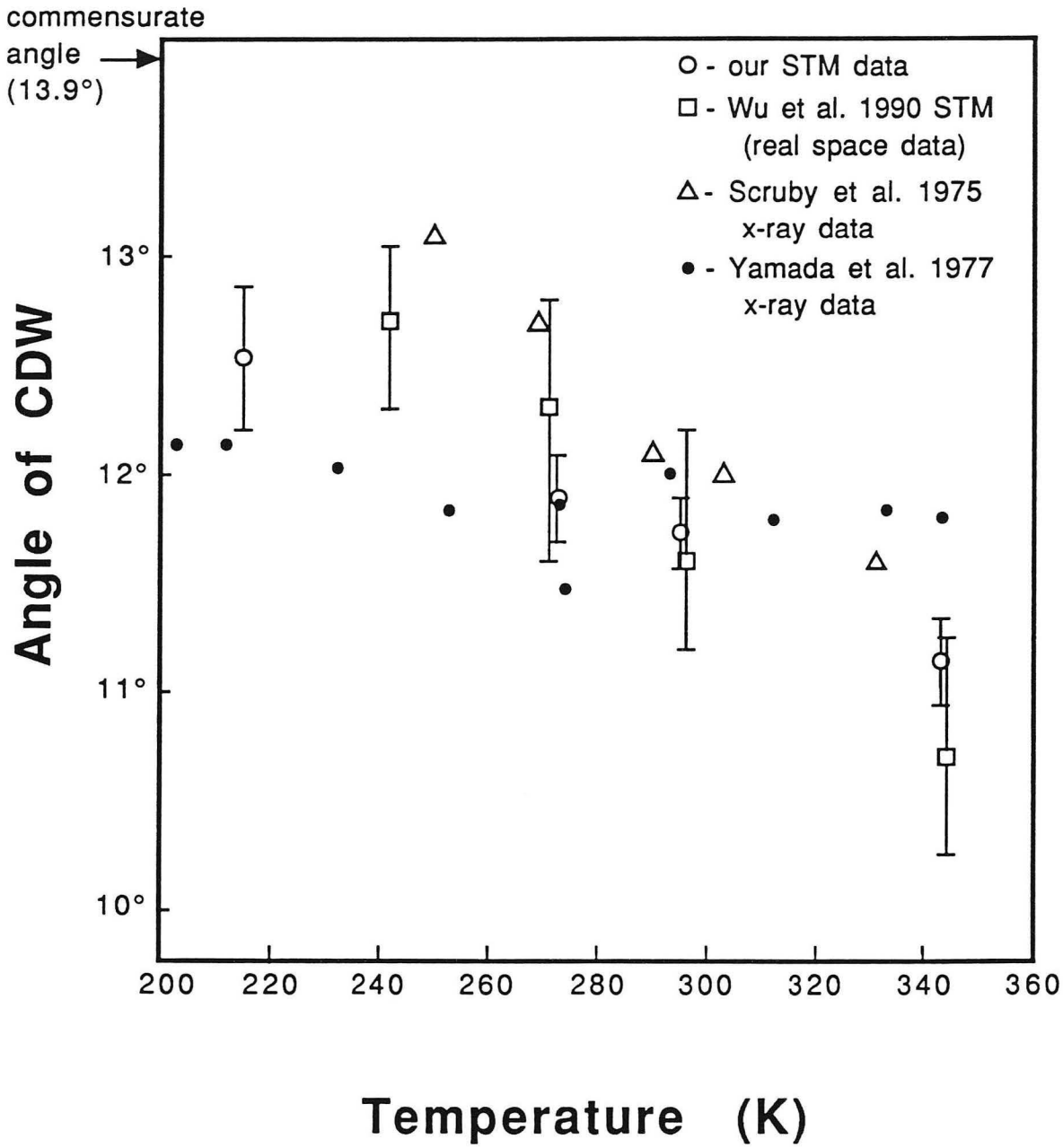


Figure 6-17 Plot of our measurement of the angle of the CDW relative to the lattice as a function of temperature in the **NC** phase of 1T-$TaS_2$ compared with previously published measurements. The error bars are at $\pm\sigma$.

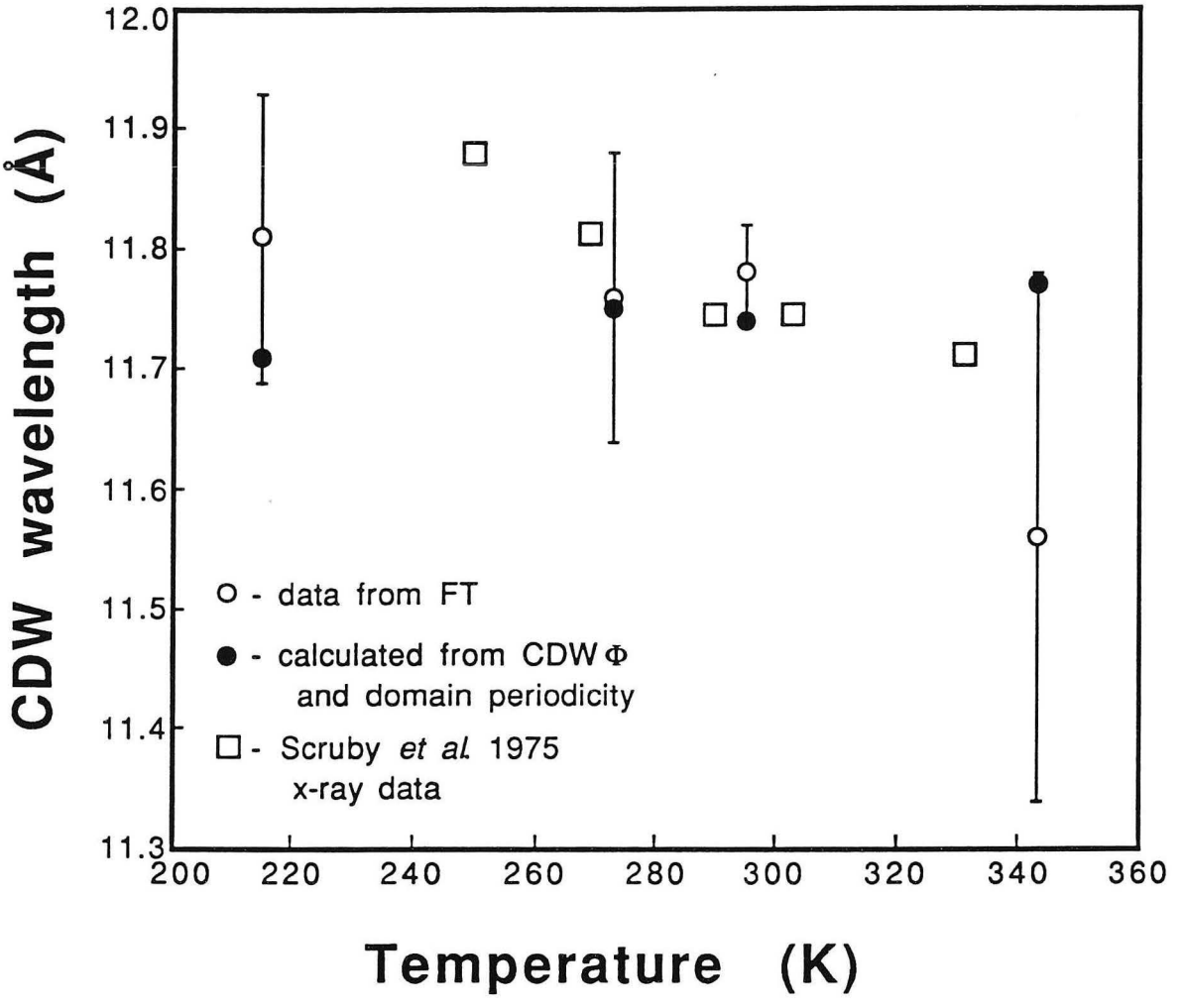


Figure 6-18 Plot of the wavelength of the CDW in the **NC** phase of 1T-$TaS_2$ measured directly from the FT, and calculated from the measured CDW angle and the domain periodicity. The error bars are at $\pm\sigma$. Also plotted are the results of an x-ray diffraction study by Scruby *et al.*[11]

$\lambda_{commensurate}$ = 12.06Å. We can check the consistency of our results by comparing the CDW wavelength obtained from direct measurements off of the FT and that calculated from Eq. (6-6). This comparison is plotted in Fig. 6-18. It is clear that the differences between the wavelengths obtained by these two methods agree to within our experimental error as well as agreeing with those measured by x-ray diffraction.[11] It is interesting to note that to within our experimental error the CDW wavelength does not appear to vary with temperature and has an average value of 11.73Å.

By combining both Figs. 6-16 and 6-17 we discover a subtle but interesting point about the nature of the DCs present in these images. To understand this point, however, it is first necessary to discuss the two possible configurations for a CDW DC: the DC which "compresses" the CDW wavelength and the DC which "expands" the CDW wavelength.

When the CDW undergoes a DC, it is required to slip one atomic lattice unit. However, the exact direction of this slip is not necessarily pre-determined. Figure 6-19(a) is a schematic illustrating the two most likely choices for the direction of the slip. At the phase slip, the CDW maximum which would have coincided with the atomic position labelled 0 if it had continued in a commensurate manner, will slip to either the atomic position labelled 1 or that labelled 2. If it goes to position 1, the CDW wavelength is "compressed" compared to the commensurate wavelength, whereas if it slips to position 2 the CDW wavelength becomes "expanded" compared to the commensurate wavelength.

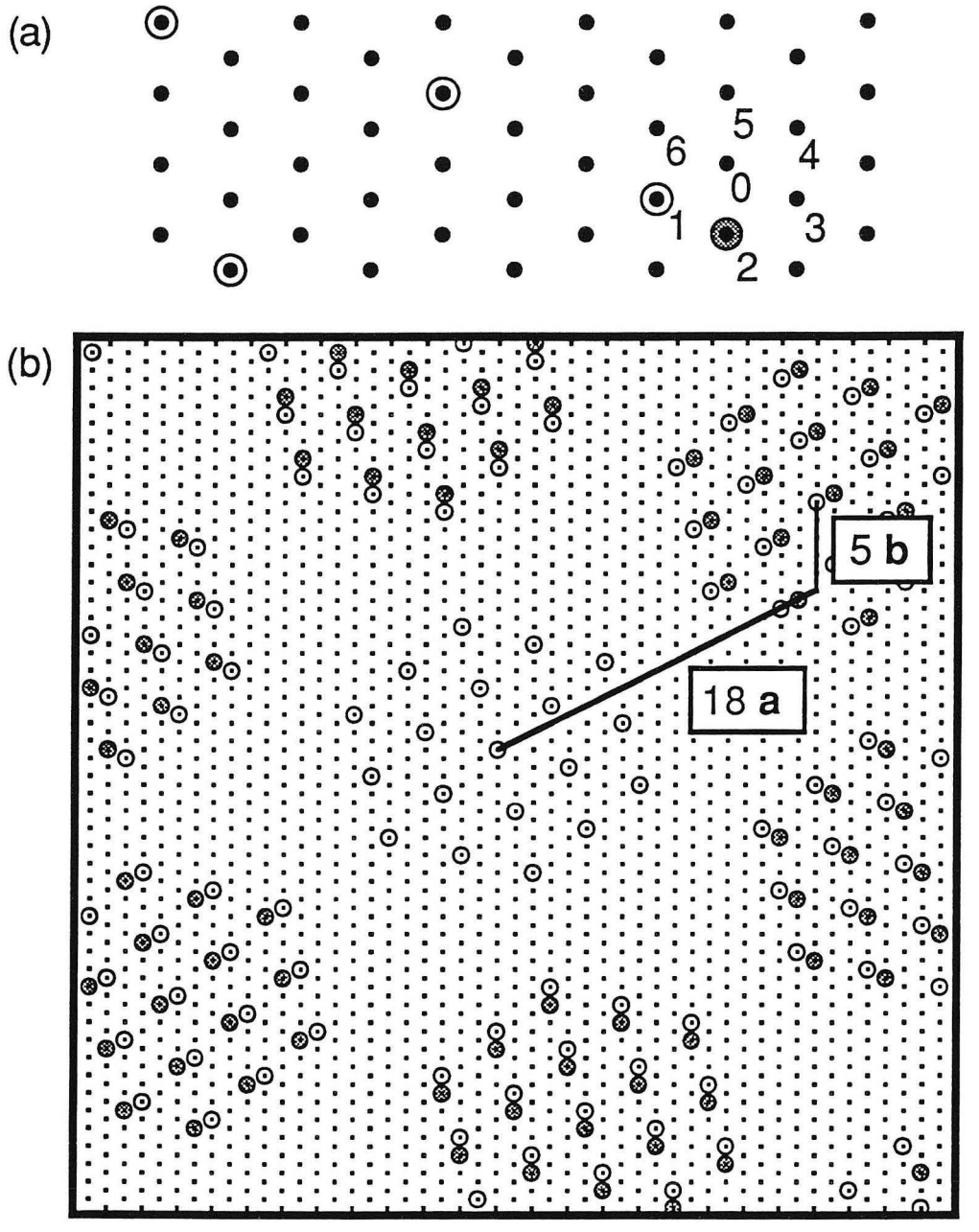


Figure 6-14 (a) Schematic illustrating the possible types of DC. If the CDW maximum slips to atomic position 1, a DC which "compresses" the CDW results. If the CDW maximum slips to atomic position 2, a DC which "expands" the CDW results. (b) Schematic illustrating the 18-5 structure of "compressed" DCs (open circles) and the 19-5 structure of "expanded" DCs (gray circles).

Both choices cause the CDW angle, relative to the atomic lattice, measured over several domains, to be less than the 13.9° commensurate angle, but the different angles resulting from each choice vary slightly. In their analysis of real space STM data, Wu and Leiber concluded that the majority of the DCs they observed were of the "compressed" type.[5]

If all of the DCs of the CDW are of the "compressed" type, one possibility for the **NC** phase at room temperature is the 18-5 structure, which is technically commensurate with a repeat spacing of 18 lattice units in the **a** direction and 5 in the **b** direction. This is the structure that was shown in Fig. 3-5 and is redrawn in Fig. 6-19(b) using the open circles. The similar 19-5 structure employs the "expanded" DCs and produces a slightly different CDW angle and domain periodicity. This structure is also shown in Fig. 6-19(b) using the gray circles There exist two whole families of discommensurate structures, one related to the 18-5 and using "compressed" DCs and one related to the 19-5 and using "expanded" DCs. Within one family, the different members differ from each other only by how many commensurate CDW wavelengths are contained within each domain. These two families are plotted in Fig. 6-20, along with our measurements of the actual CDW angle and wavelength that were plotted in Figs. 6-16 and 6-17.

Examination of Fig. 6-20 reveals that the actual discommensurate CDW structure employs both types of DCs. Each point plotted in the figure is taken from our data at a different temperature. The highest temperature point (that with the smallest domain periodicity) appears to lie closer to the family of "expanded"

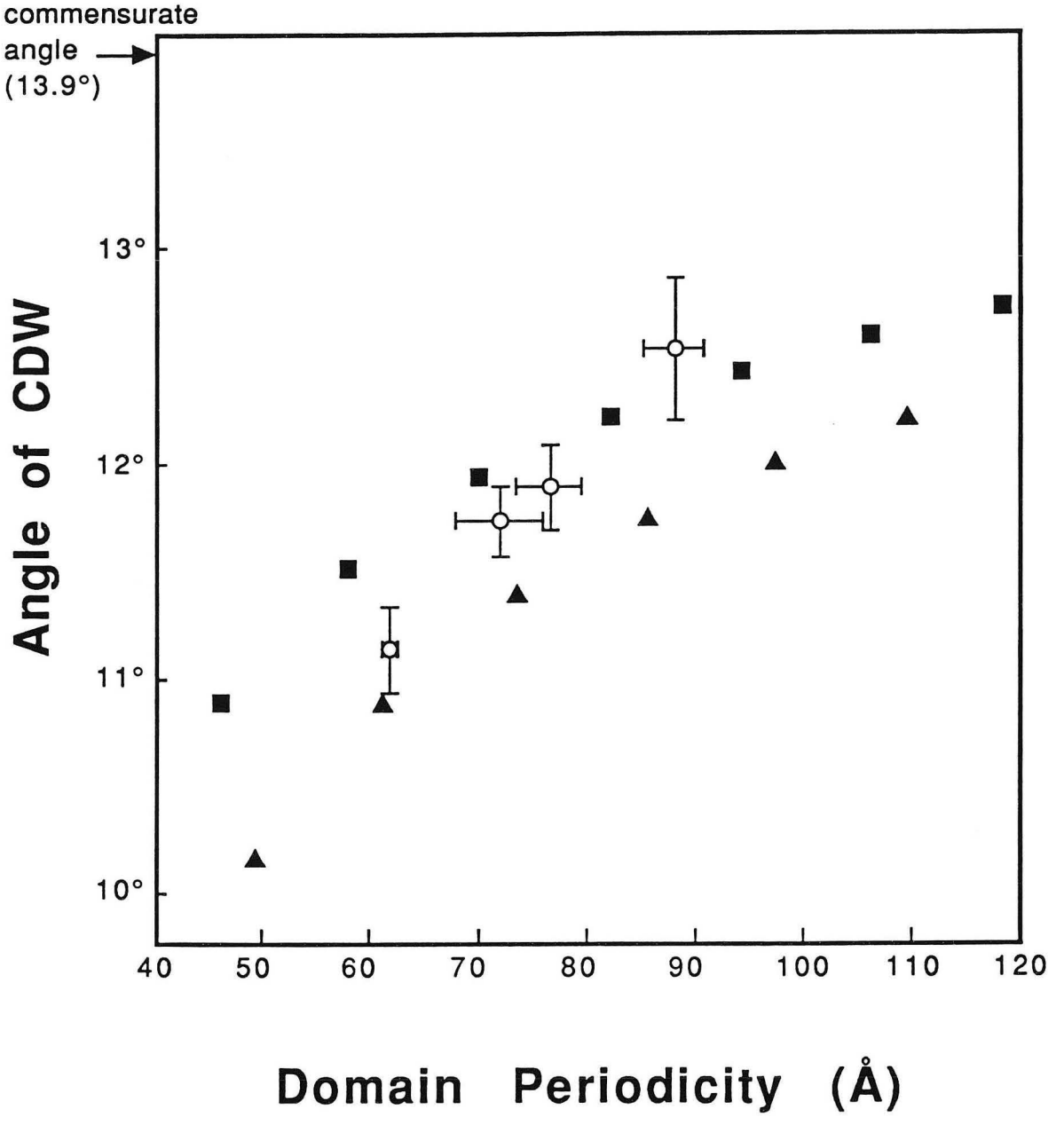


Figure 6-20 Plot of the angle of the CDW relative to the lattice (determined by the positions of the fundamental CDW peaks in the Fourier transforms of the STM images) vs. the domain periodicity (determined from the positions of the satellite spots in the Fourier transforms). The error bars are at $\pm\sigma$.

wavelength structures, while the other points lie closer to the "compressed" wavelength structures. The fact that the lowest temperature point (that with the largest domain periodicity) lies above the line connecting the "compressed" wavelength structures is not particularly disturbing. There are several other possible DCs, including one in which the CDW shown in Fig. 6-19(a) would slip to the atomic lattice position labelled 3. (This choice would result in a structure with an angle much closer to the commensurate angle of 13.9° at the same domain periodicity when compared to the other two families described.) A combination of different types of DCs between different domains would produce an intermediate structure with angle and domain periodicity values similar to those we measure.

The last question to consider in the analysis of the domain structure in the **NC** phase is the orientation of the domains. J.A.Wilson[13] has published an exhaustive theoretical study analyzing previous STM and x-ray diffraction data to determine the precise superstructure of the CDW in the **NC** phase. He concludes that the CDW is arranged in a $19\,^{2}/_{3}$ - by - $2\,^{2}/_{3}$ rotated honeycomb array which is closely related to the 18-5 array shown in Fig. 6-19(b). The differences between these two superstructures which are relevant to STM images are the orientation of the domains relative to the CDW and the precise value of the CDW wavelength and orientation, which are given in Table 6-1 along with the values we measure for these properties from our STM images at 295K. It is clear that our STM data agrees well with the $19\,^{2}/_{3}$ - by - $2\,^{2}/_{3}$ structure proposed by Wilson.

However, I believe it is a mistake to adhere too strongly to the idea that the CDW exists in a well-defined superstructure of a certain type. The CDW domains observed by the STM appear to quite nonuniform [see Figs. 6-6(a), 6-8(a), 6-10(a), 6-12(a) and 6-14(a)], with some domains appearing to be of unusual sizes or off-center relative to the other domains in a single image. In addition, the CDW domain structure appears to change more or less continuously as the temperature is lowered. If the CDW were to adhere strictly to a specified superstructure such as the $19\ ^{2}/_{3}$ - by - $2\ ^{2}/_{3}$, it could only increase the size of the domains with discrete jumps of 3x1 (12Å), adding one more commensurate CDW wavelength to each domain with each jump. Our STM data does not support this last conclusion (see Fig. 6-16 and 6-20). Also, as is illustrated in Fig. 6-20, our data does not appear to follow any particular family of superstructures.

In conclusion, in the **NC** phase of 1T-$TaS_2$ we have shown unequivocally that a true discommensurate domain structure exists, and analyzed this structure at 215K, 225K, 273K, 295K, and 343K. We find that the domain size increases monotonically with decreasing temperature, but that the angle of the CDW relative to the lattice, $\Phi$, does not continuously approach the commensurate angle at the transition temperature. In addition, we find it unlikely that the $19\ ^{2}/_{3}$ - by - $2\ ^{2}/_{3}$ structure, or any other rigorously commensurate superstructure, adequately describes the complicated domain superstructure observed in the STM images.

| | CDW angle $\Phi$ | CDW wavelength $\lambda$ | domain orientation |
|---|---|---|---|
| 18 - by - 5 structure | 11.93° | 11.68Å | 11.93° |
| $19\ ^{2}/_{3}$ - by - $2\ ^{2}/_{3}$ structure | 11.76° | 11.72Å | 6.275° |
| our STM measurements at 295K | 11.73° ± 0.16° | 11.78Å ±.12Å | 6.9° ± 2.4° |

Table 6-1 Comparison of our room temperature STM data with the properties of the 18 - by - 5 and the $19\ ^{2}/_{3}$ - by - $2\ ^{2}/_{3}$ structures.

[1]K.Nakanishi, H.Takatera, Y.Yamada, and H.Shiba, J. Phys. Soc. Jpn. **43**, 1509 (1977); K. Nakanishi and H. Shiba *ibid.* **43**, 1893 (1977).

[2]K.Nakanishi and H.Shiba, J. Phys. Soc. Jpn **53**, 1103 (1984).

[3]R.E.Thomson, U.Walter, E.Ganz, J.Clarke and A.Zettl, Phys. Rev. B **38**, 10734 (1988).

[4]G.Gammie, S.Skala, J.S.Hubacek, R.Brockenbrough, W.G.Lyons, J.R.Tucker and J.W.Lyding, J. of Microsc. **152**, 497 (1988).

[5]X.L.Wu and C.M.Lieber, Phys. Rev. Lett. **64**, 1150 (1990); X.L.Wu and C.M.Lieber, Science **243**, 1703 (1989).

[6]C.G.Slough, W.W.McNairy, C.Wang and R.V.Coleman, J. Vac. Sci. Technol. B **9**, 1036 (1991); C.G.Slough, W.W.McNairy, R.V.Coleman, J.Garnæs, C.B.Prater and P.K.Hansma, Phys. Rev. B **42**, 9255 (1990).

[7]J.Garnæs, S.A.C.Gould, P.K.Hansma and R.V.Coleman, J. Vac. Sci. Technol. B **9**, 1032 (1991).

[8]R.V.Coleman, W.W.McNairy and C.G.Slough, submitted to Phys. Rev. B.

[9]B. Giambattista, A. Johnson, W.W.McNairy, C.G.Slough and R.V.Coleman, Phys. Rev. B 38, 3545 (1988).

[10]Ref. 13 concludes that the CDW maxima appear identical and are at an angle of 13.9° inside the domains, while Ref. 12 concludes that the maxima are not identical and refs. 12, 14, and 15 measure the angle of the CDW from the real space images at room temperature to be around 12° inside the domains.

[11]C.B.Scruby, P.M.Williams and G.S.Parry, Philos. Mag. **31**, 225 (1975).

[12]K.Nakanishi, H.Takatera, Y.Yamada and H.Shiba, J.Phys. Soc. Jpn. **43**, 1509 (1977).

[13]J.A.Wilson, J. Phys. Condens. Matter **2**, 1683 (1990).

# Chapter VII

## Triclinic phase of 1T-$TaS_2$

The triclinic phase is present only on warming 1T-$TaS_2$ from the commensurate phase (223K<T<283K). X-ray diffraction studies have shown that this is the only phase in which 1T-$TaS_2$ loses its hexagonal symmetry.[1] The first STM study to identify domains in 1T-$TaS_2$ clearly showed them in the **T** phase[2] (part of this work). This was possible because in the **T** phase the domains are very long and narrow, providing a larger number of CDW maxima (or minima) to compare to demonstrate a high degree of similarity.

Figure 7-1 is a low-resolution STM image 1T-$TaS_2$ in the **T** phase at 225K which does not exhibit atomic resolution. This image shows a very strong amplitude modulation of the CDW. An amplitude modulation of this degree is quite unusual; more often, the domains are only barely discernable in the real space data.

Figure 7-2(a) is a top view of a high-resolution STM image of 1T-$TaS_2$ in the **T** phase taken at 250K. In this image the atomic lattice is clearly visible, as well as the CDW. A close inspection of this image will reveal small areas where each CDW minimum is centered on an atomic lattice site. The atom in the minimum appears to have a dark halo around it, which produces a method for determining the registration of the CDW relative to the lattice quite accurately. In so far as this halo seems to be the same size from minimum to minimum, the CDW appears to be commensurate in these areas. This property is illustrated in Fig. 7-2(b) where the positions of the CDW minima which appear to lie directly on top of an atomic

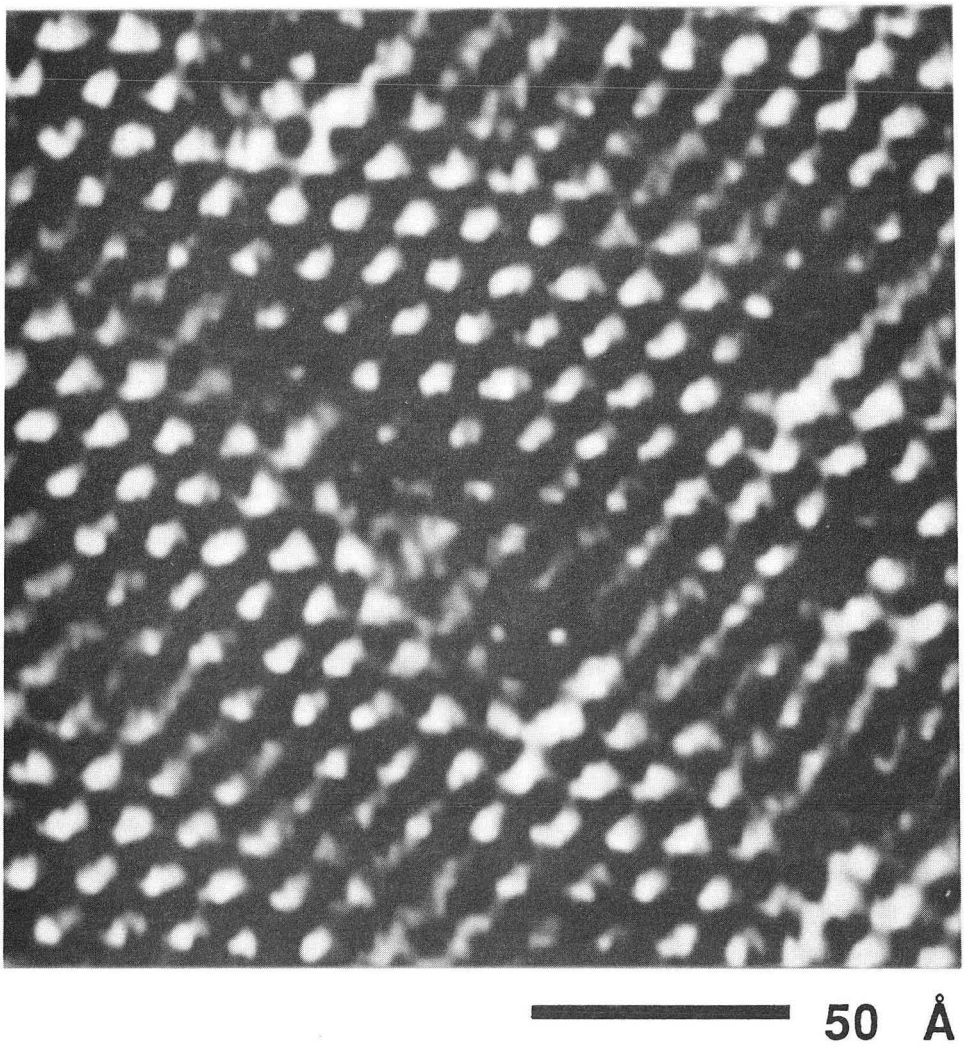


Figure 7-1 1T-$TaS_2$ in the **T** phase at 225K. (XBB-883-2142)

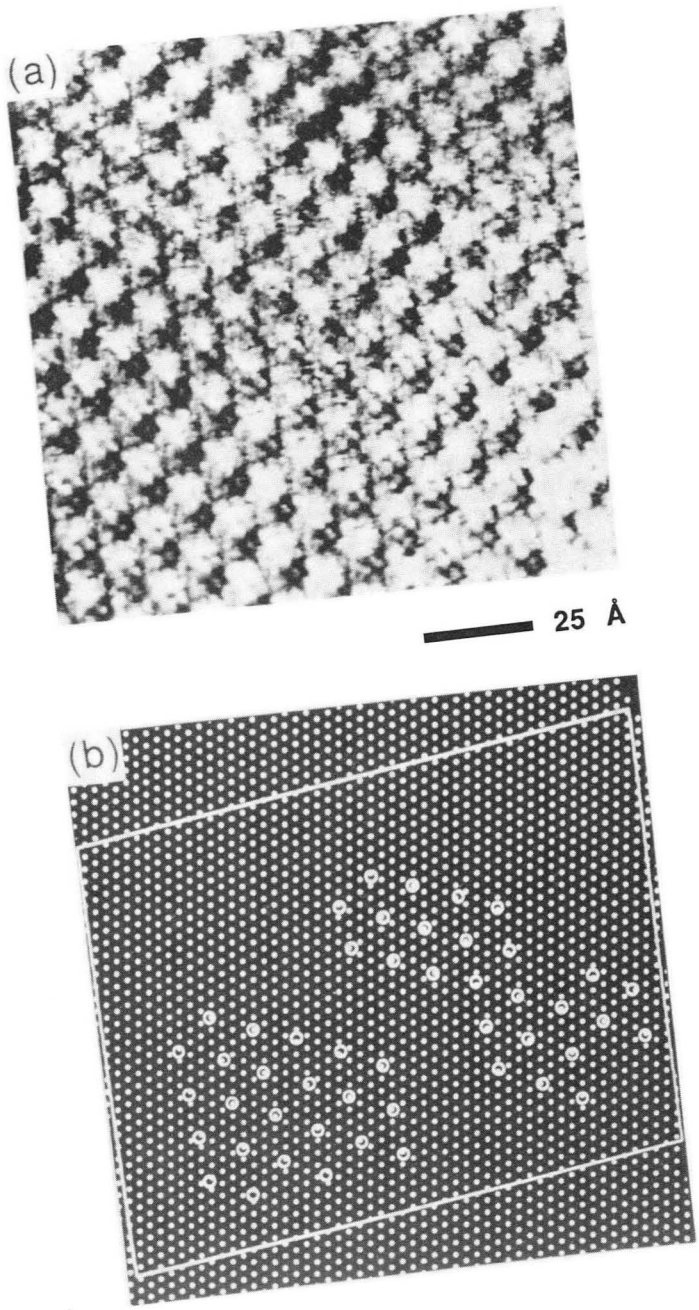


Figure 7-2 (a) 1T-$TaS_2$ in the **T** phase at 250K. Notice the small areas where each CDW minima is identical and has a single atom centered in the minima. (b) Model made from (a) clarifying the positions of the CDW minima relative to the atomic lattice inside the domains. (XBB 884-3296A)

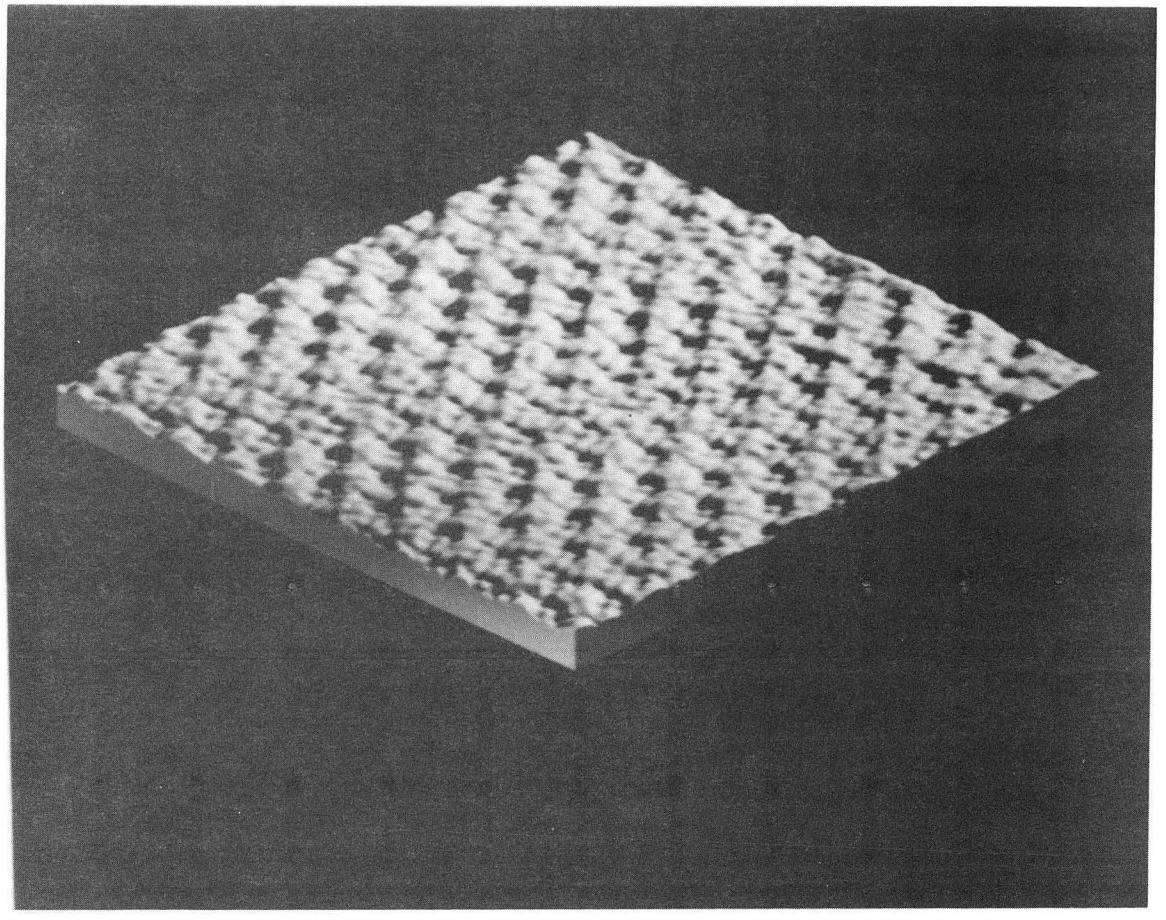

Figure 7-3 A projected view of Fig. 7-2. Notice the clear phase slips in the lines of CDW maxima. (XBB-888-7485A)

lattice site have been plotted along with the atomic lattice. The phase slip of one atomic lattice unit at the DC can easily be seen in this model by viewing it at a glancing angle along the direction of CDW minima rows. In Fig. 7-3, a projected view of the same data shown in Fig. 7-2(a), it is also possible to see the phase slips along the rows of CDW maxima, making the DCs quite clear. However, as was discussed in Chapter VI, a superior way of identifying presence of DCs is to make use of the Fourier transform (FT). In order to produce a high-quality FT, however, it is necessary to use a larger image that contains many domains.

Figure 7-4(a) is too large to resolve the atomic lattice. In this image the small bright dots are the CDW maxima. Close inspection of the image reveals a series of narrow diagonal lines running across the image. In four out of five extensive sets of images taken on three samples we have found similar long narrow stripes that run approximately parallel across the entire area of the surface which we are able to sample (1 $\mu m^2$). These lines are 60-70 Å apart and at an angle of 26° ± 2° relative to the CDW. However, in the discommensuration model of Nakanishi and Shiba, the DCs were calculated to be 40 Å apart and at an angle of less than 1° relative to the CDW at 225K.[3]

Figure 7-4(b) is the FT of the data shown in 7-4(a). In this figure the satellite spots around both the first order and higher order CDW spots are clearly visible. These spots are very reminiscent of the satellite spots seen in the FT of the computer generated simulation of the discommensurate CDW in the **NC** phase discussed in part (a) of Chapter VI and of those seen in the FTs

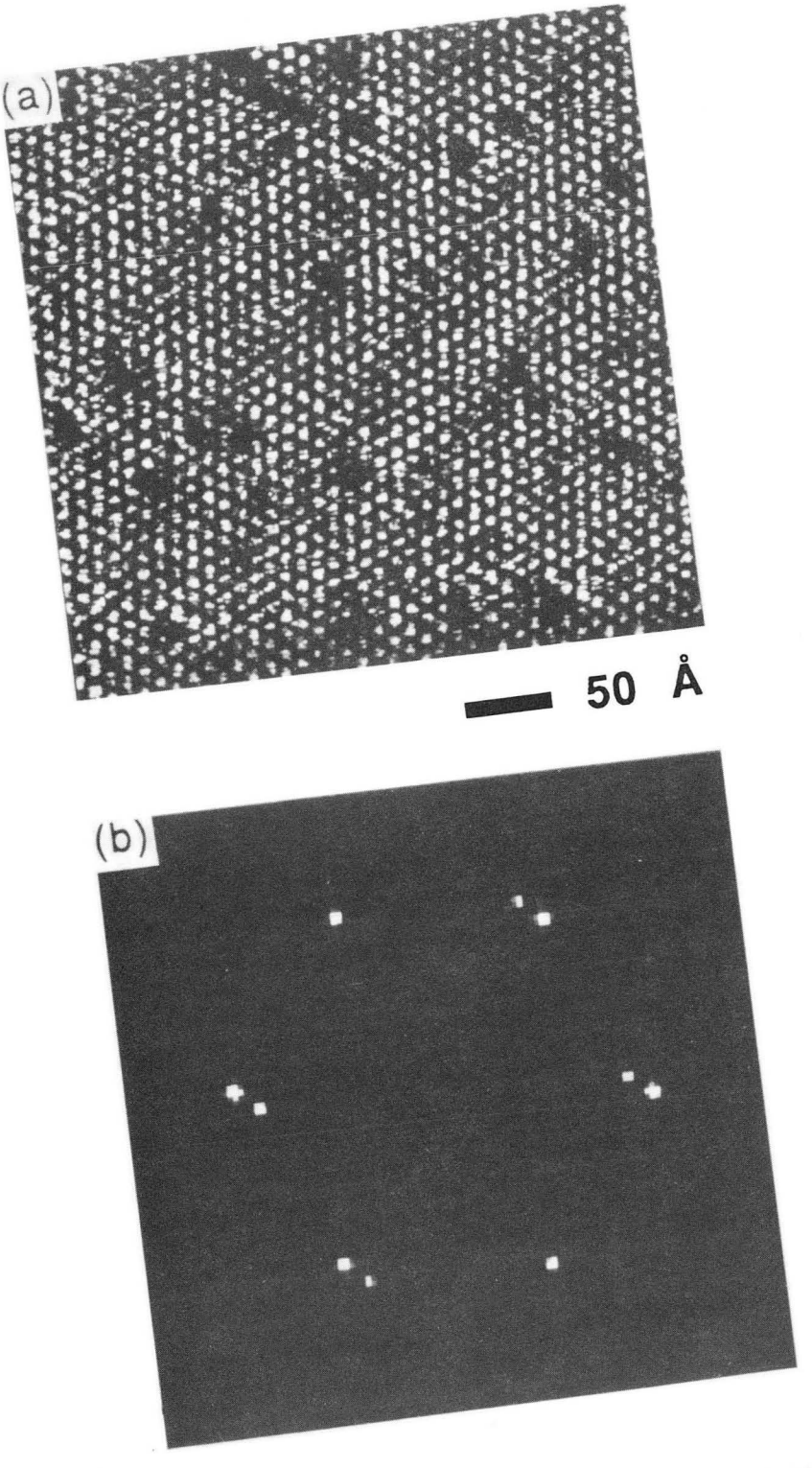


Figure 7-4 (a) Apodized real space data of 1T-$TaS_2$ in the **T** phase at 225K. (b) Fourier transform of (a). (XBB-910-8772A)

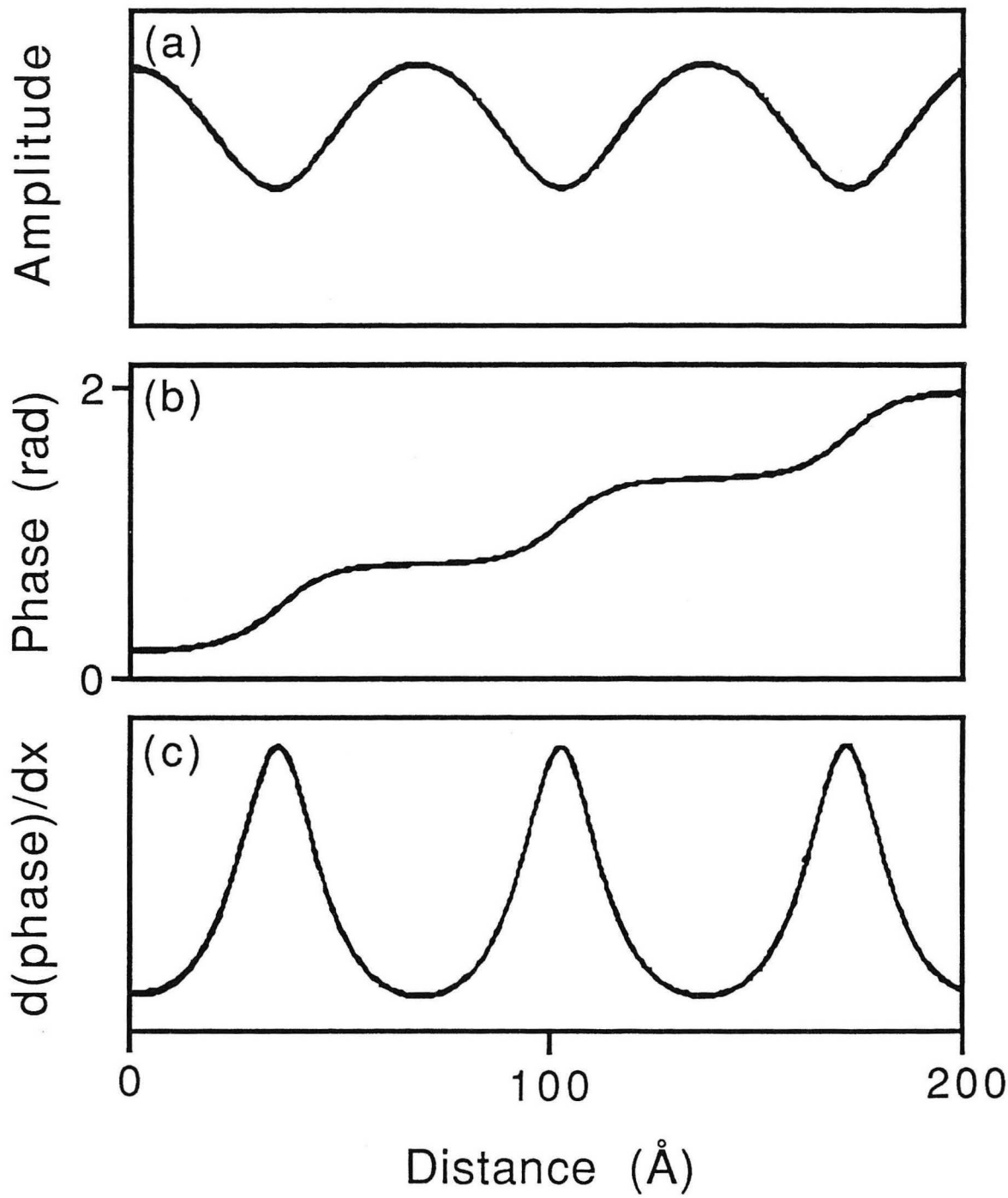


Figure 7-5 Graphs generated by an analysis of the satellite spots in Fig. 7-4(b). (a) CDW phase vs. distance, (b) CDW amplitude vs. distance, (c) derivative of the CDW phase vs. distance.

shown of experimental data from the **NC** phase in part (b) of Chapter VI. We have measured the position and intensity of the satellite spots in the FTs of our experimental data to determine the size of the domains, the orientation of the CDW inside the domain and the width of the DC. Figures 7-5(a)-(c) are graphs determined from the satellite positions and intensities in Fig. 7-4(b). In the regions where the phase is constant, the CDW is commensurate From these figures it is clear that 1T-$TaS_2$ exhibits strong DCs in the **T** phase with both amplitude and phase modulations.

However, as mentioned above, the size and orientation of the domains seen in the STM images are significantly different from those predicted by the stretched honeycomb model of Nakanishi and Shiba[3]. The stretched honeycomb model was based on measurements of only the fundamental CDW wavevectors obtained by x-ray diffraction by Tanda and Sambongi.[1] As in the **NC** case, which was discussed in Chapter VI, the size and shape of the domains in the **T** phase are very closely related to the moiré pattern obtained by allowing the CDW superlattice to beat with the underlying atomic lattice. The distance and direction between maxima of interference in the moiré pattern are necessarily the same as the distance and direction between domain centers when true domains are present. This implies that all that is required to predict the qualitative size and shape of domains is a knowledge of the fundamental CDW wavevectors. Indeed, this is the only information from the x-ray diffraction study that was used in deriving the stretched honeycomb model.

However, as was discussed in Chapter VI, the satellite peaks near the fundamental CDW wavevector peaks are the signature of true domains and DCs, and the observation of these peaks is necessary to confirm the existence of a discommensurate structure. Since no satellite peaks were reported in the original x-ray diffraction study,[1] my co-worker, Brian Burk, undertook an x-ray diffraction study to search for these peaks. His findings are illustrated in Fig. 7-6. One can immediately see the source of the breaking of the hexagonal symmetry in the **T** phase: two of the CDW wavevectors are rotated clockwise from the commensurate wavevector and one is rotated anticlockwise. Using these new measurements of the fundamental CDW wavevectors, we developed new domain models for the **T** phase and calculated the locations of the satellite spots produced by these models. One set of satellite spots was located near their calculated positions, confirming the particular domain structure present in this phase. This domain model is illustrated in Fig. 7-7. In this striped model the domains are about 60Å wide and the DCs run at an angle of about 24.5° relative to the CDW orientation. This is in excellent agreement with the findings from the STM data (60-70Å wide and an orientation of 26° ± 2°). We therefore conclude that in the **T** phase the CDW is in a striped domain configuration which is essentially identical both on the surface and in the bulk of the crystal.

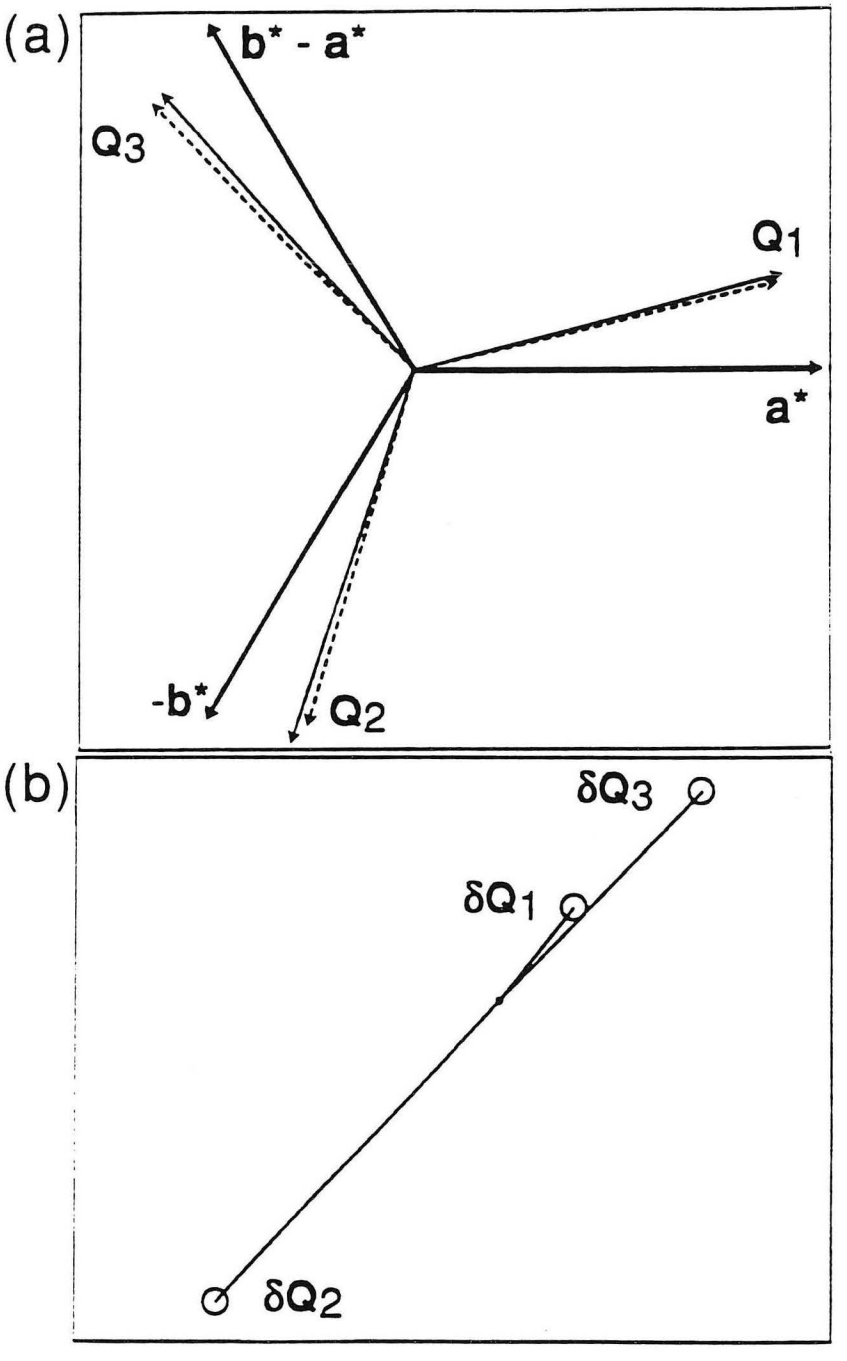


Figure 7-6 X-ray diffraction study results (a) plot of the fundamental CDW wavevectors relative to the commensurate wavevectors, (b) plot of the deviations of the fundamental CDW wavevectors from the commensurate wavevectors (Drawings courtesy of B. Burk.)

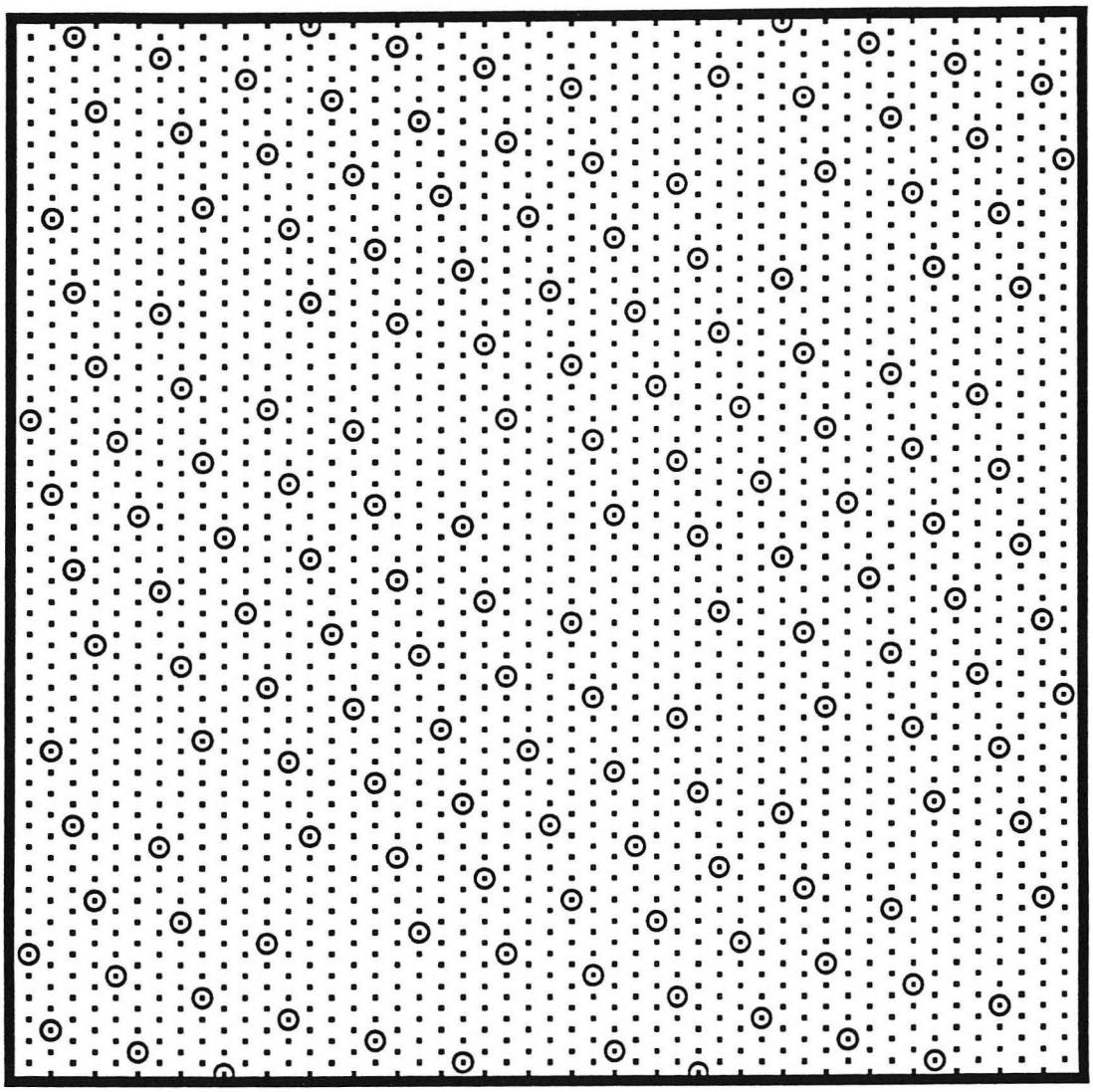

Figure 7-7. Schematic of the new striped model developed from the x-ray diffraction data illustrated in Fig. 7-6.

[1]S.Tanda and T.Sambongi, Synth. Methods **11**, 85 (1985); S.Tanda, T.Sambongi, T.Tani and S.Tanaka, J. Phys. Soc. Jpn. **53**, 476 (1984).

[2]R.E.Thomson, U.Walter, E.Ganz, J.Clarke and A.Zettl, Phys. Rev. B **38**, 10734 (1988).

[3]K.Nakanishi and H.Shiba, J. Phys. Soc. Jpn. **53**, 1103 (1984).

# Chapter VIII

## Blue Bronze

Unlike 1T-$TaS_2$, several materials which exhibit CDWs also exhibit Fröhlich conductivity, or the sliding of the CDW under the influence of a static electric field. In these materials, the CDW is less strongly pinned than it is in 1T-$TaS_2$, allowing it to respond to the applied external field. Many groups have studied sliding CDWs indirectly, making many kinds of transport measurements. A great deal of effort has been directed towards using the STM not only to study the static CDW present at the surface, but also towards using it as a possible tool to investigate directly the dynamics of Fröhlich conductivity.

There are only a few systems known to show Fröhlich conductivity at reasonably low electric fields. These include $(TaSe_4)_2I$, $(NbSe_4)_{10/3}I$, $NbSe_3$, $TaS_3$, and the two blue bronzes $K_{0.30}MoO_3$ and $Rb_{0.30}MoO_3$. The transition metal trichalcogenides $NbSe_3$ and $TaS_3$ grow in needle-like crystals typically less than 100 μm in diameter, making them difficult to use as STM specimens. The halogenated transition metal tetrachalcogenides $(TaSe_4)_2I$ and $(NbSe_4)_{10/3}I$ have quasi-2D crystal structure and are therefore candidates for STM studies, but their rapid oxidation complicates surface studies. The blue bronzes, on the other hand, form large cleavable crystals which are relatively inert, making them practical specimens for STM experiments. Recently, two groups have

published STM images of blue bronze at room temperature above the CDW transition temperature $T_P$=180K.[1,2]

In this chapter I will discuss our attempts to image the CDW in blue bronze at temperatures below $T_P$. Although we obtained STM images resolving the lattice structure at 295K, 143K and 77K we were unable to find evidence of the CDW. I also describe the surface CDW structure calculated from x-ray and neutron diffraction satellite lines and discuss possible reasons why we did not observe this superstructure in our STM images.

The blue bronzes, $M_xMoO_3$ ($0.24 < x < 0.30$, M = Na, K, and Rb), crystallize into the monoclinic C2/m structure with $a_o$ = 18.25 Å (18.94 Å), $b_o$ = 7.560 Å (7.560 Å), $c_o$ = 9.855 Å (10.040 Å), and $\gamma$ = 117.53° (118.83°) with 20 formula per unit cell for $K_{0.30}MoO_3$ ($Rb_{0.30}MoO_3$).[3,4] These compounds form a layered structure with sheets of distorted $MoO_6$ octahedra (corner shared) separated by, but also held together by, the alkali-metal atoms. These sheets are composed of units of ten octahedra, eight of which share edges to form a zig-zag chain in the **[102]** direction. The extra two octahedra, referred to as the "hump" octahedra in Ref. 5, share an adjoining edge with two of the chain octahedra, making them slightly displaced from the chain octahedra. These units of 10 octahedra in turn share corners of the chain octahedra of adjoining unit cells to form infinite Mo-O sheets parallel to the **b-[102]** plane.

Because the bonds between the sheets of these Mo-O chains are weak, the crystals are easily cleaved parallel to the **b** and **[102]**

plane. We determined the positions of the alkali-metal atoms and the molybdenum-oxygen octahedra on this surface from the x-ray diffraction data.[3,5] The symmetry of the surface unit cell is shown in Figs. 8-1 and 8-2. For concentrations of $x < 0.30$ the blue bronzes are nonstochiometric because not all of the interstitial (interlayer) positions are occupied by the M atoms. For x=1/3, the neighboring phase of red bronze is formed.

Below $T_P$ = 180K an incommensurate CDW is formed in the blue bronzes. This creates a gap in the conduction band and therefore gives rise to semiconducting behavior[6] below $T_P$. This phase transition affects nearly all microscopic and macroscopic quantities measured below $T_P$. A CDW in blue bronze was first postulated by Travaglini *et al.* in 1981[7] and was subsequently confirmed by nonlinear electronic transport measurements[8] and by measurement of a Kohn anomaly in the molybdenum-oxygen octahedra along the **b*** direction.[9,10] Recently it was suggested that below T = 100K the CDW undergoes an incommensurate-commensurate phase transition.[11] although the occurrence of such a "lock-in" transition is still controversial. The threshold field for depinning the CDW, $E_T$, varies from 50 to over 250 mV/cm for T > 25K. [12]

We have calculated the projection of the CDW on to the cleavage plane in order to compare the CDW periodicity as well as the lattice periodicity to the observed periodicity of our STM images. The cleavage plane in blue bronze is defined by the **b** and **[102]** crystal axes, and the CDW wavevector is known from x-ray diffraction and neutron scattering data to be[9,11,13]

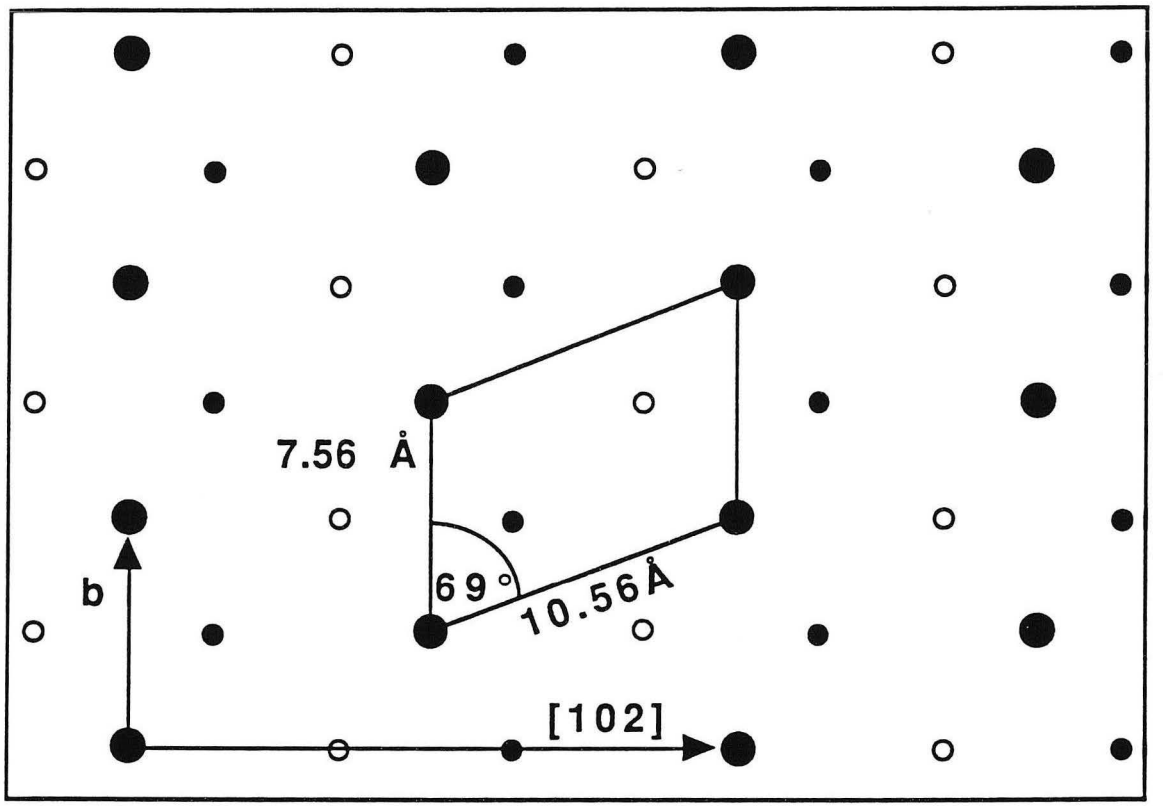


Figure 8-1. Positions of K atoms projected onto the **b - [102]** plane (the cleavage plane) as calculated from x-ray diffraction data. Large solid circles indicate atoms in the uppermost positions in this plane. Small open circles indicate atoms 1.2Å below the plane, and small solid circles indicate atoms 1.2Å above the plane.

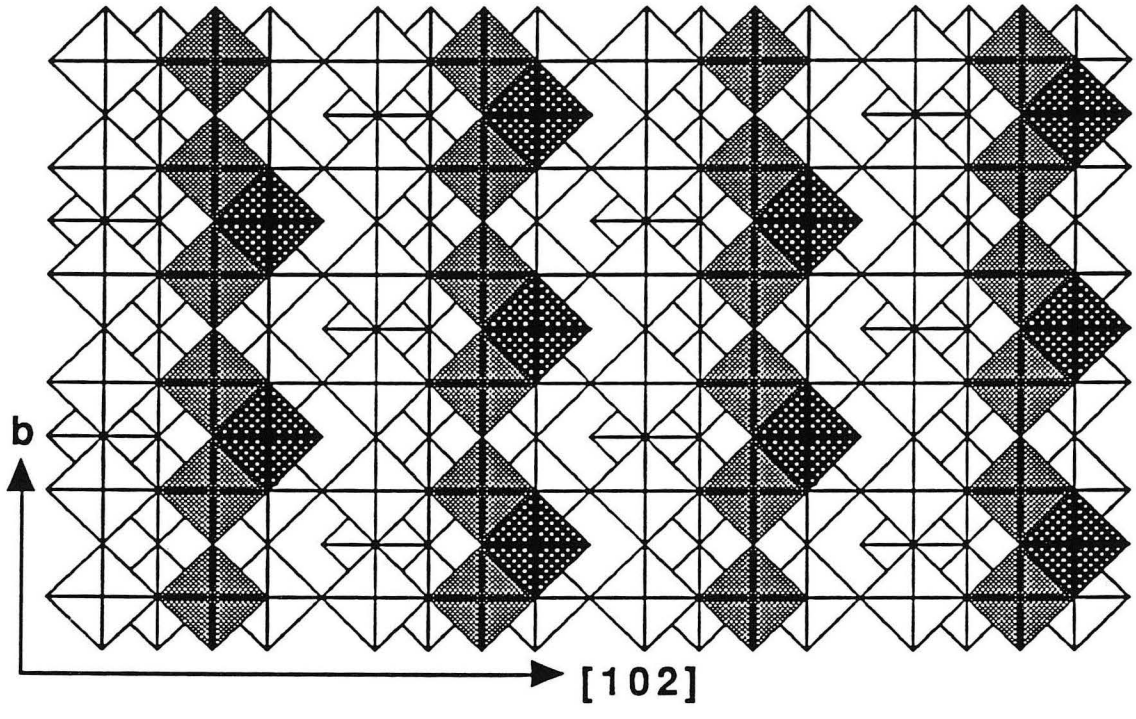


Figure 8-2 Structure of the idealized Mo-O octahedra in the topmost unit cell of the cleavage plane. The centers of the darkest octahedra (the "hump" octahedra) are 1.8 Å below "surface" defined by the **b-[102]** plane. The gray octahedra have centers 2.4 Å below the "surface".

$$\mathbf{q}_{CDW}^{\pm} = \pm\delta\mathbf{b}^* + 0.5\mathbf{c}^*$$

where $\delta = 0.737$ (0.74) for $K_{0.3}MoO_3$ ($Rb_{0.3}MoO_3$).

Projection of the CDW wavevector onto **b** gives:

$$\mathbf{q}_{CDW}^{\pm} \cdot \frac{\mathbf{b}}{|b|} = (\pm\delta\mathbf{b}^* + 0.5\mathbf{c}^*) \cdot \frac{\mathbf{b}}{|b|} = \pm\delta\mathbf{b}^* \cdot \frac{\mathbf{b}}{|b|} = \frac{2\pi\delta}{|b|},$$

while projection of the CDW wavevector onto **[102]** gives:

$$\mathbf{q}_{CDW}^{\pm} \cdot \frac{\mathbf{[102]}}{|[102]|} = (\pm\delta\mathbf{b}^* + 0.5\mathbf{c}^*) \cdot \frac{\mathbf{a}+2\mathbf{c}}{|[102]|} = \mathbf{c}^* \cdot \frac{\mathbf{c}}{|[102]|} = \frac{2\pi}{|[102]|}.$$

Thus, in the cleavage plane we find:

$$\mathbf{q}_{PROJECT}^{\pm} = 2\pi \left\{ \frac{\pm\delta}{|b|}\frac{\mathbf{b}}{|b|} + \frac{1}{|[102]|}\frac{\mathbf{[102]}}{|[102]|} \right\}.$$

The translation vectors reciprocal to the projected wavevectors are:

$$\mathbf{T}_{PROJECT}^{\pm} = \left\{ \frac{\pm\mathbf{b}}{2\delta} + \frac{\mathbf{[102]}}{2} \right\}.$$

An equivalent basis for the projected CDW translation vectors is:

$$\mathbf{T}_{PROJECT}^{1} = \left\{ \frac{\mathbf{b}}{\delta} \right\} ; \mathbf{T}_{PROJECT}^{2} = \left\{ \frac{\mathbf{b}}{2\delta} + \frac{\mathbf{[102]}}{2} \right\}.$$

Finally, the vector magnitudes and angle between the vectors are:

$$|\mathbf{T}_{PROJECT}^{1}| = 10.2\ \text{Å} ; |\mathbf{T}_{PROJECT}^{2}| = 11.1\ \text{Å} ; \theta = 62.6°.$$

In Fig. 8-3 the CDW surface structure is displayed together with the positions of the "hump" octahedra. The CDW forms a superlattice in the cleavage plane that is commensurate in the

**[102]** direction and nearly commensurate in the **b** direction. In this figure the phase of the CDW with respect to the "hump" octahedra is chosen so that a CDW maximum (open circle) coincides with a "hump" octahedron (solid circle) in the lower left region of the figure. The choice of the CDW phase is arbitrary in the **b** direction since the CDW is incommensurate in this direction. In the **[102]** direction the CDW is commensurate and the phase is chosen so that commensurability is obvious; however, the phase of the CDW may be offset in the **[102]** direction so that CDW maxima may not coincide with "hump" octahedra.

The structural and transport properties of $K_{0.30}MoO_3$ and $Rb_{0.30}MoO_3$ are very similar both above and below $T_P$, which is identical in the two materials. The STM images of the two types of blue bronze are also nearly identical. Thus all results described for $K_{0.30}MoO_3$ in the following discussion also apply to $Rb_{0.30}MoO_3$.

We prepared single crystals of both K and Rb blue bronze for the microscope by evaporating three indium contacts onto the crystals before mounting them on copper sample holders with stycast epoxy (Fig. 8-4). One contact on the center of the rear side of the crystal was used for the tunneling bias voltage. The other two contacts on each end of the top side of the crystal enabled us to apply the electric field necessary to induce Fröhlich conductivity at low temperatures. We scored the crystal with a razor blade before cleaving it with tape; the epoxy protected the contacts during the cleaving process.

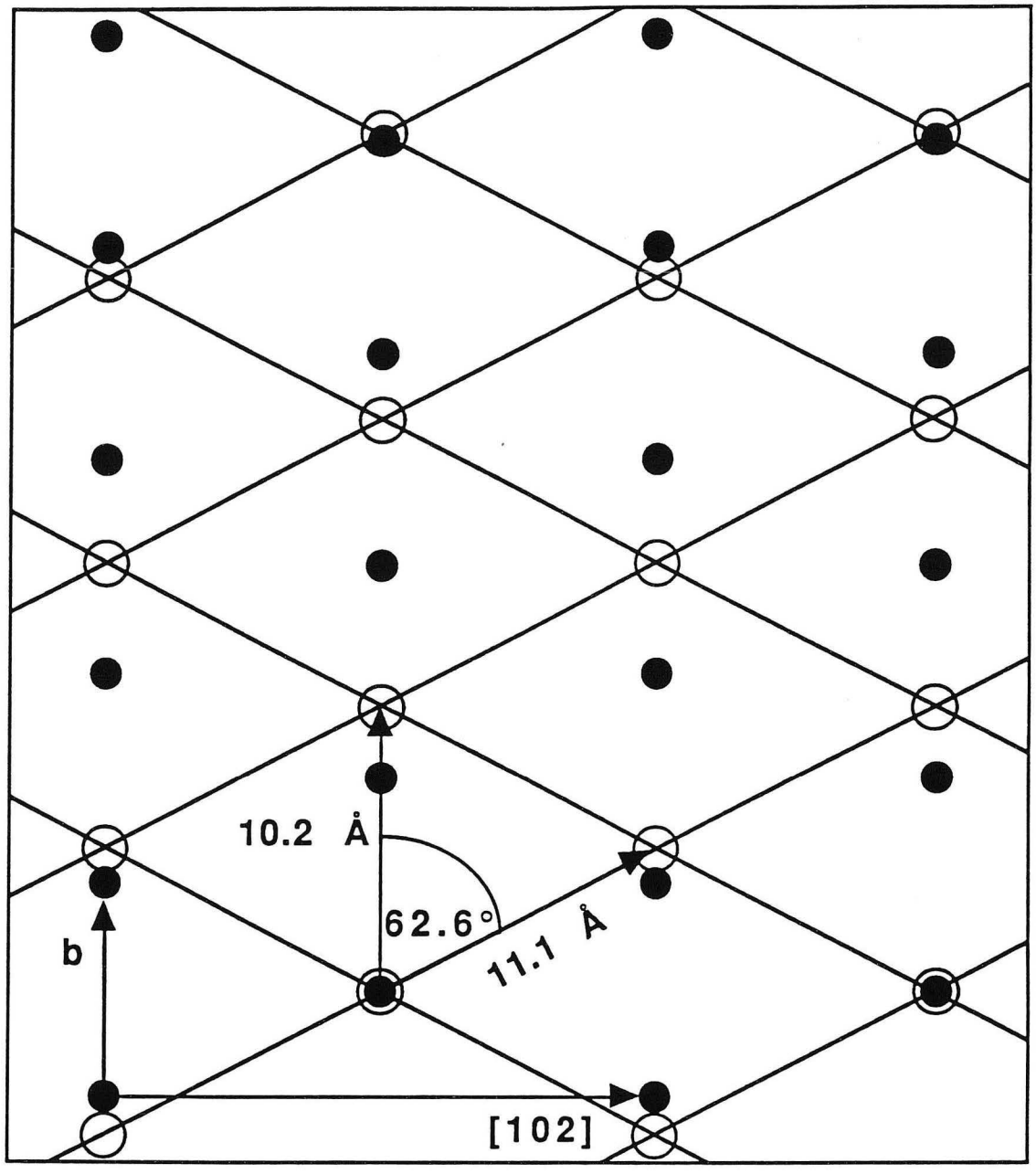


Figure 8-3 The incommensurate charge density wave of $K_{0.30}MoO_3$ in the **b - [102]** plane as calculated from x-ray diffraction and neutron scattering data. The solid lines indicate the CDW wave front with a wavelength of 9.07Å and the open circles indicate the CDW maxima. Solid circles indicate the positions of the underlying "hump" Mo-O octahedra.

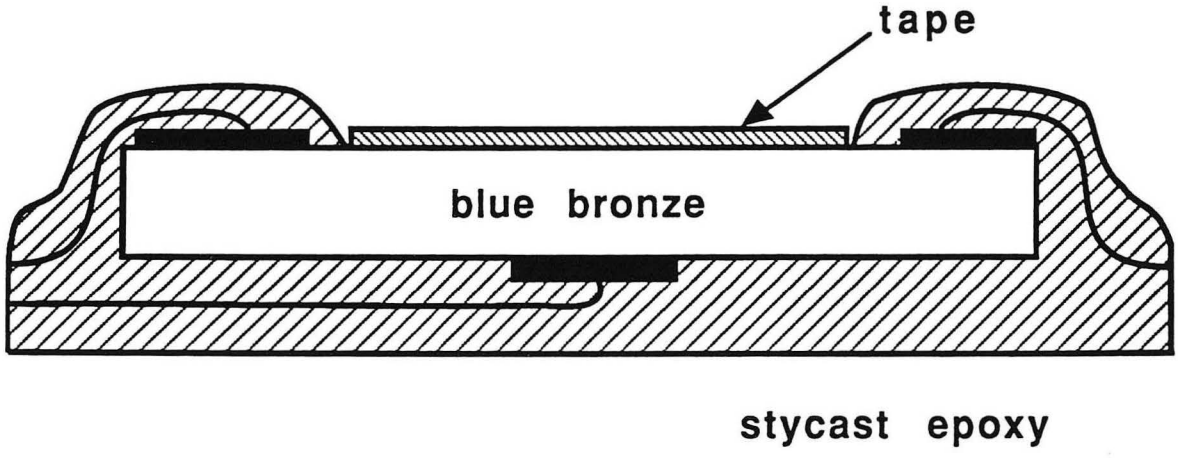


Figure 8-4 Schematic of the sample mounted for use in the STM. The stycast epoxy protects the evaporated indium contacts while the sample is cleaved with tape.

Initial test runs with samples cleaved in air did not produce images with atomic resolution. Instead we obtained pictures showing large structures which were stable but not periodic (Fig. 8-5). We attributed these structures to surface contamination and subsequently worked with samples either cleaved and handled in clean $N_2$ gas or cleaved under hexadecane oil. In the latter case, images at room temperature were obtained with the oil on the surface. We obtained low temperature images by dissolving the hexadecane in pentane and working in a bath of pentane at its melting point (143K), as described in Chapter 2. These cleaner samples yielded images with atomic resolution at all three temperatures (see Figs. 8-6 - 8-8).

Figure 8-6 is an example of the images we obtained at room temperature. The clear periodic structure in Fig 8-6 reflects the periodicity of the rhomboid unit cell of blue bronze. An analysis of 14 images taken at 295K (from 9 samples) yields values of nearest neighbor distances of 7.4Å ± 0.3Å and 10.4Å ± 0.4Å and an angle between the two nearest neighbor directions of 68°± 3°. Our calculations from x-ray diffraction data on $K_{0.30}MoO_3$ yield a surface unit cell with crystal lattice translation vectors of 7.56 Å in the **b** direction and 10.56 Å in the **[112]** direction. The angle between these two lattice vectors is 69°. Thus, within our experimental error, the structure observed in the STM images agrees with the calculated crystal surface lattice translation vectors with regard to both the lattice constants and the angle.

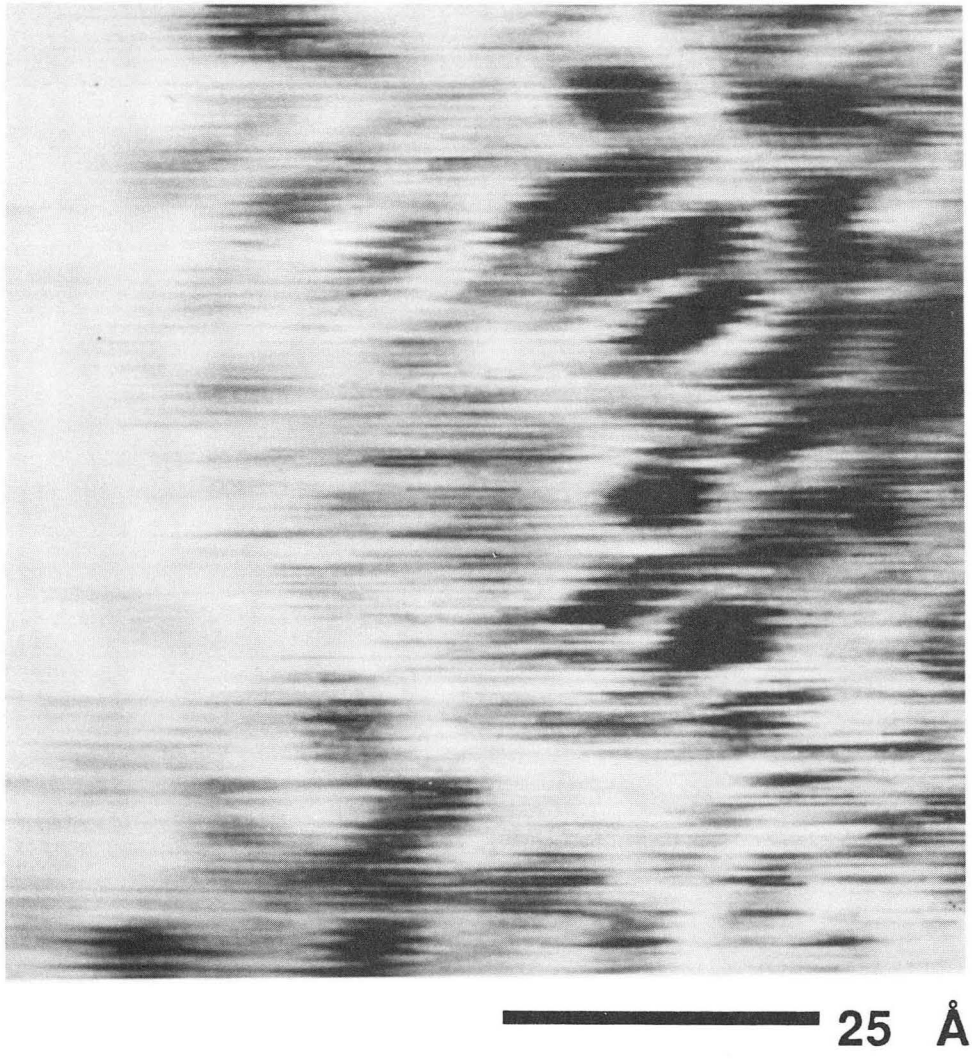


Figure 8-5 STM image of contaminated $K_{0.30}MoO_3$ surface at 143K.

(XBB-914-3024)

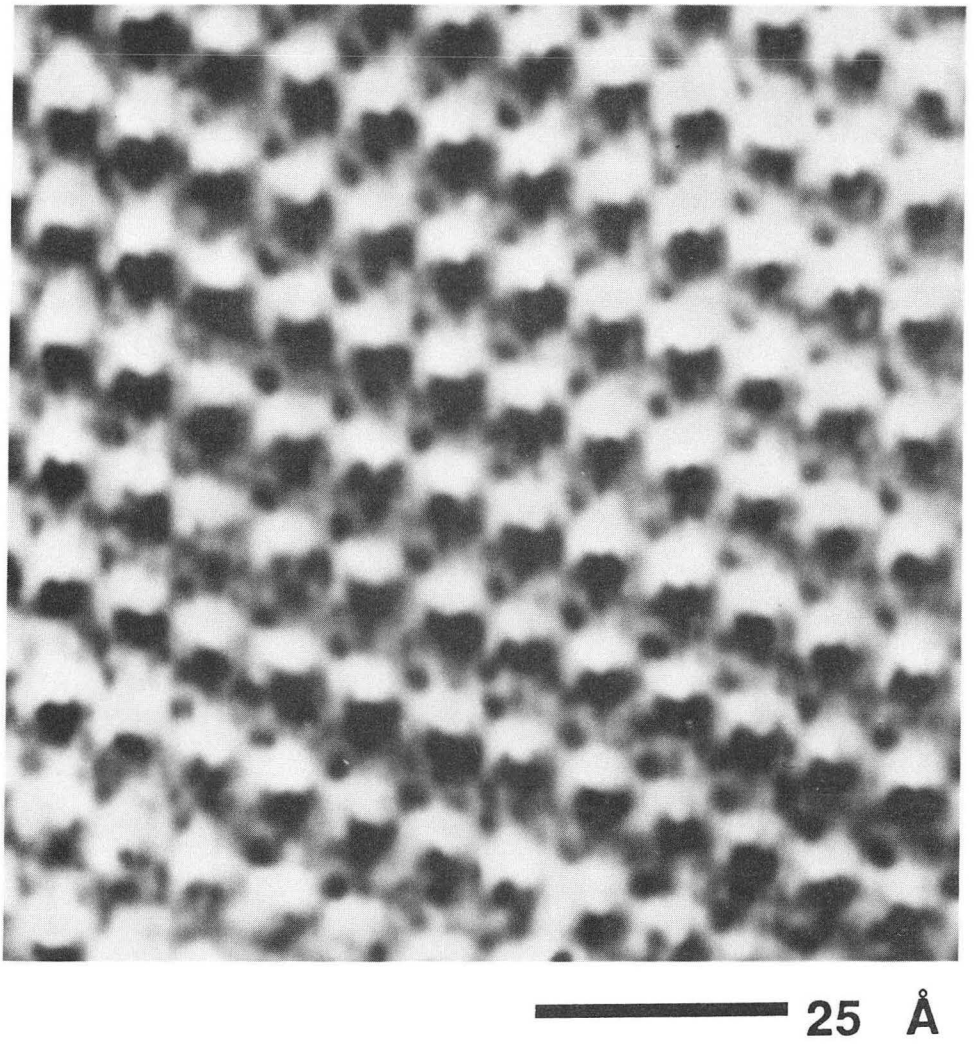


Figure 8-6 STM image of $K_{0.30}MoO_3$ at 295K. A single maxima per surface unit cell is resolved and is probably due to the "hump" octahedra. (XBB-914-3025)

Figures 8-7 and 8-8 are images of the sample in the proposed commensurate phase (77K) and in the incommensurate phase (143K), respectively. (Figure 8-8 is the only image shown in this thesis that was taken in the constant current mode and took about 30 seconds to acquire.) Comparing either figure with Fig. 8-6, we conclude that we are again imaging merely the surface lattice unit cell with no evidence of the CDW. An analysis of 7 images (from 5 samples) taken at 77K and at 143K yielded lattice constants of 7.3Å ± 0.6Å and 10.7Å ± 0.4Å and an angle of 68° ± 4°. These lengths agree with the distances and angle given for the atomic lattice but do not agree with those calculated from x-ray diffraction and neutron scattering data[9,11,13] for the CDW in the cleavage plane: 10.2Å and 11.1Å and an angle of 62.6°. There is no indication of any superstructure we could attribute to the CDW.

In another attempt to find the CDW structure we Fourier transformed our images as shown, for example, in Fig. 8-9(a) which is a Fourier transform of Fig. 8-8. For comparison, in Fig. 8-9(b) we display a schematic of the Fourier transform showing the position of the peaks for the atomic lattice and the CDW calculated from x-ray diffraction and neutron scattering data.[9,11,13] A careful examination of Figs. 8-9(a) and (b) shows that the peaks in the Fourier transform of our STM image agree very well with those calculated for the atomic lattice, but that there are no discernible peaks corresponding to the CDW structure.

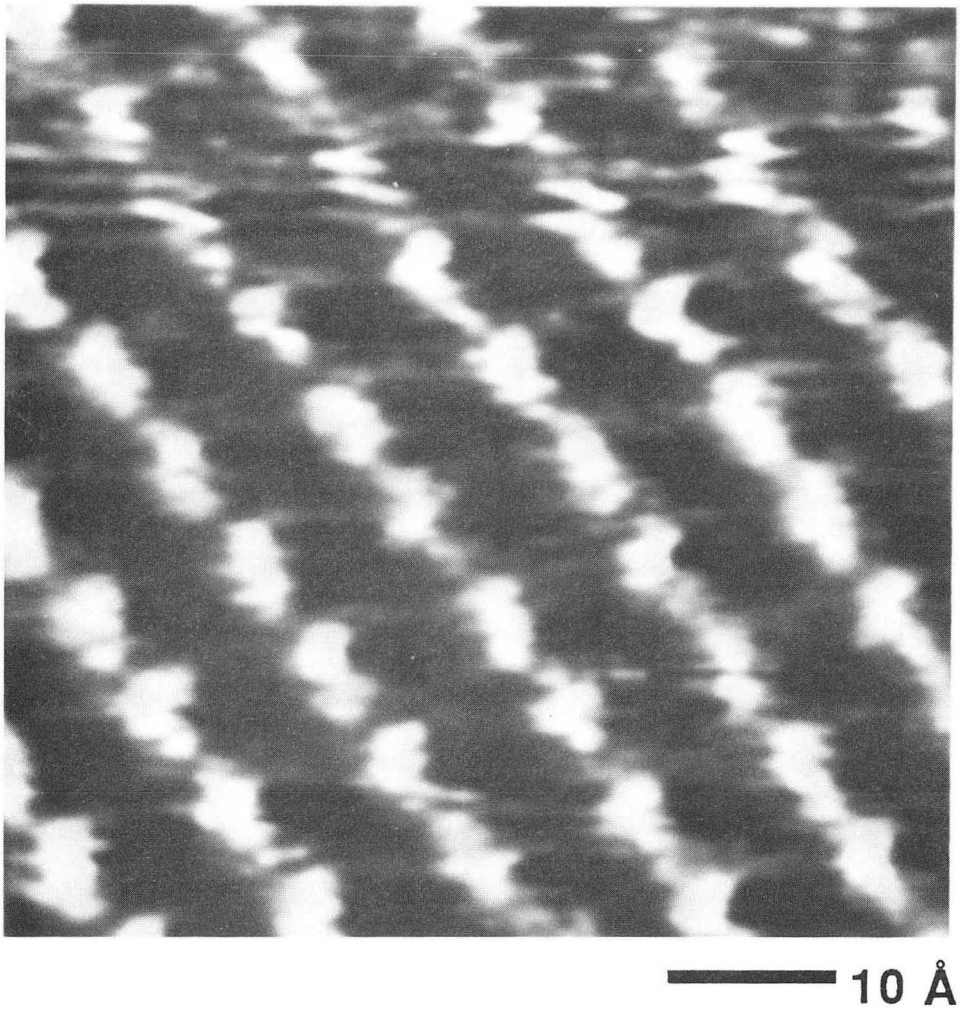


Figure 8-7. STM image of $K_{0.30}MoO_3$ in the proposed commensurate phase at 77K. (XBB-914-3028)

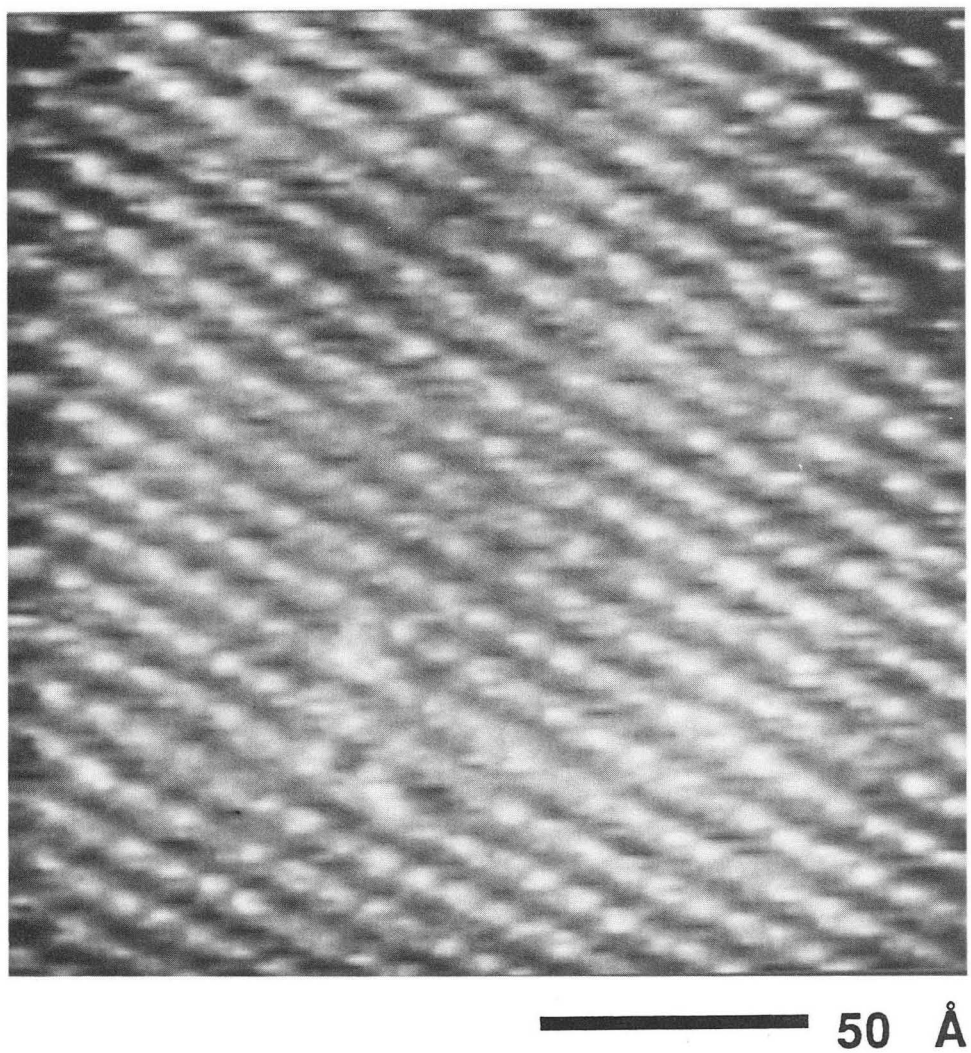


Figure 8-8. STM image of $K_{0.30}MoO_3$ in the incommensurate phase at 143K. The image shows only the Mo-O octahedra and does not display any structure due to the CDW. (XBB-915-3890)

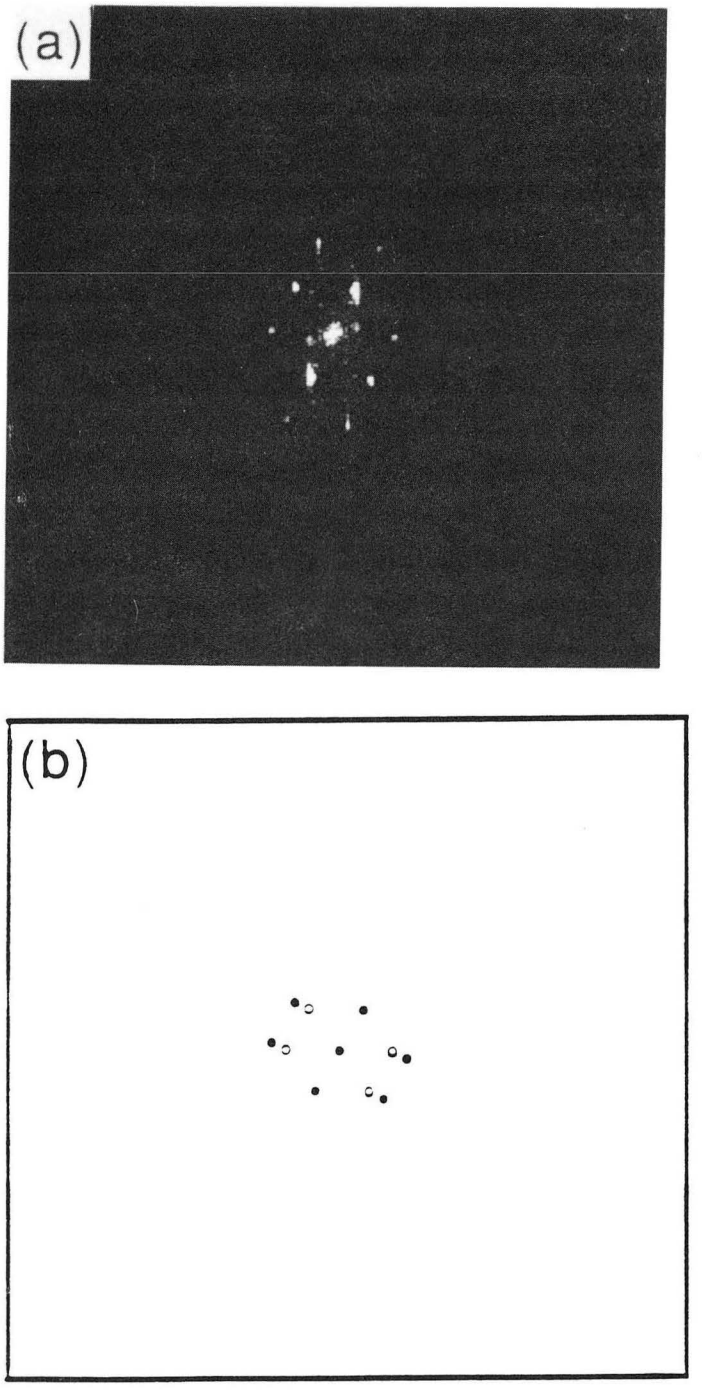


Figure 8-9 (a) Fourier transform of Fig. 8-8 showing the atomic lattice peaks. The two weak peaks nearest the center of the transform are due to 60 Hz noise on the feedback signal. (XBB-915-3889) (b) Schematic showing the calculated positions of the atomic lattice peaks (solid circles) and the CDW peaks (open circles).

In a further attempt to see some indication of the CDW we applied an independently grounded voltage of 200mV to the two side contacts on the top surface of the crystal to produce an electric field 3 times the threshold field $E_T$ (determined by a measurement of dV/dI on the same sample). This procedure did not extinguish or modify the structures observed by the STM at either of the lower temperatures. Therefore, we conclude that none of our STM images shows any evidence of the CDW superstructure.

The inability of our STM to detect a CDW in blue bronze implies that the charge modulation at the surface is nonexistent or at least too weak to be detected. There appear to be at lease two possible explanations for this observation. The first of these is that the CDW is attenuated near the surface. It is well known that the characteristics and behavior of the CDW at the surface can be significantly different from those in the bulk material.[14-17] In fact, it would be surprising for the CDW to extend unchanged to the surface since one expects properties known to affect the CDW, such as the impurity concentration, nonstoichiometry and electronic structure of the crystal, to be quite different on the surface from their values in the bulk. This is especially true in blue bronze, where we expect that the alkali metal atoms not to remain at the surface after cleaving. Also, several studies have indicated that the pinning mechanisms of CDW motion may be influenced by surface effects[14,15,16] such as increased scattering of carriers by the

surface or pinning by defects or different CDW wavevectors at the surface.

Alternatively, the CDW, as measured by STM, may be weak or absent on the surface because it is concentrated on those Mo-O octahedra which are significantly below the surface. To illustrate this possibility, in figure 8-10 I show a schematic of the structure of blue bronze showing the relative displacements (due to the Kohn anomaly) of the atoms in the (010) plane from their room temperature positions (after Sato *et al.*[9]). The top edge of the drawing, which I refer to as the "surface", is defined by the positions of the alkali ions before the cleaving process. (The fact that these ions may have been removed during cleaving is not relevant to the argument, which concerns the relative distances of the various atoms from the surface.) The solid circles represent the uppermost K atoms and the open circles represent the K atoms 1.2Å below this "surface". The Mo atoms closest to the "surface" are 1.8Å below the "surface" and those which undergo the largest displacements are 3.5Å below the "surface". If the CDW is concentrated on the same atoms that are displaced due to the Kohn anomaly, as one would expect, it may be that the greater part of the CDW modulation is too far below the surface to be detected with our STM.

Given our result that the CDW on the surface of blue bronze is either weak or nonexistent, it is of interest to consider previous work relevant to this problem. In 1990, Zhu *et al.*[17] reported that

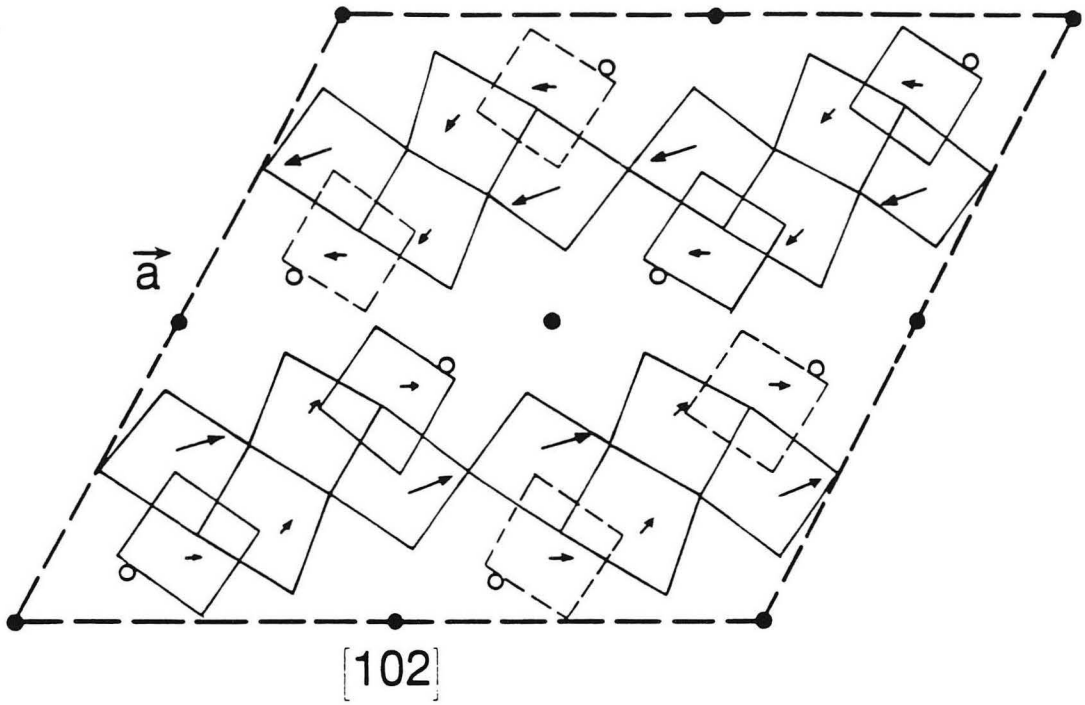


XBL 895-5106

Figure 8-10. Side view of a single unit cell of blue bronze projected onto the plane perpendicular to **b**. The "surface" of the crystal (defined by the **b-[102]** plane) is along the top of the figure. Solid circles are the K atoms in the uppermost positions. Open circles are the K atoms 1.2 Å below the "surface". The Mo atoms are at the center of oxygen octahedra and the three highest sets lie at levels 1.8, 2.4, and 3.5 Å below the "surface". The arrows indicate the relative amplitudes and directions of the displacement of the Mo atoms due to the CDW (after *Sato et al.*[9]).

the CDW in blue bronze was easily detected by grazing incidence x-ray diffraction. In this study, the CDW satellite peak was unchanged at the shallowest incident angle used, which was calculated to have an x-ray penetration depth of 20Å, corresponding to about two and one half Mo-O sheets. If our STM fails to image the CDW because it does not propagate to the surface, then to be consistent with the grazing incidence x-ray diffraction study we have to conclude that the CDW disappears within the last Mo-O sheet. However, our second proposed explanation for our results, that the CDW is concentrated on the Mo atoms which are too far below the surface for our STM to image, is also consistent with the x-ray results.

Our failure to detect the CDW appears to contradict the results of Nomura and Ichimura[18] who detected a peak in the frequency spectrum of the STM tunneling current which they attributed to the presence of a sliding CDW on the surface of a sample biased above its CDW conduction threshhold field. However, these authors were unable to obtain STM images of either the CDW or of the atomic lattice. It is possible that the peak they observed in the frequency spectrum was due to the time-varying voltage (i.e. narrow band noise) induced across the sample by the sliding CDW. This oscillating voltage could have modulated the tip-sample bias voltage of the STM, and hence the tunneling current.

Finally, one might ask what aspect of the atomic lattice the STM images in blue bronze. The periodicity of the STM images

reflects the periodicity of the unit cell of the material, but one would like to know which part of the unit cell, the K atoms or the Mo-O octahedra, is being imaged. An inspection of Figs. 8-1 and 8-2 reveals that the uppermost potassium atoms and the uppermost Mo-O octahedra (the "hump" octahedra in Ref. 5) both produce lattices with identical unit cell vectors (the known surface lattice translation vectors), making it impossible to differentiate between them based only on their measured periodicities. However, from an analysis of the calculated electronic density of states,[5] it seems unlikely that the alkali metal ions would affect the tunneling current because they have no electronic states available near the Fermi level. Furthermore, because the alkali ions are normally held in position by electrostatic forces due to the rest of the atomic lattice, it is unlikely that the ions remain on the surface in their original positions when one half of the material creating their electrostatic environment is removed in the cleaving process. Lastly, since the blue bronzes are generally nonstochiometric, not all of the interstitial (interlayer) positions are expected to be occupied by alkali atoms. Thus if we were imaging the K ions we would expect a very large number of defects, contrary to what we observe. Therefore, we conclude that the periodic structure in our STM images is due to the Mo-O octahedra. In this case, we may be imaging just the uppermost "hump" octahedra (the dark gray octahedra in Fig. 8-2), or, alternatively, each maximum in the STM image may correspond to a blurred image of the group of three Mo-O

octahedra (both the dark and light gray octahedra in Fig 8-2). The latter option was the hypothesis of Heil *et al.*[1] for their room temperature STM data, and Anselmetti *et al.*[2] concluded that it was at least consistent with their data.

In conclusion, we have used our STM to image the atomic lattice in the blue bronzes above the CDW transition temperature (295K), in the incommensurate phase (143K) and in the proposed commensurate phase (77K). At all three temperatures the structure imaged by the STM is consistent with the surface crystal structure of uppermost "hump" octahedra. However, we have not seen any evidence for the CDWs known to exist in these materials at the lower two temperatures. The two most likely reasons for this fact are that either the CDW does not propagate to the surface of the crystal, or, that the CDW is concentrated on the Mo-O octahedra which are too far below the surface to be imaged with our STM.

[1]J.Heil, J.Wesner, B.Lommel, W.Assmus, and W.Grill, J. Appl. Phys **65**, 5220 (1989).

[2]D.Anselmetti, R.Weisendanger, H.-J.Güntherodt and G.Grüner, Europhys. Lett. **12**, 241 (1990).

[3]J.Graham and A.D.Wadsley, Acta Cryst. **20**, 93 (1966).

[4]J.-M.Reau, C.Fouassier, and P.Hagenmuller, Bull. Soc. Chim. France **8**, 2883 (1971).

[5]W.H.Whangbo and L.F.Schneemeyer, Inorg. Chem. **25**, 2424 (1986).

[6]W.Fogle and J.H.Perlstein, Phys. Rev B **6**, 1402 (1972).

[7]G.Travaglini, P.Wachter, J.Marcus and C.Schlenker, Solid State Comm. **37**, 599 (1981).

[8]J.Dumas, C.Schlenker, J.Marcus, and R.Buder, Phys. Rev. Lett. **50**, 757 (1983).

[9]M.Sato, H.Fujishita, S.Sato and S.Hoshino, J. Phys. C **18**, 2603 (1985).

[10]C.Escribe-Filippini, J.P.Pouget, R.Currat, B.H.Hennion and J.Marcus in *Charge Density Waves in Solids* , Lecture Notes in Physics. Vol. 217 edited by Gy. Hutiray and J. Solyom (Springer-Verlag, Berlin, 1985), pp 71-75.

[11]R.M.Fleming, C.F.Schneemeyer and D.E.Moncton, Phys. Rev. B **31**, 899 (1985).

[12]R.M.Fleming, R.J.Cava, L.F.Schneemeyer, E.A.Reitman and R.G.Dunn, Phys. Rev. B **33**, 5450 (1986).

[13]J.P.Pouget, C.Noguera, A.H.Moudden and R.Moret, J.Physique **46**, 1731 (1985).

[14]P.J.Yetman and J.C.Gill, Solid State Commun. **62**, 201 (1987).

[15]J.McCarten, M.Maher, T.L.Adelman, and R.E.Thorne, Phys. Rev. Lett. **63**, 2841 (1989).

[16],J.C.Gill, Europhys. Lett. **11**, 175 (1990).

[17]X.-M.Zhu, R.Moret, H.Zabel, I.K.Robinson, E.Vlieg, and R.M.Fleming, Phys. Rev. B **42**, 8791 (1990).

[18]K.Nomura and K.Ichimura, Solid State Commun. **71**, 149 (1989).

# Chapter IX

## o-$TaS_3$

In a second attempt to study Fröhlich conductivity, my co-workers J. B. Liu, B. Burk and I decided to study orthorhombic tantalum trisulfide (o-$TaS_3$). In this material the CDW readily depins, but the crystals grow in long thin needles, making them difficult to study with STM. However, we found that by very careful positioning of the STM tip above the sample using an optical microscope, we could obtain a tunneling current to the sample in about 50% of our attempts.

The orthorhombic form of $TaS_3$ undergoes a three dimensional Peierls metal-insulator transition at $T_P$=220K. In the "metallic" state above $T_P$, both transport[1] and diffraction[2] experiments suggest fluctuations corresponding to the interesting situation of *uncorrelated* regions of local CDW structure existing in the otherwise undistorted crystal. CDW fluctuations are understood theoretically but they have not been directly observed on a local scale in any CDW material. In the coherent (three-dimensionally ordered) CDW state below $T_P$, the collective CDW mode in o-$TaS_3$ displays "sliding" conduction for applied static electric fields exceeding a threshold impurity-pinning field $E_T$.

In this chapter I discuss our STM studies of o-$TaS_3$ at temperatures above and below $T_P$. Above $T_P$, CDW fluctuation effects are observed directly. In the ordered CDW state below $T_P$, the static CDW is observed with the expected periodicity. Application of static bias fields as high as $7.5E_T$ had no measurable

effect on the surface CDW image. This suggests that either the CDW is strongly pinned and sheared at the surface of the crystal, or moves coherently with an unusual non-constant velocity.

Recently, Gammie *et al.*[3] studied o-$TaS_3$, and observed the S-S lattice spacing along the chain axis at room temperature and the $\lambda_{CDW}= 4c_o$ spacing below the transition temperature of 215K. At 160K they applied an electric field of 5 times greater than the depinning field, but continued to observe the CDW on the surface. This was attributed to the fact that the large anisotropy of o-$TaS_3$ coupled with a disordered crystal surface may have given rise to a local surface electric field much lower than the average value, so that the CDW in the observed region was not depinned.

A second STM study on o-TaS3 was performed by Slough and Slough and Coleman[4] In this study the lattice periodicity was clearly resolved both along and perpendicular to the atomic chains. At 77K, the STM images resolved CDWs on two of the three chains present in the surface unit cell. These CDW's were 180° out of phase with each other, but together they exhibited the expected CDW wavelength and orientation. This study did not report any attempts to depin the CDW.

We synthesized single crystals of o-$TaS_3$ by the usual vapor transport process.[5] The crystals produced were a few centimeters long and approximately 30 μm wide. Single fibers, cut to about 4 mm, were mounted on copper sample holders using insulating stycast epoxy. An electrical contact was made at the each end of the crystals using silver paint.

Because the experiments were always performed on samples in air or in pentane after exposure to air, the surfaces were usually quite contaminated, making it difficult to obtain high quality STM images. We found that samples which had been exposed to air for more than two weeks usually could not be imaged. Even on good samples that had been exposed to air for only a few days, images obtained during a single run could vary dramatically in quality, and usable images were obtained only about 1% of the time.

Despite intensive study, little is known about the crystal structure of o-$TaS_3$. The most probable space group is C222, with the very large unit cell composed of 24 chains and having lattice constants[6] of $a_o$=36.804 Å, $b_o$=15.173 Å, $c_o$=3.340 Å. Crystals of o-$TaS_3$ form long narrow fibers, where the long dimension corresponds to the chain axis and is along the c-direction. X-ray studies have shown that the CDW structure is commensurate with the lattice and has a wavelength[2] of $\lambda_{CDW}=(2a_o, 8b_o, 4c_o)$.

Examples of our data at 295K are shown in Fig. 9-1. As in all our pictures shown here, there is a well-resolved periodicity only in the direction parallel to the chains. For unknown reasons, the lattice is unresolved perpendicular to the chains; the problem is made more difficult by the fact that the crystal structure is not well known. In these images, the smaller periodicity is 3.3 ± 0.5 Å, consistent with the known lattice spacing along the chain of $c_o$ = 3.340 Å. However, we were surprised to observe a superstructure with a larger spacing of $4c_o$, which is consistent with the known CDW wavelength. At room temperature we observed the CDW in about one-half of the pictures which showed atomic resolution, on a

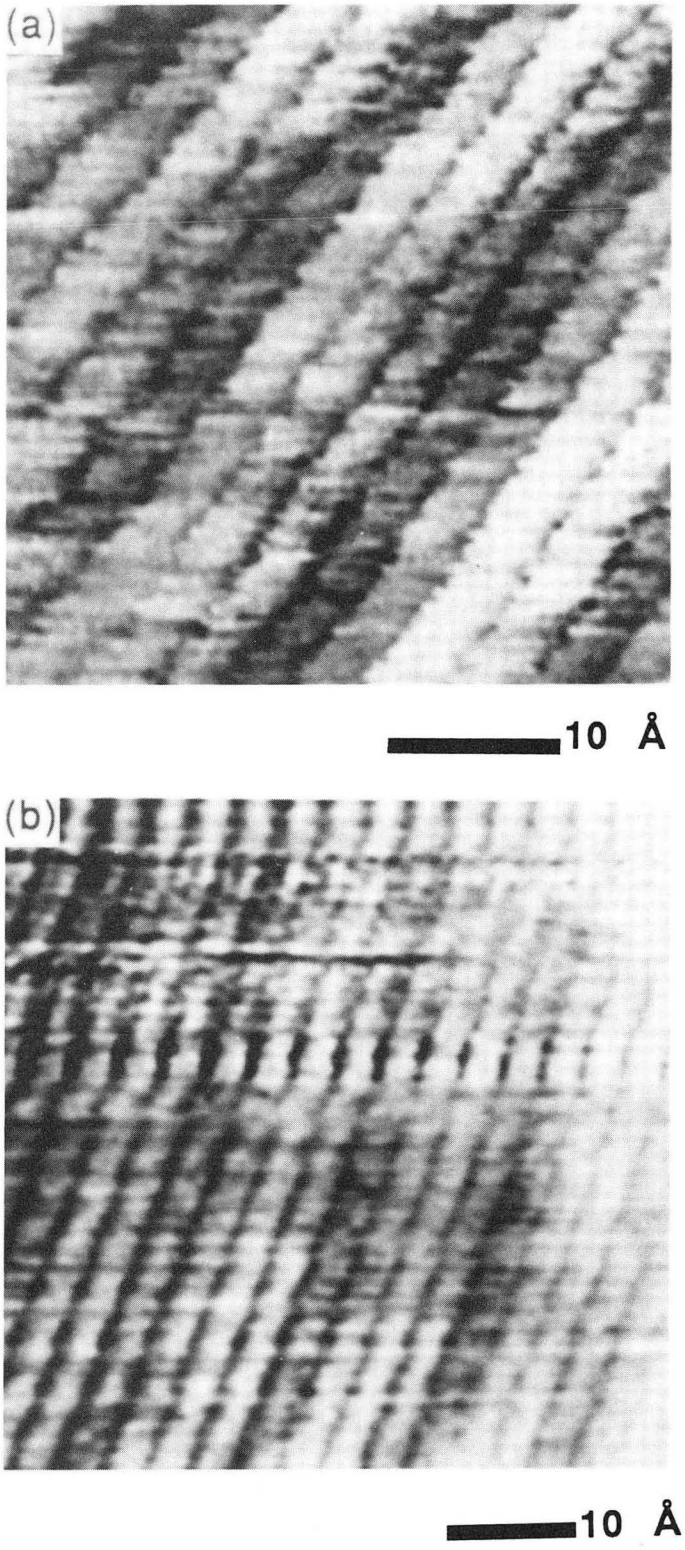


Figure 9-1. STM images of o-$TaS_3$ taken at 295K. Both the lattice and the CDW superstructure are clearly imaged in one dimension in both images. (XBB-910-8950A)

total of 17 out of 31 samples. (The remaining samples were too severely contaminated to be imaged at all. All samples that could be imaged displayed the CDW superstructure at room temperature in at least some images.) In the fluctuation region above 215K, diffraction[2] and transport[1] measurements indicate that the charge density wave is present but is not fully condensed into a coherent state. In our images, the CDW is almost always in phase across the entire image perpendicular to the chain direction, but occasionally it appears to have a wavelength of 3 or 5 $c_o$ in the chain direction, instead of the expected and much more usually observed $4c_o$.

In an attempt to verify that the superstructure observed at room temperature was indeed the CDW, we raised the temperature of two samples to 343K, well above the cut-off of the fluctuation region (~300K[1]). At this temperature our images showed only the one-dimensional lattice periodicity and the CDW modulation disappeared completely. Figure 9-2 is an example of an image taken at 343K. This image appears curved because of strongly fluctuating thermal drifts present when we raised the temperature of the entire STM. We never obtained any evidence of the CDW at this temperature. When the samples were cooled to room temperature, our STM images were identical to those obtained before the temperature was raised, with approximately the same fraction of images showing the CDW as before the temperature was raised.

At low temperatures, well below the transition temperature, the CDW and the lattice periodicities were still visible. Examples are shown in Figs. 9-3. After we had established that a sample produced good images at 143K, we measured the I-V characteristic

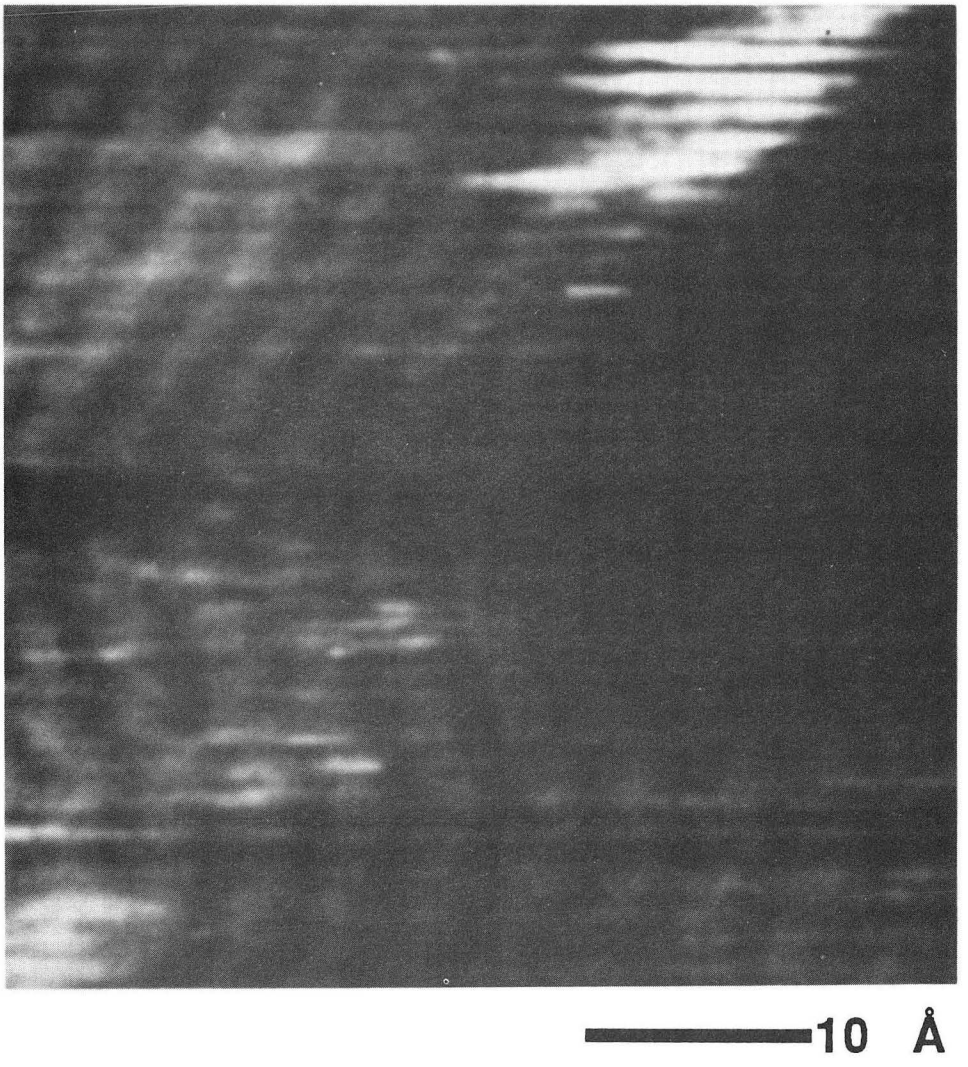


Figure 9-2 STM image of o-$TaS_3$ taken at 343K. Only the atomic lattice periodicity is seen in this case. (XBB-914-3029)

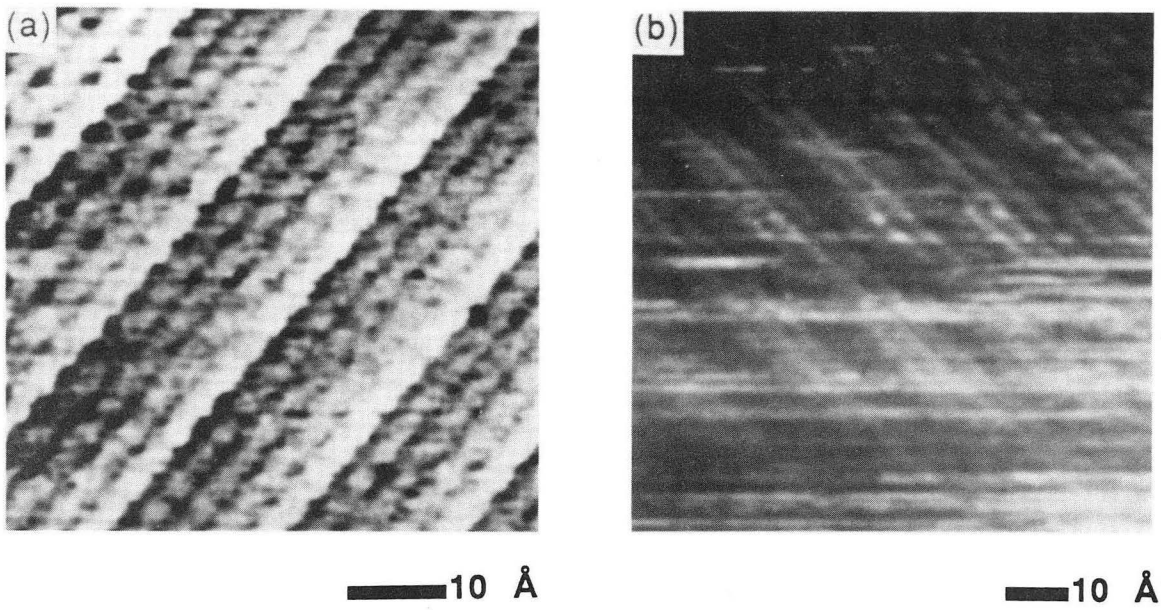


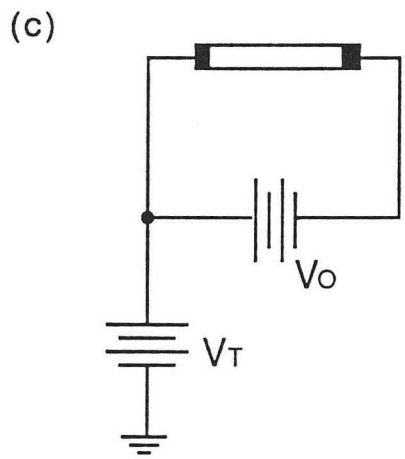


Figure 9-3 STM images of o-$TaS_3$ taken at 143K. Both the lattice and the CDW are visible in (a) without a static electric field applied and in (b) with a static electric field of 1.12V/2.1mm applied, which is 3.1 times the depinning field for this crystal. (XBB-892-1414B) (c) Circuit used to apply the bias voltage ($V_O$) required to depin the CDW. $V_T$ is the STM tunnel voltage.

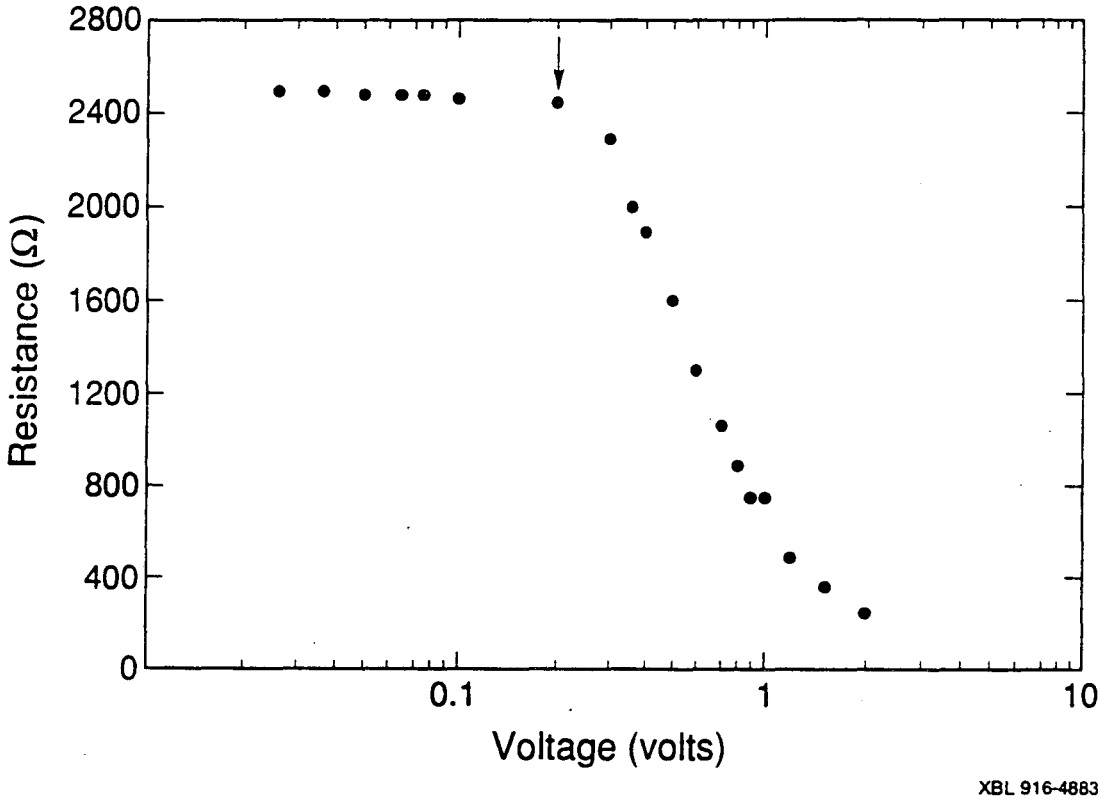


Figure 9-4 I-V characteristic of a sample that exhibited a CDW in a static field of 2.5V/2.1mm. The arrow indicates the field at which narrow band noise peaks first appear.

of the sample to determine the threshold field. The depinning field for the sample imaged in Fig.9-3(b) was 360mV/2.1mm as determined from the I-V curve shown in Fig.9-4. After determining the depinning field, we monitored the STM images for evidence of the CDW periodicity as we varied the bias voltage across the sample from 0V to 3V using the circuit shown in Fig. 9-3(c). The image quality deteriorated as the electric field was increased until above 2.6V/1.5mm it was no longer possible to obtain any STM images that showed periodic or repeatable structures on any samples. However, we were still able to detect the CDW periodicity in images taken with 2.6mV/1.5mm applied to a sample where this was 7.5 times the threshold field. Figure 9-3(b) is an image acquired while the field applied to the sample was 1.12V/2.1mm, or 3.1 times the threshold field for this sample.

The field at which periodic repeatable STM images are no longer obtainable seems to be determined by the noise in the tunneling current and does not represent the point at which the CDW actually begins to slide. We determined this by applying similar size fields across samples at room temperature (where the CDW, although present, would not be expected to depin) and across heavily doped samples. We found that the images deteriorated in the same way with increasing field strength and disappeared completely at approximately the same applied field as when the experiment was done at low temperatures and on undoped samples.

One explanation for the absence of a sliding CDW is that the local electric field at the surface was much less than the average field on the sample, for example, because of sample

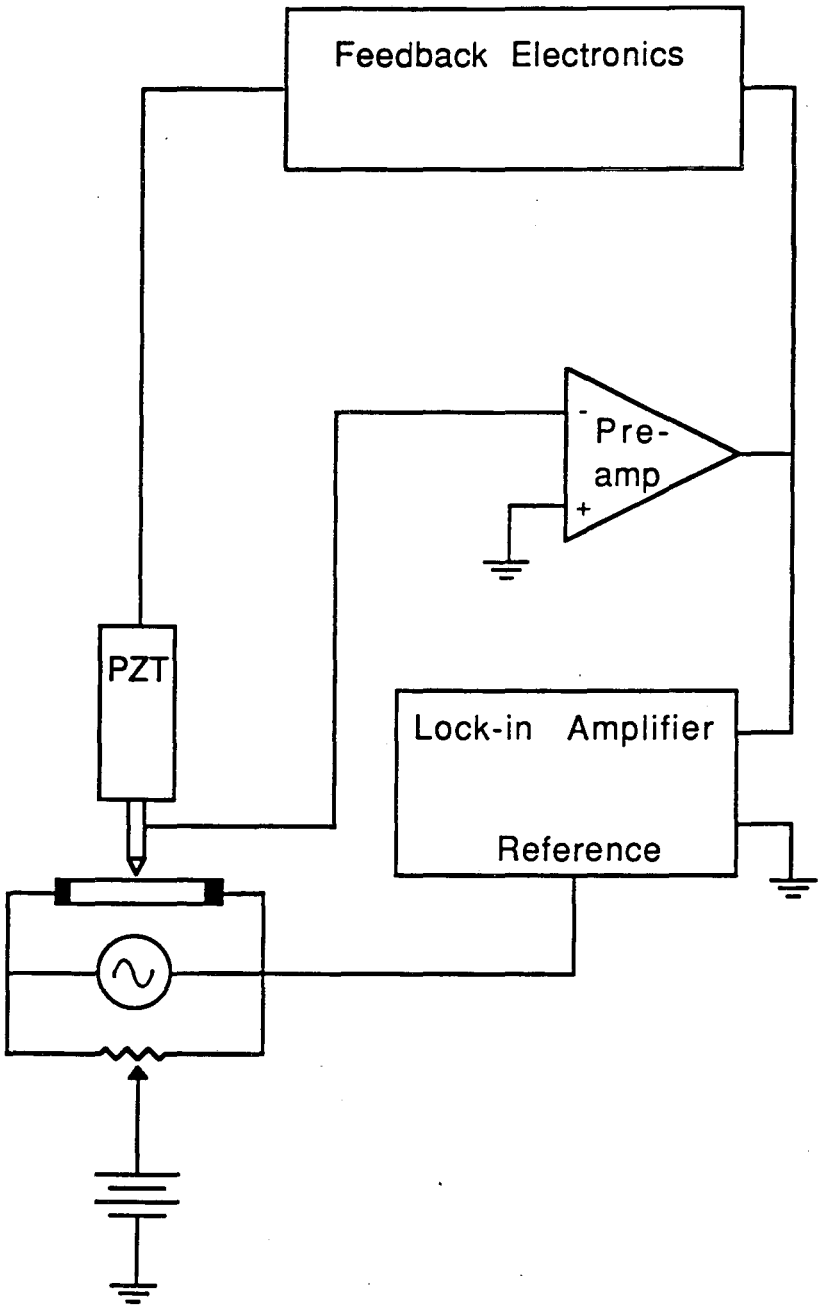


Figure 9-5 Block diagram of the electronics used to measure the surface potential.

inhomogeneities. This was the speculation that Gammie *et al.*[3] gave to explain their data. To test this possibility, we measured the surface potential directly with the STM using the bridge circuit shown in Fig.9-5. We applied a 1 V peak-to-peak voltage across the sample at 1 kHz, well above the roll-off frequency of the feedback circuit. Using a lock-in detector, we measured the 1 kHz signal from the preamplifier, and adjusted the potentiometer until the in phase 1 kHz component of the tunneling current was reduced to zero. By repeating the procedure at an adjacent point on the surface, about 1.6 μm away, we were able to measure the surface potential directly. The surface potential measured in this way was found to be within 20% of the average value.

To explain why the CDW remained visible at such high fields we have considered three alternative explanations. The most straightforward is that the charge density wave at the surface of the crystal is more strongly pinned than the CDW in the bulk. It is possible that the termination of the bulk periodicity is a sufficiently dramatic change in the potential seen by the CDW that it is able to pin the CDW. However, it should be noted that such an explanation hypothesizes the shearing of the CDW since it is not parallel to the surface. This would seem to be energetically unfavorable.

An alternative explanation is that the crystal of o-$TaS_3$ is divided into domains which depin at widely varying fields. With this explanation, the I-V curve would indicate the sliding of the most weakly pinned domains; other more strongly pinned domains could stay pinned until much higher fields were applied. However, we have

performed this experiment a total of 7 times on 3 samples, always with the same result, indicating that the majority of the sample surface does not depin until well above the threshold field.

A third hypothesis consistent with our data is a model used by J. H. Ross[7] to explain the motional narrowing observed in an NMR experiment in $NbSe_3$. In this model the charge density wave moves by discrete hops of exactly one CDW wavelength. Between hops the CDW is static. Ross estimated the time between hops to be greater than the time to make a single hop. A CDW moving in this manner would be imaged with an STM as a static CDW.

---

[1]A.Zettl, G.Gruner and A.H.Thompson, Phys. Rev. B **26**, 5760 (1982); and A.Zettl, C.M.Jackson and G.Gruner, Phys. Rev. B **26**, 5773 (1982).

[2]K.Tsutsumi, T.Sambongi, S.Kagoshima and T.Ishiguro, J. Phys. Soc. Japan **44**, 1735 (1978).

[3]G.Gammie, S.Skala, J.S.Hubacek, R.Brockenbrough, W.G.Lyons, J.R.Tucker and J.W.Lyding, Ultramicroscopy **152**, 497 (1988).

[4]C.G.Slough and R.V.Coleman, Phys. Rev. B **40**, 8042 (1989).

[5]T. Sambongi, K. Tsutsumi, Y.Shiozaki, Y.Yamamoto, K.Yamada and Y.Abe, Solid State Commun. **22**, 729 (1977).

[6]E. Bjerkelund, and A. Kjekshus, Zeitschrift Fur Anorganische und Allgemeine Chemie, **328**, 235 (1964).

[7]J.H.Ross, Ph. D. Thesis, University of Illinois, 1986.

# Chapter X
# Summary

In this thesis I began by describing our STM designed for variable temperature work, the electronics used to control it and the computer programs used for data acquisition and analysis. Since most of our work was done on 1T-$TaS_2$, I have described this material, its CDW, and the four separate temperature-dependent phases of the CDW.

We used this STM to study 1T-$TaS_2$ intensively. We imaged the material in all four of its phases and tracked the phase transition between the two highest temperature phases with both analysis of the STM images and resistance measurements. In the lowest temperature phase, the **C** phase, we were able to explain the wide variety of apparent CDW registrations relative to the lattice with a theory of multiple tips contributing to the STM image. We compared our STM data in the **NC** and **T** phase to models proposed for these phases with special consideration given to differentiating a truly discommensurate CDW from a moiré pattern formed by the CDW beating with the atomic lattice in the STM images. We found that discommensurations exist in both of the **NC** and the **T** phases. In the **NC** phase the domains are hexagonal in shape, although at low temperatures we found them to be somewhat smaller than was predicted. In the **T** phase, the trigonal symmetry is broken and the domains are long and narrow, although they are about 50% wider and at a different orientation than predicted in the stretched-honeycomb model. After a careful measurement of the fundamental CDW and

satellite peaks by x-ray diffraction we developed a striped model that agrees very well with the STM data. By a analysis of the Fourier transforms of our data, we were able to show that both the amplitude and the phase of the CDW vary nonuniformly across the sample surface in both phases, as was predicted in the models.

Finally, since the dynamics of the sliding CDW would be very interesting to study with STM we attempted to study both blue bronze and o-$TaS_3$, materials which exhibit Fröhlich conductivity. We took data of blue bronze at several temperatures, which always reflected the atomic surface symmetry, never the CDW symmetry. On o-$TaS_3$ our STM data only showed periodicity in one dimension, but, interestingly, showed the CDW periodicity well above the CDW transition temperature. We attempted to cause this 1-D CDW to depin at low temperatures by applying a field up to 7.5 times the threshold field, but we were never able to verify that we had caused the CDW to slide.

The STM is a great tool for studying the local surface properties of the CDW materials because it images the CDW directly. There exist several more CDW materials which might be studied with STM. These include 2H-$TaSe_2$, which exhibits a complex series of phases from 80K to 120K. Like 1T-$TaS_2$, it is hysteretic and the CDW forms domains in several phases, although in the case of 2H-$TaSe_2$ these domains are much larger ( 300 Å). It would still be very interesting to study Fröhlich conductivity with the STM, although some technical improvements would probably be necessary to make our STM capable of this. A quieter STM working in a vacuum on a vacuum cleaved crystal might have the resolution necessary to

image the CDW in blue bronze. A UHV microscope could also be used to try imaging the CDW in $(TaSe_4)_2I$ and $(NbSe_4)_{10/3}I$.

# APPENDIX

This appendix lists the menu trees for the four computer programs we use with our STM as described in Chapter 2.

## DEC LSI 11/73: DATA ACQUISITION PROGRAMS

SLOW SCAN DATA ACQUISITION PROGRAM: This program controls the analog scanning ramps and the STM itself for data acquisition in the slow, or constant current, mode.

Main Menu: ACQUIR program

1) Set up

    1-1) Acquisition speed

        1-1-1) Number of scans: controls the number of scans in the STM image

        1-1-2) X ramp up setting: tells the computer the frequency of the x ramp. This should be set to the reading on the x ramp up time potentiometer on the front panel of the analog ramp box

        1-1-3) X ramp down setting: NO LONGER IN USE

        1-1-4) Y ramp up setting: this informs the user of the correct setting for the y ramp up time potentiometer on the analog ramp box. It is calculated from the number of scans in the image and the x ramp up setting.

        1-1-5) Data acquisition rate: this tells the user the frequency with which data points are being read in by the A to D board.

1-1-6) Return: returns to the set-up menu

1-2) Calibration

1-2-1) Z amp gain: this should be set to the total gain of of the output of the feedback box before it is fed to the computer

1-2-2) HV amp gain: this is normally 25

1-2-3) XY HV amp gain: this is either 1 or 25 depending on the position of the selecting switch on the high voltage amplifier box

1-2-4) X ramp height: this is the amplitude of the X ramp in Volts as read off of the amplitude potentiometer on the analog ramp box

1-2-5) Y ramp height: this is the amplitude of the Y ramp in Volts as read off of the amplitude potentiometer on the analog ramp box

1-2-6) X Ångstroms/Volt: the calibration of the X drive

1-2-7) Y Ångstroms/Volt: the calibration of the Y drive

1-2-8) Z Ångstroms/Volt: the calibration of the Z drive

1-2-9) Return: returns to the set-up menu

1-3) Title: allows the user to enter a title for the image

1-4) Quick scan

1-4-1) On: sets quick scan feature on

1-4-2) Off: turns quick scan feature off

1-5) Viewing angle

1-5-1) Theta: the angle from the normal of the data

1-5-2) Phi: the angle around the normal of the data in a clockwise direction starting from the direction of +X

1-5-3) Return: returns to the set-up menu

1-6) Gain: adjusts the gains for the DISPLAY ONLY of the data

1-6-1) X gain

1-6-2) Y gain

1-6-3) Z gain

1-6-4) XZ gain

1-6-5) A gain

1-6-6) X scale

1-6-7) Y scale

1-6-8) Return

1-7) Aux data type: defines the variable stored in the auxiliary data array

1-7-1) None

1-7-2) dlnI/dS

1-7-3) dI/dV

1-8) Aux data calibration: calibrates the auxiliary data array

1-9) Store set-up: stores the current set up in the file DATA.VAR

1-0) Reset

1-0-1) Program reset: resets all the set-up parameters to those in the DATA.VAR file

1-0-2) Return: returns to the set up menu

1-A) Return: returns to the main menu

2) Take data: starts acquiring an image

3) Manipulate data

3-1) Redraw screen: redraws image using any new parameters that have been entered

3-2) Viewing angle: same as 1-5

3-3) Single scan: displays the amplitude along a single X scan

3-3-1) Choose new scan

3-3-2) Dump screen: this outputs single scan to printer

3-3-3) Return: returns to the manipulate data menu

3-4) Top view: displays the image in a grayscale planar view

3-5) Flatten picture

3-5-1) Auto rotate: rotates the image by finding the average value of Z along each edge and causing it to be equal to the average value of Z along the opposite edge

3-5-2) Least square flatten (whole picture): finds the best fit plane for the image and subtracts it from the image

3-5-3) Least square flatten (select region): same as 3-5-2 except that the plane is fit to some subset of the image chosen by the user

3-5-4) Return: return to manipulate data menu

3-6) Remove Z drift: calculates the average Z value of each X scan and subtracts it from each pixel in that scan

3-7) Show variables: displays all the important parameters of the image on either the screen or the printer

3-7-1) Printer

3-7-2) Screen

3-8) Set data type to display: chooses the data array to display

3-8-1) Topography

3-8-2) dInI/dS

3-9) Gains and scales: see 1-6

3-0) Hidden line

3-0-1) Hidden line is: toggles between enabled and disabled

3-0-2) Cross hatching is: toggles between enabled and disabled

3-0-3) Return

3-A) Remove scan lines: allows the removal of anomalous scan lines

3-A-1) Remove 1st scan

3-A-2) Remove last scan

3-A-3) Return

3-B) Plot height distribution: produces a histogram of all the Z values in the image

3-C) Return: returns to the main menu

4) Walk: not used with the microscope described in this thesis

5) Data Storage: reads and writes data files

5-1) Store data

5-2) Read data

5-3) Return

6) Send data

6-1) Send data to printer: prints out projected image

6-2) Send data to Tektronix: NO LONGER IN USE

6-3) Return: returns to main menu

7) Quit

FAST SCAN DATA ACQUISITION PROGRAM: This program controls the analog scanning ramps and the STM itself for data acquisition in the fast, or constant height, mode.

Main menu: FASTD

1) Take data: starts acquiring an image

2) Set-up

    2-1) Title: allows user to enter a title for the image

    2-2) Manual Triggering __: toggles between on and off. Manual triggering means that the space bar must be pushed to start each new image

    2-3) Fast Show Mode __: toggles between on and off. This option displays an abbreviated image in order to make the data acquisition proceed faster

    2-4) __ data bits: toggles between 4 and 8. The correct choice depends on which LSI 11/73 is being used

    2-5) __ scans per image: toggles between 128 and 256.

    2-6) Return: returns to main menu

3) Calibration

    3-1) X ramp height: the amplitude of the X ramp in Volts

    3-2) Y ramp height: the amplitude of the Y ramp in Volts

    3-3) X Ångstroms/Volt: the calibration of the X drive

    3-4) Y Ångstroms/Volt: the calibration of the Y drive

    3-5) Z Ångstroms/Volt: the calibration of the Z drive

    3-6) Return: returns to the main menu

4) Approach: not used with the microscope described in this thesis

5) Show single scan: this subroutine is supposed to display a single scan of the data, but it is not currently working.

6) Store data: stores STM in a FASTD format file

7) Read data: reads STM data from a FASTD format file

8) Send data to TEK: used to prepare files for transfer to the Tektronix. C returns to the main menu, F writes the data file as an ascii file, and A aborts the writing of the file after it has begun.

9) Quit

TEKTRONIX: DATA ANALYZING PROGRAMS

FAST FOURIER TRANSFORM PROGRAM: This program is designed to be the main data analysis program. It can calculate the Fourier transform of the image and filter the image as well as manipulate the data in a variety of ways.

Main Menu: FFT Program

1) Show data

    1-1) Single scan: displays the amplitude along a line through the data

    1-2) Squash output: skews image according to a linear transform

    1-3) View

        1-3-1) Top view: displays the data in top view

        1-3-2) Projected View: displays a projected view of the data

        1-3-3) Return: returns to show final menu

    1-4) Add scale bar: adds scale bar below image

    1-5) Get values: retrieves x, y, and z for a single data pixel

    1-6) Set color scale

1-6-1) Invert scale: inverts scale

1-6-2) Modify scale: lets user adjust color or grayscale parameters

1-6-3) Gray >< Color: toggles from color to grayscale

1-6-4) Return: returns to show final menu

1-7) Return: returns to main menu

2) Manipulate data

2-1) Manipulate data

2-1-1) Invert data: multiplies data array by -1

2-1-2) Flatten data: removes dishing of data in y direction by calculating average height of each x scan and subtracting this number from each pixel in that scan

2-1-3) Smooth data: filters data by assigning each pixel the weighted average value of the pixels surrounding it

2-1-4) Data Algebra

2-1-4-1) Raise data to power: replaces each pixel with its value raised to the specified power

2-1-4-2) Merge data: adds current image to that stored in special buffer (see 3-2-2)

2-1-4-3) Exponentiate data: replaces each pixel with its exponentiated value

2-1-4-4) Return: returns to manipulate data menu

2-1-5) Flip data: flips data about vertical center line

2-1-6) Rotate data: rotates data 180° about center point

2-1-7) Return: returns to manipulate data menu

2-2) Remove part of data

2-2-1) Copy subset of image: Enlarges subset of data

2-2-2) Remove single scan: Removes a single x scan from data array and replaces it with a scan interpolated from the scans directly above and below it

2-2-3) Turn background to zero: saves only a small subset of the image and sets the rest of the array to zero

2-2-4) Apodize data: apodizes the image according to the selected window

2-2-4-1) Sine apodization

2-2-4-2) Sinc apodization

2-2-4-3) Cosine apodization

2-2-4-4) Radial apodization

2-2-4-5) Return: returns to remove part of data menu

2-2-5) Make ave. zero: makes the average value of the data array equal zero

2-2-6) Set edge ave. to zero: causes the average value of the data along the edges of the array to be equal to zero

2-2-7) Return: returns to manipulate data menu

2-3) Set color scale: see 1-6

2-4) FFT filter data

2-4-1) Filter data: low pass filters FFT

2-4-2) Edit FFT

2-4-2-1) Copy/delete points

2-4-2-1-1) Copy data points: saves only pixels in the FT selected by cursor

2-4-2-1-2) Copy data peaks: fits a peak to the point in the FT selected by cursor and

saves the whole peak

2-4-2-1-3) Delete data points: replaces data pixels in the FT selected by cursor with zeroes

2-4-2-1-4) Return: returns to edit FFT menu

2-4-2-2) Copy subset: saves and enlarges a subset of the FT

2-4-2-3) Set grayscale: modifies grayscale parameters

2-4-2-4) Store FFT in buffer: stores FT in buffer

2-4-2-5) Show line through FFT

2-4-2-5-1) General line: displays amplitude along a line through the FT chosen with the cursor

2-4-2-5-2) Line to center: displays the amplitude along a line through the FT from a point chosen by the cursor to the center of the FT

2-4-2-5-3) Measure satellites: measures the intensity and position of up to 7 spots on the FT

2-4-2-5-4) Return: returns to edit FFT menu

2-4-2-6) Measure FFT: retrieves x, y, and the real and imaginary values from the FT array for pixels selected by the cursor

2-4-2-7) Reurn

2-4-2-7-1)Filter further: allows user to do a

low pass filter on the FT

2-4-2-7-2) Reverse transform: performs inverse transform

2-4-2-7-3) Return to main menu: returns to main menu CAUTION: IF THE REVERSE TRANSFORM IS NOT PERFORMED THE CURRENT IMAGE CANNOT BE VIEWED OR FURTHER PROCESSED, BUT A NEW IMAGE OR SATELLITE FILE MUST BE READ IN.

2-4-3) Get FFT from buffer: recalls FT from buffer (see 2-4-2-4)

2-4-4) Read satellite file: recalls previously stored file of satellite point values

2-4-5) Return: Returns to manipulate data menu

2-5) Data buffer

2-5-1) Store data in buffer

2-5-2) Read data from buffer

2-5-3) Return: returns to manipulate data menu

2-6) Analyze data

2-6-1) Est. height diff.: determines height difference between two planes which are determined by fitting the planes to the data in selected rectangles

2-6-2) Autocorrelate: performs an autocorrelation on a selected subset of the data

2-6-3) Stat. diff.: calculates the statistical difference of the data array

2-6-4) Only real data: only for files that were originally

acquired as 128 scan images, this option removes the scans that were interpolated from the original data and produces an array of which the lower 1/2 is the original data and the upper 1/2 is zeroes

2-6-5) Cut off data: Replaces the data array with zeroes everywhere except for local maximum which are replaced by 1's

2-6-6) Return: returns to manipulate data menu

2-7) Return: returns to main menu

3) Data I/O

3-1) Read data: reads data file

3-2) Store data: stores data in file

3-3) Receive DEC transfer: NO LONGER USABLE

3-4) Create model data

3-4-1) Make IC TaS2 data: creates a data file which mimics 1T-TaS2 data

3-4-2) Make IC+domains TaS2 data: same as 3-4-1

3-4-3) Make DC TaS2 data: same as 3-4-1

3-4-4) Make blue bronze data: creates a data file which mimics blue bronze data

3-4-5) Return: returns to Data I/O menu

3-5) Write ASCII file: translates current image into ascii file for transfer over BITNET

3-6) Change data size: adjusts scaling parameter which translates pixels into Ångstroms

3-7) Return: returns to main menu

4) 3D display

4-1) Draw pedestal: draws a 3-D pedestal below the image

4-2) Set light source: allows user to adjust the position and intensity of the apparent light sources of the image

4-3) Set gray scale: see 1-6

4-4) Halftoning: toggles halftoning on and off

4-5) Return: returns to main menu

5) Quit

CALIBRATION PROGRAM: This program is designed to transform data to a hexagonal symmetry (to remove skewing due to drift or incorrectly scored PZT scanners) and to create a model of the data that clarifies the relative positions and orientations of the various parts of the data.

Main Menu: CAILB program

1) Start new image

1-1) Use photo on tablet: NO LONGER IN USE

1-2) Use image on screen

1-2-1) Use existing size: uses image as is

1-2-2) Transform to hcp: calculates a linear transform to try to make the image as hexagonal as possible

1-2-3) Straighten image: adjusts position of each scan in x in order to minimize the effect of a curving image

1-3) Return: returns to main menu

2) Input lines

2-1) Input lines: draws lines on image

2-2) Input shapes: draws shapes on image

2-3) Delete lines/shapes

2-3-1) Delete all lines: deletes all lines

2-3-2) Delete last group: deletes only the last entered set of lines

2-3-3) Delete all shapes: deletes all shapes

2-3-4) Delete last shape: deletes only the last entered shape

2-3-5) Return: returns to main menu

2-4 Return: returns to main menu

3) Print out stats: prints out information on linear transform and on lines and shapes entered

4) Draw grid: draws a honeycomb shaped grid on top of model data

5) Camera ready: draws the model only in large format

5-1) Set all colors white

5-2) Annotate image

5-2-1) Draw wide lines

5-2-2) Edit lines

5-2-2-1) Redraw a line

5-2-2-2) Remove a line

5-2-2-3) Set line width

5-2-2-4) Return

5-2-3) Draw panels

5-2-4) Draw dotted lines

5-2-5) Add text

5-2-6) Delete annotation

5-2-7) Return

5-3) Set graphite params

5-3-1) Line width

5-3-2) Fill pattern

5-3-3) Dot visibility

5-3-4) Return

5-4) Set circle size

5-5) Select fill pattern

5-6 Return

6) Data I/O

6-1) Read data file: reads in a file of a model

6-2) Write data file: writes a file of the current model

6-3) Read image file: reads in a file of an actual image

6-4) Directory: displays current working directory

6-5) Transform image

6-5-1) Draw skewed image: draws image using linear transform calculated in 1-2-2

6-5-2) Store skewed image: stores a file of the current image skewed according to transform from 1-2-2

6-5-3) Draw and Store: does both 6-5-1 and 6-5-2

6-5-4) Return: returns to data I/O menu

6-6) Return: returns to main menu

7) Quit

LAWRENCE BERKELEY LABORATORY
UNIVERSITY OF CALIFORNIA
TECHNICAL INFORMATION DEPARTMENT
BERKELEY, CALIFORNIA 94720